Universität Hamburg
Department Physik

Extreme Ultraviolet Fluorescence Spectroscopy of Pure and Core-Shell Rare Gas Clusters at FLASH

Dissertation

zur Erlangung des Doktorgrades
des Department Physik
der Universität Hamburg

vorgelegt von

Lasse Schroedter

aus Hamburg

Hamburg
2013

Gutachter der Dissertation: PD Dr. Tim Laarmann
Prof. Dr. Wilfried Wurth

Gutachter der Disputation: PD Dr. Tim Laarmann
Prof. Dr. Thorsten Uphues

Datum der Disputation: 27.06.2013

Vorsitzender des Prüfungsausschusses: PD Dr. Michael Martins
Vorsitzender des Promotionsausschusses: Prof. Dr. Peter Hauschildt
Leiterin des Fachbereichs Physik: Prof. Dr. Daniela Pfannkuche
Dekan der Fakultät MIN: Prof. Dr. Heinrich Graener

Abstract

The interaction of rare gas clusters with short-wavelength radiation of free-electron lasers (FELs) has been studied extensively over the last decade by means of electron and ion time-of-flight spectroscopy. This thesis describes the design and construction of a fluorescence spectrometer for the extreme ultraviolet (XUV) spectral range and discusses the cluster experiments performed at FLASH, the Free-electron LASer in Hamburg. Fluorescence of xenon and of argon clusters was studied, both in dependence on the FEL pulse intensity and on the cluster size. The FEL wavelength was set to the giant $4d$-resonance of xenon at 13.5 nm and the FEL pulse intensity reached peak values of $2.7 \cdot 10^{15}$ W/cm^2. For xenon clusters, charge states of at least 11+ were identified. For argon, charge states up to 7+ were detected. The cluster-size dependent study revealed a decrease of the fluorescence yield per atom with increasing cluster size. This decrease is explained with the help of a geometric model. It assumes that virtually the entire fluorescence yield stems from shells of ions on the cluster surface, whereas ions in the cluster core predominantly recombine non-radiatively with electrons. However, the detailed analysis of fluorescence spectra from clusters consisting of a core of Xe atoms and a surrounding shell of argon atoms shows that, in fact, a small fraction of the fluorescence signal comes from Xe ions in the cluster core. Interestingly, these ions are as highly charged as the ions in the shells of a pure Xe cluster. This result goes beyond the current understanding of charge and energy transfer processes in these systems and points toward the observation of ultrafast charging dynamics in a time window where mass spectrometry is inherently blind.

Zusammenfassung

Die Wechselwirkung von Edelgasclustern mit der kurzwelligen Strahlung von Freien-Elektronen-Lasern (FELs) wurde in den vergangenen 10 Jahren intensiv untersucht. Diese Doktorarbeit beschreibt den Entwurf und die Konstruktion eines Fluoreszenzspektrometers für den extrem-ultravioletten Wellenlängenbereich und diskutiert die Clusterexperimente, die damit an FLASH (Free-electron LASer in Hamburg) durchgeführt wurden. Fluoreszenz von Xenon- und von Argonclustern wurde untersucht, sowohl in Abhängigkeit von der FEL-Pulsintensität als auch der Clustergröße. Die FEL-Wellenlänge war auf die $4d$-Riesenresonanz von Xenon bei 13.5 nm eingestellt, und die FEL-Pulsintensität erreichte Maximalwerte von $2.7 \cdot 10^{15}$ W/cm^2. Ladungszustände von mindestens 11+ wurden in Xenonclustern identifiziert. Bei Argonclustern wurden Ladungszustände bis zu 7+ detektiert. Die clustergrößenabhängige Untersuchung zeigt, dass die Fluoreszenzausbeute pro Atom mit steigender Clustergröße abnimmt. Diese Beobachtung kann mit Hilfe eines geometrischen Modells erklärt werden. Es basiert auf der Annahme, dass fast die gesamte Fluoreszenz von Ionen stammt, die sich in einer Schale an der Clusteroberfläche befinden, wohingegen die Ionen im Kern zum Großteil strahlungslos mit Elektronen rekombinieren. Darüber hinaus zeigt jedoch die detaillierte Analyse der Fluoreszenzspektren von Clustern, die aus einem Kern aus Xenonatomen bestehen, der umgeben ist von einer Schale aus Argonatomen, dass ein kleiner Teil der Fluoreszenz von Xe-Ionen im Clusterkern stammt. Interessanterweise sind diese Ionen genauso hoch geladen wie Ionen in der Schale eines reinen Xe-Clusters. Dieses Resultat geht über das derzeitige Verständnis von Ladungs- und Energietransferprozessen in diesen Systemen hinaus und weist auf die Beobachtung ultraschneller Aufladungsdynamik in einem Zeitfenster hin, in dem Massenspektrometrie methodisch bedingt blind ist.

Contents

1. Introduction

Structure and dynamics of matter interacting with strong laser pulses raised a lot of interest in the last decade, because new experimental regimes became accessible that push the experiments to new boundaries: (i) Short wavelengths: the shorter the wavelength, the smaller the possible focus and consequently the resolvable sample size. Furthermore, the high photon energy allows the direct photoionization of inner-shell electrons, giving element- and site-specificity in the investigation of molecules. (ii) High photon flux: large numbers of photons are needed to generate high intensities, which can be used to drive non-linear processes or collect a scattering signal from very small, dilute or non-periodic systems. (iii) Light pulses with short durations: with short light pulses it is possible to study phenomena in a time-resolved manner, for instance transitions between structures of molecules. Such transitions are the basis of molecular function.

Each of these properties allows novel research but even more possibilities for experiments open up if they are all available simultaneously. The only sources which combine all these properties are short-wavelength free-electron lasers (FELs), which have been available since 2005 when FLASH, the Free-electron LASer in Hamburg, was made accessible for user operation. Since then, additional FELs have been built, which either offer, as FLASH does, pulses mainly in the extreme-ultraviolet (XUV[1]) wavelength range (FERMI@Elettra [2]) or pulses in the Ångström regime of X-rays (LCLS [3] and SACLA [4]).

The topic of this thesis is the interaction of FEL pulses with clusters, conglomerates of atoms ranging in size from just a few to ten thousands of atoms. Clusters are a link between molecules and the condensed phase of elements. As clusters grow in size, one can study the transformation of material properties at an atomic or molecular level to the characteristics at bulk level (Jortner [5]). Particularly interesting in this context is the role of surface atoms compared to the bulk, because the ratio of surface atoms to bulk atoms continually changes with growing cluster size. I will try to illustrate why clusters make for intriguing research objects by giving a few examples of milestones in cluster research and future applications.

One fascinating class of experiments which has been proposed to be carried out at FELs is the imaging of a *single* molecule in a single light pulse (Neutze et al. [6]). Such an experiment can reveal the structure of molecules which cannot be prepared in crystalline form and, due to the shortness of FEL pulses, also possible transitions between structures, if a time-resolved pump-probe scheme is used. Experiments of this kind are often advertised as 'molecular movies'[2]. However, a severe concern in such experiments is the damage done to the molecule by the light pulse. As the light is scattered by the bound electrons of the molecule, the molecule is destroyed. It is a complex question whether sufficient scattering signal can be detected before the molecule disintegrates. One possible way to alleviate this problem is adding a tamper layer around the molecule (Hau-Riege et al. [7]). At this point, cluster science comes into play. Rare-gas clusters are relatively simple systems, which can be easily generated by expanding gas through a nozzle. The interatomic distance in rare-gas clusters

---

[1] For the wavelength regimes relevant to this thesis, I will from now on follow the definitions given in the book by Attwood [1]: XUV: 40–5 nm, soft X-rays: 5–0.3 nm, X-rays: shorter wavelengths.

[2] In a pump-probe setup, two light pulses with a variable time separation between them are used. The first pulse, the pump, induces a structural change in a molecule. The second pulse, the (FEL) probe, is used to image the molecular structure. By repeating the measurement with different time delays between the pulses and concatenating the images, a 'molecular movie' is formed.

is a few Å, just like in molecules (Saalmann [8]). They can be used as model systems to measure how much energy is absorbed. Because they are surrounded by vacuum, no energy can dissipate. Their relatively simple structure also makes them accessible via theoretical calculations. Furthermore, it is also possible to test the effect of tamper layers, as so-called core-shell clusters can be generated, with a core consisting of one element and a surrounding shell consisting of another. A schematic drawing of such a cluster is shown in figure 1.1. This is only one example of the possible impact of investigations of laser-cluster-interaction. Extensive work has been done on the interaction of clusters and light at near-infrared and ultraviolet wavelengths. For instance, in 1993 McPherson et al. measured XUV light around 10 nm that was generated after illuminating rare-gas clusters with 248 nm-photons from a high power laser [10]. One year later, they published results showing the generation of X-ray photons between 0.2 and 0.3 nm with the same excitation wavelength [11]. In 1997, Ditmire et al. [12] showed that upon irradiation with 780 nm-photons focused to a peak intensity of $2 \cdot 10^{16}$ W/cm^2, a plasma is formed in xenon clusters which can generate ions with kinetic energies up to 1 MeV. In 1999, Ditmire et al. [13] observed the emission of neutrons produced by nuclear fusion in deuterium clusters irradiated by an intense laser pulse (λ =820 nm, peak intensity $2 \cdot 10^{16}$ W/cm^2).

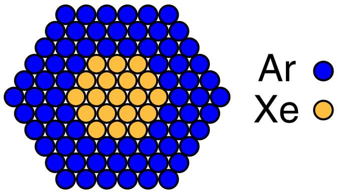

Figure 1.1.: Schematic drawing of a core-shell cluster (from Hoener et al. [9])

The history of experiments of rare-gas clusters at FELs is naturally shorter, but it has already provided new insight into the interaction of light and matter. The very first cluster experiment at a short-wavelength FEL, carried out by Wabnitz et al. [14] at the predecessor of FLASH, the TTF1, analyzed xenon clusters irradiated by photons with a wavelength of 100 nm. Unexpectedly high charge states up to 8+ were observed. This experiment generated a lot of interest in the capabilities of FELs (see for example Kapteyn and Ditmire [15]). New theoretical models were needed to account for the strong absorption of the clusters. Theoretical models were developed by, for instance, Siedschlag and Rost [16], Santra and Greene [17], Jungreuthmayer et al. [18] and Bauer [19]. By now, theoretical modeling and experimental data have converged and there is general agreement on the description of the VUV-FEL interaction with rare gas clusters.

In 2008, Hoener et al. [9] could show in an experiment using core-shell clusters made of a xenon core with an argon shell that electrons are efficiently transferred to the cluster center, where recombination takes place, as they found no evidence of high Xe charge states from the core-shell cluster. This result was confirmed by Thomas et al. [20], who modeled the measured kinetic energy distribution of Xe ions originating from a cluster with an electrostatic model. They showed that at the end of the FEL-cluster interaction the positive charge is concentrated on a shell on the outside of the cluster, which explodes off, whereas the cluster core expands more slowly. In the last years, a new class of experiments for the study of clusters has emerged: the analysis of FEL photons scattered from clusters (Bostedt et al. [21]). These experiments can analyze the geometric structure of clusters and, to some extent, are also able to detect transient charge states. They represent an important extension of standard experimental techniques insofar as they do not rely on the use of ion time-of-flight spectrometers (TOFs). TOFs have some inherent limitations, which will be described in the following and which are also the reason for the novel experimental approach chosen in this thesis.

Almost all of the cluster experiments at FLASH mentioned above employ TOFs. With these devices, one can determine the charge state of ions by measuring their flight time from the interaction region to the detector. A feature which makes TOFs a natural choice for the analysis of the experiments described above is their high detection efficiency. By choosing adequate electric fields, virtually all ions which result from the total disintegration of a cluster can be collected and guided to the detector. However, TOFs also have a significant limitation: microseconds pass from the creation of the ions to their reaching the detector. Compared to the interaction time of the FEL pulse with the cluster ($\approx$100 fs) this is a very long time[3,4]. The experiments of Hoener et al. and Thomas et al. showed that high charge states recombine in the cluster but they could only detect remnants, indirect evidence of this process.

For these reasons, the experiments presented in this thesis aim to expand the experimental possibilities by employing another detection technique, extreme-ultraviolet fluorescence spectroscopy. As ions are created and recombine, there is also a chance of their immediate decay emitting a fluorescence photon, while the cluster is much closer to its initial geometry. By analyzing fluorescence spectra of the cluster ions, we expect to gain direct insight into the charge states that are initially created during the interaction of FEL radiation and rare gas clusters.

---

[3] Secondly, the strong TOF fields may alter the experimental observation (Fennel et al. [22]).

[4] Another limitation of TOFs is that space charge effects in dense cluster beams may alter the measured kinetic energy distributions, leading to an overestimate of the absorbed photon energy.

2. Foundations

Having introduced the aim of this work and the performed experiments in the previous chapter, it is now time to take a more detailed look at the phenomena involved.

As the study of clusters is at the heart of this work, I will start by explaining what a cluster actually *is*. From then on, the outline of this chapter will follow the path of the light, first giving an introduction to FLASH, where the light is generated. The next step is the excitation of the cluster by the light. Therefore, the corresponding section deals with the interaction of clusters with very intense laser pulses, describing ionization and subsequent processes within the cluster.

From there on, we will keep following the light, although no longer the photons responsible for the excitation but the resulting fluorescence photons. This requires a look on fluorescence, also with respect to competing relaxation mechanisms.

The last resting place of the fluorescence photons is the detector of the spectrometer. But to get them there, one has to use optical elements, which work differently in the extreme ultraviolet spectral range compared to the visible spectral range. The last section of this chapter therefore deals with optics at XUV wavelengths.

Of course, this chapter cannot explore any of these topics in exhaustive detail, but the aim is to provide a framework which allows to analyze the measured data and also to appreciate the challenges faced while collecting it.

2.1. Clusters

Clusters are conglomerates of atoms, larger than molecules and smaller than solids, so in principle, a cluster can range in size from just a few to ten thousands of atoms. There are several reasons clusters make for intriguing objects of research. Firstly, their size can easily be varied in an experiment, which allows studying effects such as multiple ionization and plasma formation in laser-matter-interaction as they evolve from their manifestation in atoms to that in solids.

Another characteristic of clusters is that there is no hidden energy dissipation. When depositing energy in solids, data analysis is always complicated by the fact that energy which is deposited on the surface is being dissipated into the bulk of the material. With clusters, this is not possible, because in gas-phase experiments they are free, i.e. surrounded by vacuum. Any energy deposited in a cluster is guaranteed to take its effect in that cluster, be it in the form of light emission, emitted electrons, structural changes or even a totally destroyed cluster. The effect of the deposited energy is open for analysis.

As mentioned in the introduction, this thesis describes experimental investigations on rare gas clusters. There are several reasons for this: firstly, they are, compared to metal clusters for instance, rather simple systems, bound only by van-der-Waals forces. This makes them ideal candidates for theoretical investigation. Secondly, this PhD thesis further explores effects which were found in rare gas clusters. By looking at fluorescence light of the ions, this work provides information on a moment much closer to the cluster ionization than time-of-flight spectra of charged particles. As was stated in the introduction, the immediate response of the cluster to the FEL pulse and the possible production of high, transient charge states is of great interest for future experiments. I will give a short overview of those experiments, and of the most relevant experimental and theoretical works on rare-gas clusters exposed to strong XUV pulses in general, in chapter 2.4.

While a novice might envision the production of clusters of a defined size to be complicated, it is actually, at least for rare gas clusters, rather simple. All that is necessary is a means of letting a rare gas of defined pressure expand through a nozzle. For some gases it is necessary to lower the temperature before cluster formation begins, but for both gases used in our experiments, xenon and argon, room temperature is sufficient.

Empirical formulas for the average size of clusters have been established by Hagena [23]. They are based on the factor Γ^*. Wörmer et al. [24] introduced a way of calculating Γ^* using the pressure, which is a bit easier to handle than the original version by Hagena:

$$\Gamma^* = \frac{p_0[\mathrm{mbar}] \cdot d_{\mathrm{eq}}^{0.85}[\mathrm{\mu m}]}{T_0^{2.2875}[\mathrm{K}]} \cdot K_{\mathrm{ch}}, \tag{2.1}$$

where d_{eq} is the equivalent nozzle diameter for conical nozzles[1] introduced by Hagena [26]:

$$d_{\mathrm{eq}} = \frac{0.74 \cdot d}{\tan\delta}, \tag{2.2}$$

with δ being half the opening angle of the conical nozzle and d the smallest actual diameter of the nozzle.

p_0 is the stagnation pressure and T_0 is the nozzle temperature. K_{ch} is a dimensionless, element-specific factor. For xenon $K_{\mathrm{ch}} = 5554$, for argon $K_{\mathrm{ch}} = 1646$.

For $\Gamma^* > 1800$ the *average* number $\overline{N}$ of atoms in a cluster is given by

$$\overline{N} = 33 \cdot \left(\frac{\Gamma^*}{1000}\right)^{2.35} \tag{2.3}$$

Buck and Krohne [27] found that for values of Γ^* between 350 and 1800, a slightly modified version of the formula fits their experimental results better.

For $350 < \Gamma^* < 1800$

$$\overline{N} = 38.4 \cdot \left(\frac{\Gamma^*}{1000}\right)^{1.64} \tag{2.4}$$

It has to be stressed that these formulas give an *average* size of the cluster. As an estimate, the width of the distribution can be taken to be equal to the average cluster size (von Pietrowski [28]), so for an average cluster size of 6000 atoms, there would be clusters present ranging from 3000 atoms to 9000 atoms. Figure 2.1 shows a measurement of an argon cluster size distribution by Karnbach et al. [29] which illustrates this rule of thumb. Furthermore, the average cluster size varies across the cluster beam, the largest sizes being in the center of the beam cross section, the smallest in the outer regions (Dorchies et al. [30]). The geometric structure of rare-gas clusters depends on the number of atoms in the cluster. According to

---

[1] According to Joppien [25], for this formula to be valid, the length of the conical portion of the nozzle has to be at least 5 equivalent nozzle diameters, after which the cluster formation is expected to have finished.

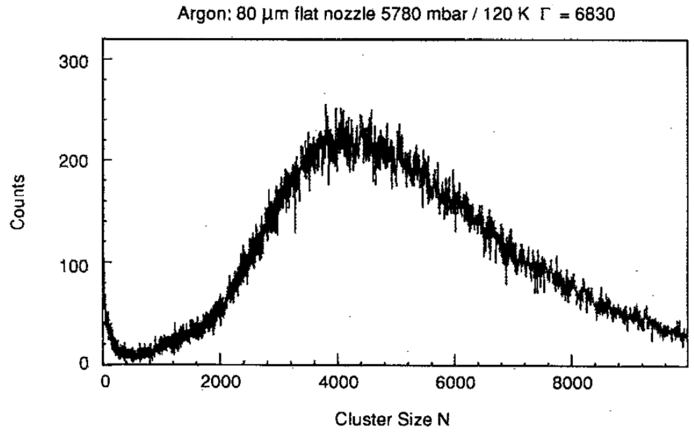

Figure 2.1.: Argon cluster size distribution for $\Gamma^* = 6830$ (Karnbach et al. [29]).

Farges et al. [31], the number of atoms at which transitions in cluster structure occur are identical for argon and xenon. They found that below an average number $\overline{N}$ of atoms in the cluster, the cluster is amorphous. Between $\overline{N} = 50$ and $\overline{N} = 800$, it has a icosahedral structure and at values larger than $\overline{N} = 800$, it exhibits a crystalline face centered cubic (fcc) structure. The surface of an icosahedron consists of 20 equal, equilateral triangles. It has 30 edges of equal length and 12 corners, at each of which 5 planes meet. Mackay showed [32] that atoms can be arranged in such an icosahedral structure. The smallest example is a cluster consisting of 13 atoms. One atom is situated in the cluster center, the other 12 are on the surface, each of them representing one of the corners. To form the next possible icosahedron, this shell of 12 atoms has to be covered by another shell of atoms. The number of atoms at which a shell is complete and an icosahedral structure is formed can be calculated by the following formula (see Mackay [32]):

$$N = \frac{10}{3}n^3 + 5n^2 + \frac{11}{3}n + 1 \tag{2.5}$$

N is the number of atoms in the cluster and n is the number of complete, also called closed, shells. For $n = 1$, there are the aforementioned 13 atoms in the cluster. For $n = 2$, one gets $N = 55$. The following closed shells occur at $N = 147,\ 309,\ 561, \ldots$. The numbers at which closed shells occur are also often called *magic numbers*, because it has been found, similar to nuclei in atoms, that clusters with such a number of atoms are especially stable (see for example Echt et al. [33]).

The unit cell of an fcc-system is formed by 8 atoms at the corner of a cube and 6 atoms in the middle of each face of that cube. Both argon and xenon form fcc-lattices in solid bulk form, therefore it makes intuitive sense that at a certain cluster size a transition to the structure found in the bulk has to take place.

Apart from clusters consisting of only a single rare gas element, one can also produce so-called *core-shell* clusters. These are clusters that consist of a shell of rare gas atoms surrounding a cluster core made of a different rare gas species. The simplest experimental method to produce core-shell clusters is to use the same setup as for pure clusters but replace the pure gas by a mixture of the two gases of which one wants to form the clusters. In this thesis, Xe-core-argon-shell clusters were studied. For the experiment presented in chapter 4.5, a mixture of 2 % xenon in argon was used. Differences in the binding energies and the melting points of xenon and argon lead to a nucleation of xenon inside the argon clusters (see Hoener et al. [9]). However, the fraction of xenon atoms inside the argon cluster is not simply equal to the fraction of xenon atoms in the gas mixture: Danylchenko et al. [34] studied Xe-Ar clusters by electron diffraction and optical methods. They found an enrichment of xenon in the argon cluster by a factor of about 10, compared to the abundance in the gas mixture. They attribute this factor to the higher binding energy of xenon. They could also show that there is a sharp transition from xenon to argon and that xenon is located in the cluster core.

2.2. FLASH

FLASH is a free-electron laser. Its functional principle will be described below but to introduce the most important parameters it is sufficient to say that light is emitted from bunches of electrons which are accelerated and forced onto a sinusoidal path. FLASH produces 10 so-called bunch trains per second. The number of bunches in a bunch train can be any value between 1 and 800 individual bunches. The minimum temporal distance between bunches in a bunch train is 1 μs. Each of these bunches emits an ultrashort light pulse. Frühling et al. measured pulse lengths below 50 fs [35]. Wavelengths can range from about 47 to about 4 nm [36]. The pulse energies depend on several parameters, including the pulse duration and wavelength, therefore it is not possible to give a single, valid value for all parameter ranges. As an example, in the experiments presented here, with pulse durations >100 fs, a wavelength of 13.5 nm and single-bunch-mode operation[2], average pulse energies up to 150 μJ were generated.
For the scope of this work, FLASH is mainly regarded as a means of obtaining light of the wavelength and intensity required for the experiment. Nevertheless, a look at the functional principle of FLASH is useful, as it reveals a certain randomness of the process. This randomness inevitably leads to fluctuations in the generated light, which of course is of concern to the experimenter.

2.2.1. How FLASH works

A more detailed description of FLASH can for instance be found in Ackermann et al. [37], but for our purposes the detail found in figure 2.2 is sufficient. The elements of FLASH which are necessary to understand its functional principle are the radio-frequency electron gun, the linear accelerator modules, and the undulator. In the electron gun, electron bunches are generated in a precisely clocked way. The electrons are brought to energies of up to 1.25 GeV [36] by the linear accelerator modules.

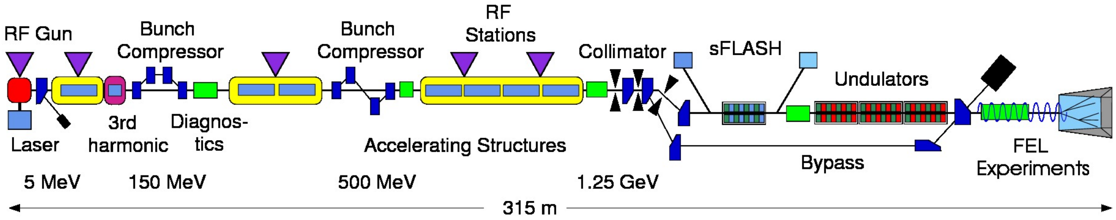

Figure 2.2.: Schematic overview of the principal elements of FLASH (from [38])

As a next step, the electrons enter the undulator. Undulators are structures of alternating permanent magnets. As the electrons pass through the undulator, they are forced onto a sinusoidal path. This constitutes an acceleration of the electrons. Charged particles which are accelerated emit light. Within an undulator, electrons are stimulated to emit radiation

---

[2] in which each bunch train consists of only a single bunch

of wavelength λ_e which depends on the undulator parameters in the following way (see, for instance, Attwood [1]).

$$\lambda_e = \frac{\lambda_u}{2\gamma^2}\left(1 + \frac{K^2}{2} + \gamma^2\theta\right), \tag{2.6}$$

where λ_u is the undulator period, i.e. the distance of one north pole to the next in the undulator structures. γ is the Lorentz factor known from the theory of relativity:

$$\gamma \equiv \frac{1}{\sqrt{1 - \frac{v^2}{c^2}}}, \tag{2.7}$$

where v is the velocity of the electrons and c is the velocity of light in vacuum. θ is an angle measured from the axis defined by the travel direction of the electrons. Finally, K is the so-called *magnetic deflection parameter*, given by

$$K \equiv \frac{eB_0\lambda_u}{2\pi m_e c}, \tag{2.8}$$

where e is the electron charge, m_e is the electron mass and B_0 is the magnetic field strength of the undulator magnets.

Now the process which is unique to FELs starts, the so-called SASE, or self-amplified spontaneous emission. The photons which are spontaneously emitted into the direction of travel of the electrons begin interacting with the electron bunch. As they interact with the light field, some electrons gain energy from the light field and are accelerated, and some lose energy to it and are slowed. This effect results in the formation of so-called microbunches within the original electron bunch; the electrons, which were formerly more or less evenly distributed along the bunch are now compressed into thin slices along the longitudinal axis of the electron beam, i.e. in the direction of travel. They are spaced with a period equal to the wavelength of the undulator radiation. Therefore, all electrons, in contrast to a synchrotron, radiate in phase.

The resulting radiation shows laser-like qualities: it is coherent, delivered in very short bursts, while being almost monochromatic (the spectral width is about 0.5 - 1% of the central wavelength (FWHM) [39]). Furthermore, the wavelength of FLASH can be tuned by changing the electron energy. A variation of the energy by varying the undulator gap is not possible at FLASH because the gap width is fixed.

All of these properties are highly desirable for experiments. However, it is important to keep in mind that the process which produces the radiation is of statistical nature. It starts from shot noise. This randomness produces variations from shot to shot in the spectral and temporal structure. (It can also shift the arrival time of the light pulse but this is of no concern for our experiment since we have to average over many hundreds of shots). Consequently, these variables cannot be assumed to be constant and have to be monitored during the experiment and taken into account during the evaluation of the data.

2.3. Xenon: Giant resonance and ionization scheme at 13.5 nm

Up to this point, it has not been explained why we chose an excitation wavelength of 13.5 nm for our experiments. The reason for this choice was that xenon exhibits a strong peak in its

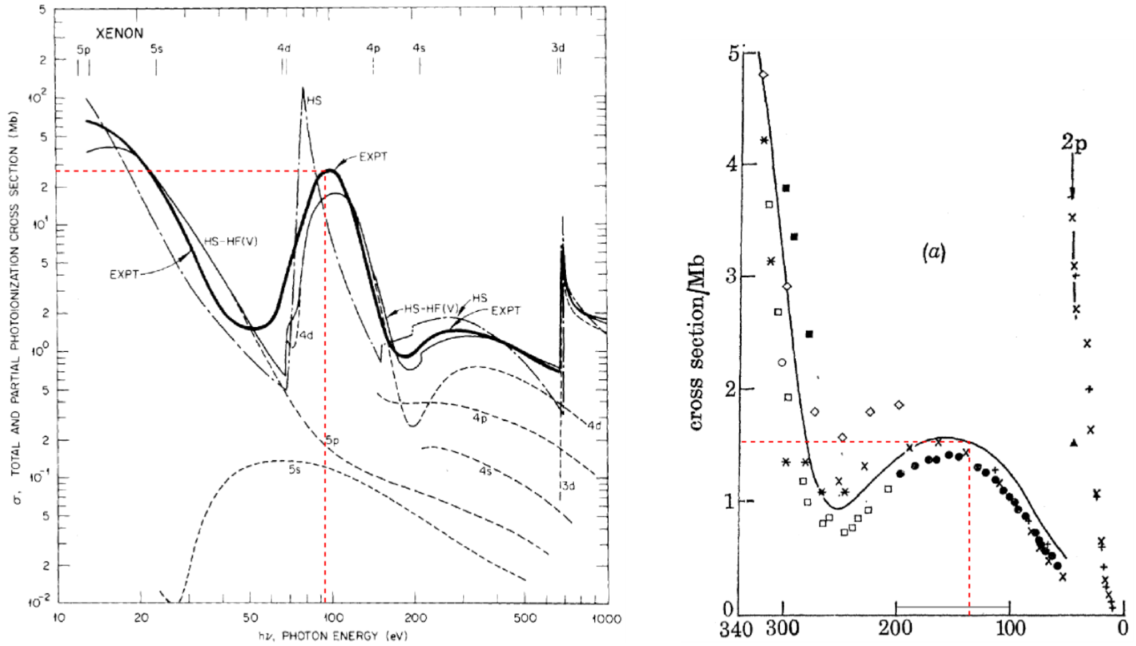

(a) Total photoionization cross section of xenon (from Krause [40]). The so-called *giant resonance* of xenon, centered at about 100 eV can clearly be seen.

(b) Total photoionization cross section of argon (from West and Marr [41])

Figure 2.3.: Total photoionization cross sections of Xe and Ar. I have added the dashed red lines to indicate the values at 13.5 nm, where our experiments were carried out. Compared to xenon, the cross section of argon is lower by about a factor of 17.

photoionization cross section, centered at about 100 eV or 12.4 nm. This rise in the cross section is often called the *giant resonance* of xenon. The origin of the giant resonance in xenon is very complex since many different effects contribute, single-electron effects as well as many-electron effects. Figure 2.3(a), taken from Krause [40], shows the giant resonance. The total cross section given was measured experimentally, whereas the cross sections of specific shells were calculated. As can be seen, the giant resonance is mainly due to a peak in the cross section of the 4d-shell but there is also a contribution from the valence shells 5s and 5p. The 4d-resonance is classified as a so-called *shape resonance* (see, for instance, [42]). This term refers to the temporary trapping of an ionized electron in a potential relatively close to the ion core, thereby increasing the photoionization cross section. The shape resonance accounts for the broad maximum between approximately 70 and 200 eV. Another defining feature are *Cooper minima*. A Cooper minimum, on a theoretical basis, is caused by a node on the wave function of a certain electron (Cooper [43]). The minimum at about 200 eV is due to a Cooper minimum of the 4d-electron (see Krause [40]). While these effects are single-electron effects, there are also important many-electron effects. For instance, Becker et al. [44] observed *shake-up* and *shake-off* processes associated with the 4d-shell. These processes describe the absorption of a single photon leading to the excitation of two electrons. In the case of the shake-off process, both electrons are ionized. In the case of the shake-up process, one electron is ionized and the other one is transferred to a more weakly bound state. To make matters even more complicated, the photoionization cross section also depends on the charge state of the ion absorbing a photon (see Aguilar et al. [45]). Lastly, it is also conceivable that the surrounding ions in the cluster influence the cross section of an atom or ion in the cluster.

The total cross section of atomic xenon at 13.5 nm is about 25 Mb.

The cross section of atomic argon at 13.5 nm, on the other hand, is much smaller. Figure 2.3(b) shows the total cross section of argon at 13.5 nm. According to West and Marr [41] it is only 1.4 Mb, smaller than the value for xenon by a factor of about 17. Consequently, a much higher intensity is necessary for argon to absorb the same number of photons as xenon. Since high charge states were observed in our experiments, it is instructive to look at the paths by which these high charge states are produced. For xenon atoms, this path has been depicted by Sorokin et al. [46], as shown in figure 2.4. The most basic information from the figure is

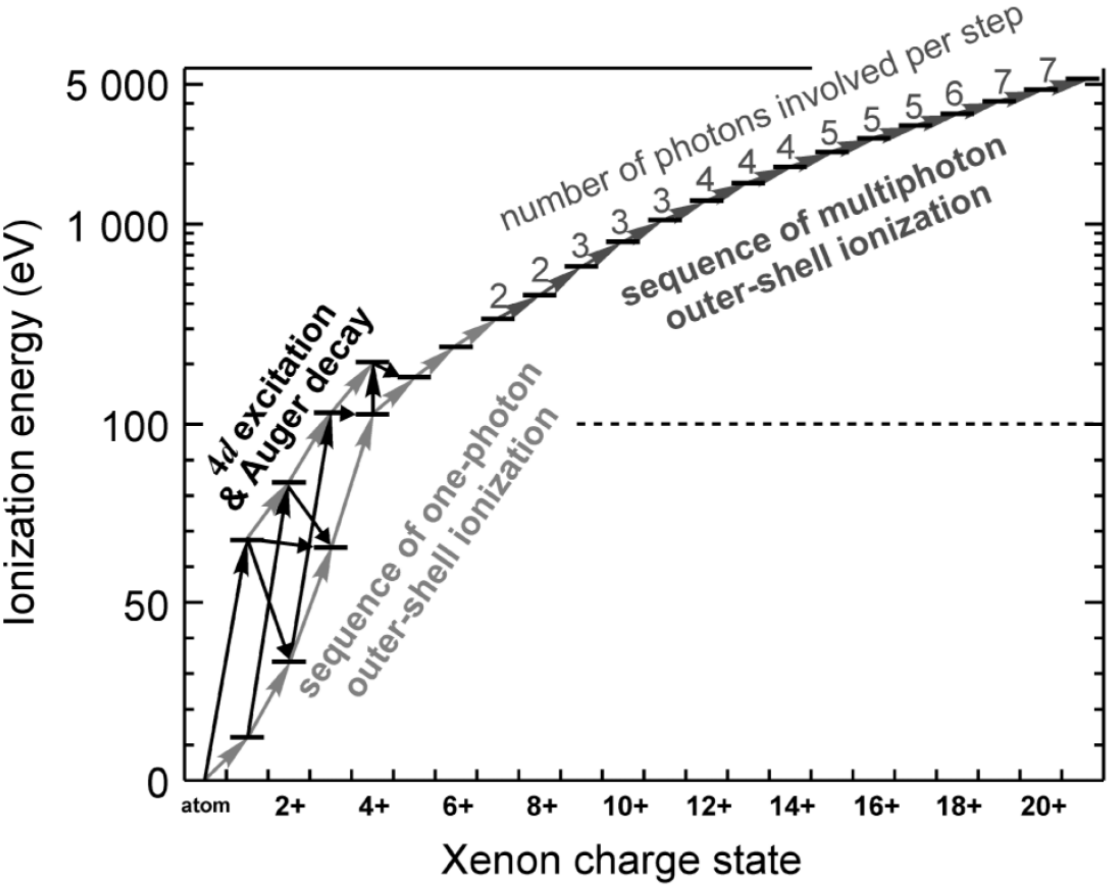

Figure 2.4.: Ionization scheme for xenon atoms ionized by light with a wavelength of 13.5 nm (from Sorokin et al. [46]). Low charge states can be reached in alternative ways. To produce Xe^{8+} at least 2 photons are needed. Xe^{10+} and Xe^{11+} require even three photons. It must be kept in mind that in clusters additional ways of ionization can play a role.

that charge states up to Xe^{5+} can be populated in two ways: either, as suggested by the giant resonance, by the ionization of an electron from the 4d-shell and a subsequent Auger decay or by the sequential absorption of single photons in the outer shell, each new charge state serving as a stepping stone to reach the next one. This sequence of one-photon outer-shell ionization works up to Xe^{7+} From there on, the energetic gap between charge states is too large to be bridged by a single photon. Charge states of 8+ and 9+ require the absorption of two photons, Xe^{10+}, Xe^{11+} and Xe^{12+} require even three photons. Higher charge states are not relevant for our experiments, which used maximum FEL intensities of $3 \cdot 10^{15}$ W/cm^2.

In the case of argon, only charge states up to Ar^{6+} can be reached by a sequence of one-photon outer-shell ionization, Ar^{7+} and Ar^{8+} require two photons [47].. Higher charge states would require even more photons but are not relevant at intensities of $3 \cdot 10^{15}$ W/cm^2.

This fact and the lower cross section of argon indicate that one should expect significantly lower charge states for argon than for xenon.

It is, however, important to note that these observations pertain to atoms. In clusters, additional mechanisms of energy absorption and ionization can occur, as will be shown in the next chapter.

2.4. Clusters exposed to strong XUV FEL pulses

The interaction of clusters and light is a very active research field. Laser wavelengths vary between X-ray and infrared and intensities over a very wide range have been used.
This chapter will only provide information pertaining to the conditions in our experiments, namely rare gas clusters interacting with strong XUV pulses, with comparison to other laser wavelength regimes where appropriate. Most of the information presented here can be found in the reviews by Fennel et al. [48] and Saalmann et al. [49]. These reviews also are a good starting point for anyone requiring a broader overview of clusters in strong laser pulses. References therein also deal with other intensity regimes.

2.4.1. Primary ionization processes

A cluster reacts to a strong laser pulse by being ionized. While this is true regardless of wavelength, the way the atoms are ionized is highly dependent on wavelength. Looking at individual atoms, there are two basic ways for ionization by a laser pulse: (i) An atom can absorb one or several photons. Subsequently, an electron is emitted. These processes are called single- and multi-photon ionization, respectively. The first work on multiphoton processes was written by Göppert-Mayer, who in 1931 predicted a process in which an atom absorbs two photons simultaneously [50]. According to perturbation theory, the reaction rate Γ_n of a multi-photon ionization which requires n photons is proportional to the product of the relevant cross-section σ_n and the laser intensity I to the nth power:

$$\Gamma_n \propto \sigma_n I^n \tag{2.9}$$

(ii) In very strong laser fields, however, there is the additional possibility of the laser field suppressing the atomic potential so that electrons can leave the atom. This process is called optical field ionization (OFI).
A useful parameter to determine which ionization process is dominant is the *ponderomotive potential* U_p. It describes the peak kinetic energy of an electron performing a quiver motion driven by the laser field. It is given by

$$U_p = \frac{e^2 E_0^2}{4 m_e \omega_{\mathrm{las}}^2}. \tag{2.10}$$

e is the charge of the electron, m_e is its mass, E_0 is the electric field strength of the laser field and ω_{las} is the angular frequency of the laser, related to the laser frequency ν_{las} by $\omega_{\mathrm{las}} = 2\pi\nu_{\mathrm{las}}$.
A more convenient formula is

$$U_p = 9.33 \cdot 10^{-14}\,\mathrm{eV} \cdot I_0\left[\mathrm{W/cm^2}\right] \cdot (\lambda[\mu\mathrm{m}])^2, \tag{2.11}$$

where I_0 is the laser intensity. It can easily be seen that U_p scales with the square of the laser wavelength, so if the laser wavelength decreases, U_p decreases quadratically.
The Keldysh adiabaticity parameter γ_{K} can be used to determine the dominant ionization mechanism.

$$\gamma_{\mathrm{K}} = \sqrt{\frac{E_{\mathrm{IP}}}{2U_p}}, \tag{2.12}$$

where E_{IP} is the ionization potential of the atom. For $\gamma_{\mathrm{K}} \gg 1$ single- or multi-photon ionization is the dominant process. For $\gamma_{\mathrm{K}} \leq 1$ optical field ionization dominates. In our experiments, the wavelength was 13.5 nm, with an intensity of up to $4 \cdot 10^{15}$ W/cm^2. Therefore, the ponderomotive potential is 0.068 eV. For xenon ($E_{\mathrm{IP}} = 12.13\,\mathrm{eV}$), this gives a Keldysh parameter of $\gamma_{\mathrm{K}} > 9$. For argon ($E_{\mathrm{IP}} = 15.76\,\mathrm{eV}$), the value is even larger. For the ionization of inner-shell electrons with larger E_{IP} the Keldysh parameter is larger still.

Obviously, at our experimental conditions, photoionization is the dominant process.

2.4.2. Inner and outer ionization and the formation of a nanoplasma

When an atom is ionized, the electron is no longer bound to the atom. In the case of a cluster, one has to distinguish between *inner* and *outer ionization*, a concept introduced by Last and Jortner [51]. Inner ionization describes the phenomenon of atoms within the cluster being ionized without the electrons leaving the cluster as a whole. This state of a delocalized electron cloud in front of an ion background is also often called a *nanoplasma*, a model developed by Ditmire et al. [52]. The term outer ionization consequently refers to electrons being emitted from the cluster.

Apart from the manner of ionization, presented in the previous section, the wavelength regimes also differ in their photon energy in relation to the ionization potential E_{IP}. For infrared wavelengths, the photon energy is lower than the ionization potential, so the electrons are first inner ionized before they are outer ionized at a later time, when they have gained additional energy from the laser field (see next section).

At a wavelength of 13.5 nm, a photon energy of about 90 eV, the photon energy is much larger than the ionization potential of argon or xenon. Therefore, electrons can be immediately outer ionized. After electrons have been emitted from the cluster, the cluster has a total charge Q. Assuming that the distribution of charges in the cluster is uniform, the cluster potential V in dependence on the radial distance r from the cluster center reads (see, for instance, Arbeiter and Fennel [53]):

$$V(r) = -\frac{e^2}{4\pi\epsilon_0} \begin{cases} \frac{Q}{2R}(3 - r^2/R^2) & \text{for } r \leq R, \\ \frac{Q}{r} & \text{for } r > R. \end{cases} \tag{2.13}$$

The electron charge is represented by e, ϵ_0 is the vacuum permittivity, Q is the cluster charge and R is the cluster radius.

Every outer ionization event deepens the potential which is formed by the remaining ions. At a certain charge Q the excess energy of the photoelectrons is no longer sufficient to leave the cluster, they are only inner ionized. Arbeiter and Fennel [54] refer to this state as the *frustration* of the cluster. Frustration starts at the cluster center and progresses outwards until it reaches the cluster surface.

As inner ionized electrons cannot overcome the cluster potential, they migrate to the cluster center, where the potential is deepest. The electrons are still not bound to individual atoms, only to the cluster as a whole. They are called *quasi-free*. In the cluster, the quasi-free electrons screen the cluster charge up to a radius R_{el}, which is given by (see Saalmann [8])

$$R_{\mathrm{el}} = \left(\frac{Q_{\mathrm{el}}}{Q_{\mathrm{ion}}}\right)^{1/3} R, \tag{2.14}$$

where Q_{el} is the overall charge of the quasi-free electrons, Q_{ion} is the overall charge of the ions in the cluster and R is the cluster radius. The overall charge Q of the cluster is given by $Q = Q_{\mathrm{ion}} - Q_{\mathrm{el}}$. This was also true for equation 2.13, but, as there were no quasi-free ions yet, Q_{el} was zero and the overall cluster charge Q was equal to Q_{ion}.
The cluster potential is modified in the following way (see Saalmann [8]):

$$V(r) = -\frac{e^2}{4\pi\epsilon_0} \begin{cases} \frac{Q}{2R}(3 - R_{\mathrm{el}}^2/R^2) & \text{for } r \leq R_{\mathrm{el}}, \\ \frac{Q}{2R}(3 - r^2/R^2) & \text{for } R_{\mathrm{el}} < r \leq R, \\ \frac{Q}{r} & \text{for } r > R. \end{cases} \tag{2.15}$$

From the cluster center to R_{el}, the quasi-free electrons screen the ion charges. This portion of the cluster is net neutral and therefore the potential in this region is constant. For the remaining cluster, the potential is harmonic, just as it was in equation 2.13 for the entire cluster. From the outside of the cluster, the potential is again a Coulomb potential.

2.4.3. Energy absorption and secondary ionization processes

Once atoms of the cluster have been ionized and there are quasi-free electrons within the cluster, additional heating mechanisms, i.e. processes which allow the transfer of energy from the laser to the cluster, and secondary ionization processes are made accessible. As was the case for the primary ionization mechanism, these secondary processes depend on the laser wavelength.
For wavelengths of about 800 nm, the most important mechanism by which energy is transferred from the laser field to the cluster is the following: the movement of the quasi-free electrons is characterized by an eigenfrequency. This eigenfrequency depends on the electron density which in turn depends on the radius of the cluster. When the cluster expands - which will be described in section 2.4.4 -, the electron density decreases and so does the eigenfrequency of the electron movement. As the electron density decreases, at some point, the eigenfrequency of the electron movement becomes resonant with the laser frequency which leads to a greatly enhanced absorption of energy and consequently to the production of high charge states in the cluster. This effect was shown experimentally by Zweiback et al. [55]. They also performed model calculations and presented the explanation of the eigenfrequency of the electrons becoming resonant with the laser frequency to explain their results. A theoretical explanation can also be found in the review by Saalmann et al. [49].
At 100 nm, the wavelength at which a first cluster experiment at FLASH was performed (see Wabnitz et al. [14]), another mechanism is responsible for the absorption of energy from the laser field, as was shown by Siedschlag and Rost [16], Santra and Greene [17] and Bauer [19]: *inverse bremsstrahlung* describes the process of electrons absorbing energy from photons while being scattered from ions. Additionally, Jungreuthmayer et al. [18] pointed out the importance of recombination processes of electrons and ions in the cluster. According to Georgescu et al. [56], inverse bremsstrahlung should remain the dominant absorption process down to a wavelength of 62 nm.
However, at 13.5 nm these secondary mechanisms of energy deposition do not play a significant role. The laser frequency is much higher than the eigenfrequency of the quasi-free electrons, so the two cannot become resonant during the cluster expansion. Also, the importance of

inverse bremsstrahlung decreases significantly for increasing laser frequency because it is proportional to $\omega_{\mathrm{las}}^{-8/3}$ (see Krainov [57]). Calculations by Ziaja et al. [58] show that already at 32 nm inverse bremsstrahlung contributes to the total energy absorption of argon clusters by at most 2 %. The ionization proceeds for by *multistep ionization*, i.e. sequential direct emission of Auger and photo-electrons into the continuum (see Bostedt et al. [59, 60], Gnodtke et al. [61, 62]). According to Bostedt et al. [60], the nanoplasma gains energy predominantly through the addition of inner ionized electrons. These electrons, which have an excess energy of $\hbar\omega_{\mathrm{las}} - E_{\mathrm{IP}}$, equilibrate thermally. A Maxwell-Boltzmann-energy-distribution is formed. The hottest electrons can gain enough energy to overcome the cluster potential and escape from the cluster (see Ziaja et al. [58], Bostedt et al. [60], Arbeiter and Fennel [53] and Gnodtke et al. [62]).

All the excitation wavelength regimes mentioned have in common that a nanoplasma of quasi-free electrons can be formed inside the cluster. Apart from being essential at longer wavelengths for the absorption of energy from the laser (via inverse bremsstrahlung or the plasma frequency becoming resonant with the laser frequency), the quasi-free electrons can also excite or ionize atoms by *inelastic scattering* and *electron impact ionization*, respectively. Either of the processes can happen when a quasi-free electron collides with an electron still bound to an atom. In the case of inelastic scattering, the bound electron gains energy and is promoted to an excited state but is still bound to the atom. In the case of electron impact ionization, the bound electron is ionized.

Another important ionization mechanism is *field ionization*[3] (see Gnodtke et al. [61]). This space charge of ions in the cluster generates strong fields, especially at the cluster surface, which cause the ionization of further electrons. These electrons migrate to the cluster center.

2.4.4. Cluster expansion and destruction

Whatever the exact mechanism of ionization is, once the ionization has started, the multiply-charged cluster is destined to be destroyed. The most straightforward way for this to happen is *Coulomb explosion*. This term refers to the expansion of the cluster driven by the repelling forces between the ions. As soon as ions have been created, the cluster begins to expand. The timescale of the expansion can be estimated by assuming a cluster of a size characteristic for its neutral state but with an average charge $\langle q \rangle$ per atom. The time in which the cluster doubles its radius is then given by (see [48]):

$$\tau_{\mathrm{doub}} \approx \frac{2.3(\sqrt{2\pi\epsilon_0}/e)m_{\mathrm{ion}}^{1/2} r_{\mathrm{s}}^{3/2}}{\langle q \rangle}, \tag{2.16}$$

where m_{ion} is the mass of the ion and r_{s} is the initial Wigner-Seitz-radius of the atom

$$r_{\mathrm{s}} = \left(\frac{3M}{4\pi\rho N_A}\right)^{1/3}, \tag{2.17}$$

where M is the molar mass, ρ is the mass density and N_A is the Avogadro constant. The Wigner-Seitz-radius is the radius of a sphere which represents the average volume of an atom in a solid (see, for instance, [63]). If one assumes the cluster to have the density of a solid,

---

[3] not to be confused with optical field ionization (described in chapter 2.4.1), which only plays a role at much longer wavelengths

one can calculate τ_{doub} for argon and xenon. For argon, τ_{doub} is approximately $90\,\text{fs}/\langle q\rangle$, for xenon, τ_{doub} is approximately $190\,\text{fs}/\langle q\rangle$.

There are also experimental results, for instance by Thomas et al. [20], and theoretical predictions, for instance by Ziaja et al. [64], which indicate that, under certain conditions, the cluster does not disintegrate by Coulomb explosion but rather via a so-called *hydrodynamic expansion*. This mode of disintegration happens if the cluster is net neutral, that is if the quasi-free electrons shield the ions. Nevertheless, an expansion takes place because the electrons are energetic. This results in an electron pressure. The hydrodynamic pressure p_e of the electrons, which are treated as an ideal gas of temperature T_e and an internal energy $E_{\text{int}} = 3N_e k_b T_e/2$, is given by (see Ditmire et al. [52]):

$$p_e = n_e k_b T_e \tag{2.18}$$

N_e is the number of electrons, n_e is the electron density and k_b is the Boltzmann constant.

The hydrodynamic pressure of the electrons leads to an expansion of the electron gas. The expanding electrons drag the ions with them (Ditmire et al. [52]). According to Krainov and Smirnov [65], the time τ_{hd} after which the cluster radius has doubled is given by

$$\tau_{\text{hd}} \approx R_0 \left(\frac{m_{\text{ion}}}{\langle q\rangle k_b T_e}\right)^{1/2}, \tag{2.19}$$

where R_0 is the initial cluster radius, m_{ion} is the ion mass, $\langle q\rangle$ is the average charge state per atom, k_b is the Boltzmann constant and T_e is the temperature of the electron gas. Hydrodynamic expansion is usually significantly slower than Coulomb explosion, but depends on the size of the cluster and the energy of the electrons.

In general, rather than expanding by pure Coulomb explosion or pure hydrodynamical expansion, the cluster expands in a combination of both processes. As was described above, a thermally equilibrated nanoplasma can form within the cluster. The most energetic electrons in the hot electron gas can leave the cluster. The remaining electrons migrate to the cluster center, thereby freeing the outermost shell of ions to explode off via Coulomb explosion. The remaining electrons continue to expand hydrodynamically and the process is repeated since the Coulomb barrier decreases during the expansion.

For the regime of excitation energies between 20 eV (62 nm) and 90 eV (13.8 nm), where the dominant ionization process is multistep ionization, Arbeiter and Fennel [54] introduced the frustration parameter α_f, which can be used to estimate whether the experimental conditions will lead to the cluster being destroyed by Coulomb explosion or by hydrodynamic expansion.

$$\alpha_f = \frac{\widetilde{N}_{\text{tot}}}{q_{\text{full}}} \tag{2.20}$$

$\widetilde{N}_{\text{tot}}$ is the total number of photoactivated electrons[4], depending on the laser intensity I_0, the pulse duration τ of the laser pulse, the atomic cross section σ for the dominant ionization channel, the number N of atoms in the cluster and the photon energy $\hbar\omega_{\text{las}}$:

$$\widetilde{N}_{\text{tot}} = \frac{I_0 \tau \sigma N}{\hbar\omega_{\text{las}}} \tag{2.21}$$

---

[4] Arbeiter and Fennel use the term photoactivation to refer to all electrons - outer and inner ionized - which are produced by photoionization.

q_{full} describes the number of possible direct photoelectrons that can be emitted before the so-called *full frustration* sets in. This term refers to the state of so many electrons having been emitted from the cluster that the Coulomb potential of the cluster prevents any direct photoelectrons or Auger electrons from leaving the cluster as a whole. The frustration starts in the cluster center and progresses outwards. q_{full} is derived by finding the number of outer ionizations after which the excess energy $(\hbar\omega_{\text{las}} - E_{\text{IP}})$ of the ionized electrons (E_{IP} is the ionization potential of the dominant ionization channel) is equal to the cluster potential seen from the outside of the cluster (see the second part of equation 2.13). The cluster radius R is replaced by $R = r_{\text{s}}N^{1/3}$. r_{s} is the Wigner-Seitz radius (see formula 2.17). N is the number of atoms in the cluster.

This equation yields

$$q_{\text{full}} = \frac{4\pi\epsilon_0}{e^2}(\hbar\omega_{\text{las}} - E_{\text{IP}})r_{\text{s}}N^{1/3} \tag{2.22}$$

In [54], the formula is given in the more convenient units eV and Å:

$$q_{\text{full}} = \frac{(\hbar\omega_{\text{las}} - E_{\text{IP}})r_{\text{s}}N^{1/3}}{14.4\,\text{eV Å}}, \tag{2.23}$$

Consequently, a value of $\alpha_f \lesssim 1$ identifies a regime of mostly direct photoionization. A nanoplasma begins to form as soon as α_f becomes larger than 1. Strong nanoplasma formation is characterized by $\alpha_f \gg 1$. A strong nanoplasma formation causes a primarily hydrodynamical expansion of the cluster, but it is important to keep in mind that the emission of electrons from the cluster - initially via direct photoionization and later on by the heating of the nanoplasma described in chapter 2.4.3 - leads to a nanoplasma which has a smaller diameter than the cluster itself. Therefore, the outer shells of the cluster, which are not shielded by quasi-free electrons, disintegrate via Coulomb explosion even for the case of $\alpha_f \gg 1$, whereas the core expands hydrodynamically.

Our experimental conditons will be described in detail in chapter 4. I will give a short outlook here to be able to calculate the frustration parameter for our experimental conditions. The intensity reached values between $5 \cdot 10^{13}$ W/cm^2 and $2.5 \cdot 10^{15}$ W/cm^2. The pulse duration was 150 fs. The photon energy $\hbar\omega_{\text{las}}$ was fixed at 92 eV. The remaining parameters are element-specific. For xenon, average cluster sizes N were varied between about 250 and 19000 atoms. Average cluster sizes of argon were varied between about 40 and 6000 atoms. Assuming a solid density of the clusters, the Wigner-Seitz radius r_s of xenon is 2.4 Å; for argon, r_s is 2.1 Å.

Lastly, to be able to calculate the frustration parameter, we need to know which electron is predominantly ionized. According to Arbeiter and Fennel [54], for argon the dominant ionization channel is the $3p$-electron with a cross section σ of 1.2 Mb and an ionization potential E_{IP} of 15.76 eV. For xenon, the dominant ionization channel is the $4d$-electron with a cross section of 25 Mb. Arbeiter and Fennel assume in their calculations for xenon that each photoionization event is followed by the ejection of an Auger electron. In other words, each photon effectively frees two electrons from an atom. Therefore, for xenon the value for $\widetilde{N}_{\text{tot}}$ has to be doubled. Instead of the excess energy $(\hbar\omega_{\text{las}} - E_{\text{IP},4d})$ of the $4d$-photoelectron, Arbeiter and Fennel use the larger excess energy of the Auger electron (33 eV) in the case of xenon. Details on relaxation processes such as Auger decay will be given in section 2.5.

The lowest frustration parameter reached in our experiments was for argon, with a cluster size of 400 atoms and an FEL intensity of $5 \cdot 10^{13}$ W/cm^2. With these values, the resulting α_f is approximately 2.8. While this result is only slightly larger than 1, it nevertheless means that we can expect frustration of the cluster even at these conditions. For intensities of $2.5 \cdot 10^{15}$ W/cm^2,

α_f is already about 142. For xenon, values are significantly larger still: at an intensity of $2.5 \cdot 10^{15}$ W/cm^2 and an average cluster size of 6700 atoms, a value used in many of our scans, the resulting α_f is over 80000.
In summary, the important outcome of these estimates is that we expect frustration of the cluster throughout the entire range of experimental parameters. Therefore, the disintegration of clusters should always proceed by a combined process of Coulomb explosion of outer shells and a hydrodynamic expansion of the core.

2.4.5. Energy redistribution within the cluster

As the laser pulse gets weaker and finally ends, the direct photoionization process stops. Energy within the cluster may be redistributed. In particular, an experiment by Hoener et al. [9] could show that it is highly likely that ions within the core of the cluster *recombine* with electrons. Hoener et al. could show this by means of mass spectroscopy. They studied so-called *core-shell clusters*, consisting of a xenon core and a surrounding argon shell and compared them with pure xenon clusters. The clusters were excited resonantly with focused FLASH pulses at 13.7 nm, making high initial charging of the xenon core almost certain. The resulting cluster fragments were detected with an ion-TOF. In pure xenon clusters, Hoener et al. found charge states up to $9+$ at peak intensities exceeding 10^{14} W/cm^2. Surprisingly, in the core-shell clusters the highest xenon charge states detected in the TOF spectra were only $2+$. Their findings are also corroborated by theoretical calculations by Jungreuthmayer et al. [18], Ziaja et al. [64, 66] and Arbeiter and Fennel [54] which show that it is essential to incorporate recombination processes into theoretical models to reproduce the experimental results for clusters studied with XUV pulses at FLASH.
In other words, an inherent limitation of TOF spectroscopy is that only the final products of the initial reaction are detected, microseconds after that reaction took place. In this time, higher charge states could form and recombine, without any possibility to detect them by TOF spectroscopy. Fluorescence, which will be studied in the next section, offers the possibility to observe more than just the end-products of such reactions.

2.5. Fluorescence and other relaxation mechanisms

Starting at the simple case of fluorescence in an isolated atom or ion, figure 2.5 shows the most common excitation processes, photoabsorption and electron impact. As was explained, these are the most important ionization mechanisms for intense XUV pulses, while at infrared wavelengths optical field ionization dominates.
Both these processes can provide the prerequisite for fluorescence, namely a vacancy in any other than the outermost shell. An electron from a higher shell can now fill the vacancy, emitting its excess energy as a photon (figure 2.5 (c)). The energy of the photon emitted as fluorescent radiation depends on the difference in energy between the participating electron shells.
However, there are alternative ways for the atom to fill the vacancy and return to the state of lowest energy: the most important one is the Auger process shown in figure 2.5 (d): once again, an electron fills the vacancy, but in this case, the excess energy is transferred to another electron, not necessarily from the same shell, which is emitted from the atom. No radiation is emitted during an Auger process.
Obviously, the two are competing processes. Either a fluorescence photon or an Auger electron is emitted, but not both. The relative weight of the processes depends on the atomic number

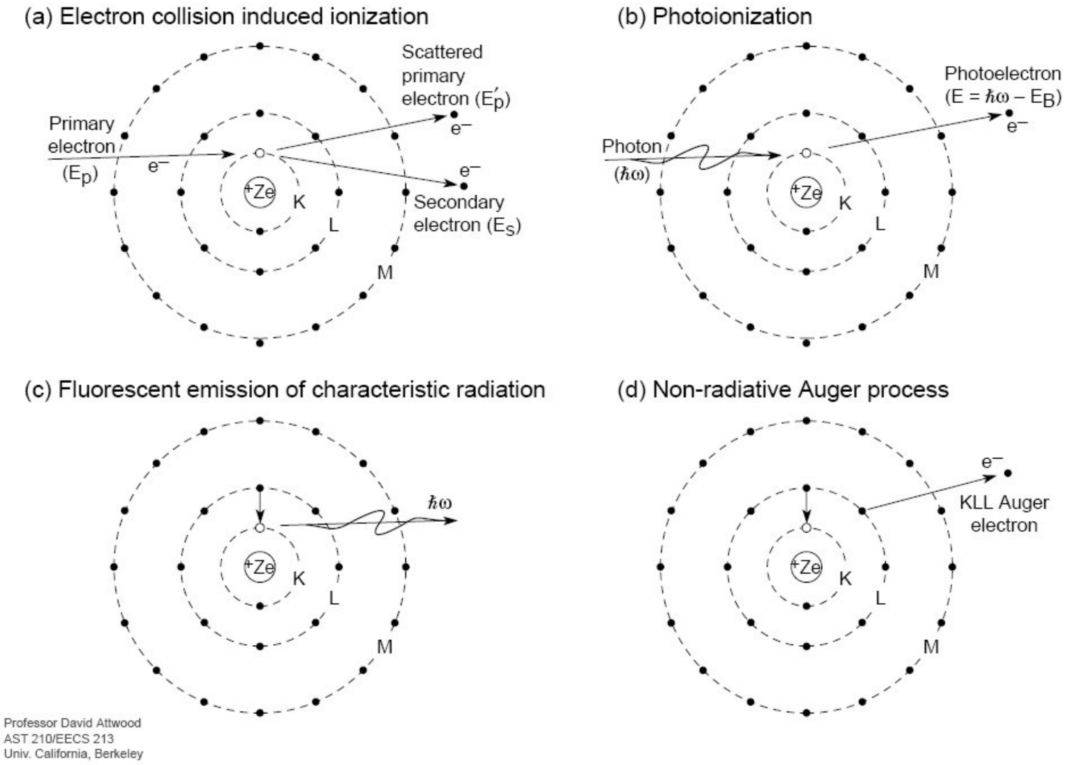

Professor David Attwood
AST 210/EECS 213
Univ. California, Berkeley

Figure 2.5.: The simplest excitation and relaxation processes in an isolated atom (from Attwood [1]).

of the elements and on the electronic shells involved, as can be seen in figure 2.6. The general trend is clear: for the K-shell, Auger processes are absolutely predominant for low atomic numbers and fluorescence radiation predominates for high atomic numbers. The crossing point occurs at an atomic number of about 30. The trend for the L_3-subshell is essentially the same, but the crossing point is shifted towards higher values of the atomic number. Consulting the NIST database [67], it becomes clear that for the elements under investigation in our experiments - argon (atomic number 18) and xenon (atomic number 54) - we are not dealing with K-shell radiation but with L- and M-shell radiation for argon and even N- and higher shells for xenon at the wavelengths we investigated. Assuming the trend of figure 2.6 continues for these shells, Auger processes are heavily favored at the expense of fluorescence. Fluorescence radiation emitted from clusters has already been studied by several groups. McPherson et al. [10] reviewed experiments studying fluorescence around 10 nm from krypton, argon and xenon irradiated with intense 248 nm-radiation. By comparing the results obtained in these experiments with other published work and with a theoretical model, they could show that the observed charge states of Kr^{9+}, Ar^{9+} and Xe^{9+} are inaccessible at the experimental conditions if atomic targets are used. They showed that the results could be explained if the targets had been small clusters, thereby showing that additional ionization processes, electron impact ionization in their model, can take place in clusters. Another experiment at a similar wavelength was published by Ditmire et al. [68], who studied fluorescence radiation of large argon and krypton clusters between about 2 and 10 nm. Other fluorescence spectra from xenon plasmas in this wavelength range were not created by means of ionizing clusters with intense laser radiation but by dense plasma discharge plasmas and capillary discharge plasmas, respectively. Examples include the papers by Böwering et al. [69], Klosner and Silfvast [70] and Sobelman et al. [71]. There are similarities between spectra created in this way and those measured in the experiments of this thesis. The wavelength calibration in section 4.1.1 will make use of this fact.

Other experiments concentrated on hard X-ray fluorescence. An early experiment was performed

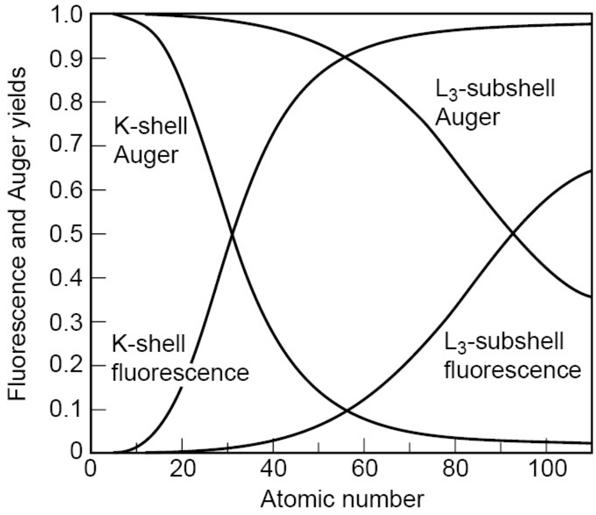

Figure 2.6.: Fluorescence and Auger decay yields depending on atomic number Z. For low atomic numbers the Auger decay is the dominant process by far. (From [1])

by McPherson et al. [11], who observed X-ray fluorescence between about 4 and 5 keV, or 0.2 and 0.3 nm, after irradiating xenon clusters with intense light at a wavelength of 248 nm. Other works were, for instance, Rozet et al. [72] (X-ray fluorescence between about 3 and 3.2 keV, about 0.39 and 0.41 nm, from Ar-, Kr- and Xe-clusters) and Skobelev et al. [73] (X-ray fluorescence between about 3 and 3.8 keV, about 0.33 and 0.42 nm, from Ar-clusters). All of the above works used laser wavelengths in the infrared or ultraviolet wavelength range, i.e. far lower photon energies than in the experiments described in this thesis.

Very recently, results of an experiment where argon clusters were illuminated by XUV light from the Japanese EUV-FEL facility SCSS test accelerator facility were published. Iwayama et al. [74] irradiated argon clusters with an FEL wavelength of 51 nm. The FEL intensity in the focus was about $3 \cdot 10^{13}$ W/cm^2. They measured the fluorescence yield between 15 and 62 nm in dependence on cluster size. The stagnation pressure was kept constant at a value which led to an average cluster size of 100 atoms. The cluster size in the interaction region, however, was varied by choosing different distances of the cluster source to the interaction region. This method takes advantage of the fact that the formation of the clusters requires a certain travel range of the atoms. According to the paper, at the minimum chosen distance of 0.5 mm distance, no clusters have formed and the sample in the interaction region consists only of atoms. At a distance of 5 mm clusters of an average size of 100 atoms are expected to have formed.

Their results are shown in figure 2.7. The fluorescence yield has been normalized with respect to the argon particle number density, which is proportional to D^{-2}, where D is the distance from the cluster source to the interaction region. This is clearly apparent in the fluorescence spectra for distances of 10 and 15 mm: as the particle number density is low for these distances, the signal to noise ratio is far worse than for the other spectra. The central finding of the paper is that fluorescence wavelengths shorter than the FEL wavelength are observed.

It must be noted that the second point, which is called up-conversion in the paper, is not exclusively a cluster effect as it already appears in a purely atomic sample at $D = 0.5$ mm. Another interesting point, which is not addressed by the authors, is the different evolution of spectral lines in dependence on cluster size. Furthermore, the ratio of line strengths continues to change for large nozzle distances, even though the authors claim that the cluster formation has finished at $D = 5$ mm.

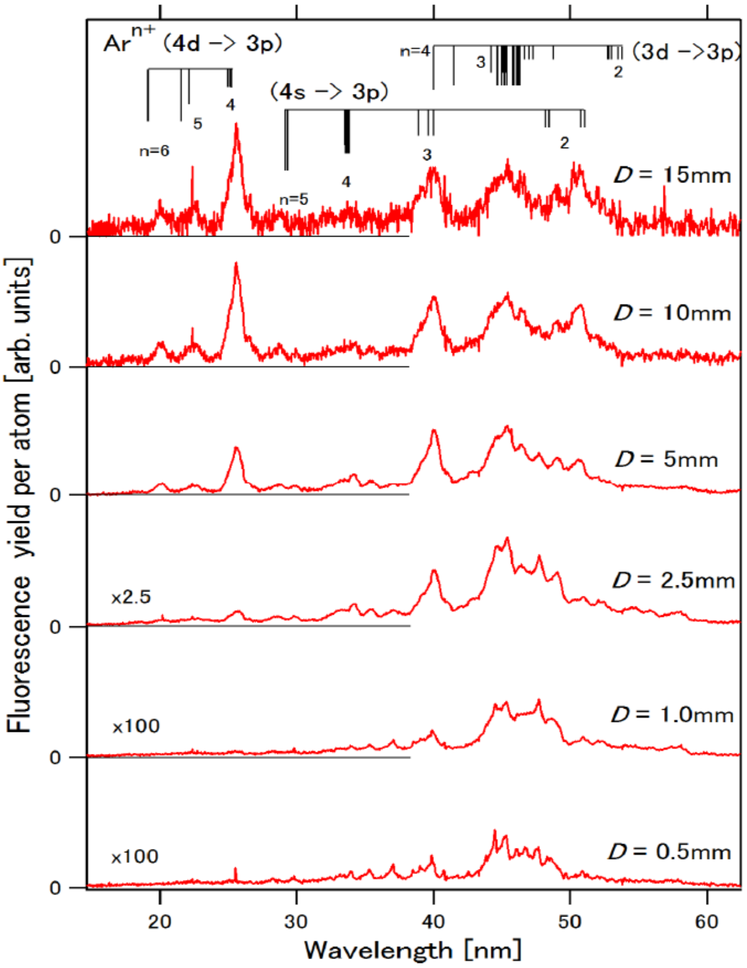

Figure 2.7.: Fluorescence of Ar clusters of different sizes, measured by Iwayama et al. [74] at an excitation wavelength of 51 nm. The cluster size was varied by varying the distance D of the cluster source to the interaction region. At $D = 0.5$ mm the target is expected to consist only of atoms, whereas at $D = 5$ mm the final cluster size of 100 atoms per cluster (on average) is expected to have formed. The fluorescence yield has been normalized with respect to the argon particle number density, which is proportional to D^{-2}.

2.5.1. Atomic energy levels, selection rules and spectroscopic notation

Atomic energy levels

This section is meant to be a reminder of the notation used to describe the electronic structure of an atom and the allowed transitions between different states. The complete theory behind these rules can be found in textbooks about atomic physics, for instance in the book by Bransden and Joachain [75].

The simplest possible atom, the hydrogen atom, is a good example to introduce *quantum numbers*. The quantum number n describes the energy of the electron, also called the *shell* which the electron occupies. n can take any integer value of 1 or above.

The quantum number l describes the angular momentum of the system. Possible values for l are $0 \leq l \leq n - 1$. States which share the same values for n and l constitute a *subshell*.

The magnetic quantum number m_l is defined by the projection of the angular momentum along the z-axis. m_l can have any integer value from $-l$ to $+l$.

The last quantum number is the spin projection number m_s. For an electron, which has a spin

of $1/2$, m_s can be either $-1/2$ or $+1/2$.
All quantum numbers are needed to fully describe the state of the atom. Alternatively, a single-electron-atom can also be described by the quantum numbers n, l, j and m_j. j is the quantum number describing the total angular momentum, m_j is its projection along the z-axis. For a given value of l and s, j can take the following values: $|l-s|$, $|l-s|+1$,..., $l+s$. For hydrogen, this leaves $l \pm 1/2$. m_j can take values from $-j$ to $+j$, spaced by 1.

Selection rules

Dipole-allowed transitions between two electronic states have to obey the following selection rules:

$$\Delta l = l - l' = \pm 1 \tag{2.24}$$

$$\Delta m = m - m' = 0,\ \pm 1 \tag{2.25}$$

$$\Delta n = n - n' \text{ is arbitrary} \tag{2.26}$$

The selection rules can be derived from the case of an atom interacting with an external radiation field (see for instance Bransden and Joachain [75]). Two important approximations are made in this derivation. Firstly, the external radiation field is treated as a small perturbation of the atomic Hamiltonian. This should be a valid approximation in the case of our experiments, because, even though the FLASH pulse is very strong, the dominant excitation mechanism is the absorption of single photons, as was shown in chapter 2.4.1. It is in any case a valid approximation for the *deexcitation* of the states. At this point in time, the FLASH pulse is no longer present. Instead, the external radiation field is that of the fluorescence photons, which clearly can be treated as a small perturbation.
The second approximation made is the so-called *dipole approximation*. The transition probability between two states ψ_b and ψ_a depends on the so-called *matrix element* M_{ba}.

$$M_{ba} = \langle \psi_b | \exp(i\boldsymbol{k}\boldsymbol{r})\hat{\boldsymbol{\epsilon}}\boldsymbol{\nabla} | \psi_a \rangle = \int \psi_b^*(\boldsymbol{r}) \exp(i\boldsymbol{k}\boldsymbol{r})\hat{\boldsymbol{\epsilon}}\boldsymbol{\nabla}\psi_a(\boldsymbol{r})d\boldsymbol{r} \tag{2.27}$$

i is the imaginary unit, $\boldsymbol{k}$ is the wave vector, defined by $|\boldsymbol{k}|$ and pointing in the direction the light wave is traveling, $\hat{\boldsymbol{\epsilon}}$ is a unit vector perpendicular to $\boldsymbol{k}$ and $\boldsymbol{\nabla}$ is the Nabla operator.
The exponential factor can be expanded in the following form:

$$\exp(i\mathbf{k}\boldsymbol{r}) = 1 + (i\mathbf{k}\boldsymbol{r}) + \frac{1}{2!}(i\mathbf{k}\boldsymbol{r})^2 + ... \tag{2.28}$$

In the dipole approximation, all summands but the 1 are neglected. Thus, the general matrix element M_{ba} is replaced by the *dipole matrix element* M_{ba}^{D}.

$$M_{ba}^{\mathrm{D}} = \hat{\boldsymbol{\epsilon}} \langle \psi_b | \boldsymbol{\nabla} | \psi_a \rangle \tag{2.29}$$

In practical terms, this approximation corresponds to a neglection of the spatial variation of the radiation field across the atom. This is valid if the wavelength is much larger than the extension a of the atomic wave function, which is on the order of $0.1\,\mathrm{nm}$. Consequently, even for the

lowest wavelength in our experiments of 10 nm, $\lambda/a \approx 100$ and the dipole approximation is valid.
Using the dipole approximation, it turns out that the transition probabilities for absorption, stimulated emission and spontaneous emission all depend on the quantity $|\hat{\boldsymbol{\epsilon}}\boldsymbol{r}_{ba}|^2$. Expressing this quantity in spherical components leads to integrals which depend on the quantum numbers n, l and m. It can be shown that these integrals are only non-vanishing for the cases defined by the selection rules defined in equations 2.24, 2.25 and 2.26.

Spectroscopic notation

For atoms with many electrons, there is a special notation used in spectroscopy, according to the following scheme: $nl^{2S+1}L_J$. n is the principal quantum number as introduced above, but l is replaced by a letter code. $l = 0$ is denoted by the letter s, $l = 1$ is p, $l = 2$ is d, $l = 3$ is f. From then on, the scheme continues alphabetically, omitting j. The letter is followed by a superscript which shows the number of electrons in this subshell. As an example, the configuration of carbon in its ground state would be written as follows: $1s^2 2s^2 2p^2$. The Pauli exclusion principle states that no fermions in an atom can occupy the same quantum state, in other words they cannot have the exact same quantum numbers. Therefore, the maximum number of electrons which can be in the same subshell is $2(2l + 1)$, so for carbon, the s-shells are complete, while the p-shell could accomodate 4 more electrons.
To completely determine the state of the atom, more quantum numbers are needed, therefore the nl-notation is supplemented by a term of the form ${}^{2S+1}L_J$. L denotes the total orbital angular momentum. It again follows the letter code explained above, only with capital letters in this case, so $L = 0$ is S, $L = 1$ is P and so on. For all complete subshells, the only possible value is $L = 0$, again due to the Pauli exclusion principle. For two electrons with orbital angular momentum l_1 and l_2, respectively, the possible values for L are easily calculated. The minimum value is $|l_1 - l_2|$, the maximum value is $l_1 + l_2$. All integer values between these are also possible. For more than two electrons, one simply starts by calculating L for two electrons, beginning with those from the same subshell, and then adding the resulting values of L according to the same rules.
The superscript ${}^{2S+1}$ gives the so-called *multiplicity*. S is the quantum number for the *total* spin. For an atom with a single electron, this number is always $1/2$. For an atom with multiple electrons, more combinations of $-1/2$ and $+1/2$ are possible. As a consequence of the Pauli exclusion principle, filled subshells have $S = 0$, as the spins of the electrons cancel out. Also, any subshells which are more than half full necessarily contain electrons whose spin must cancel. Therefore, the maximum multiplicity can be reached for a subshell which is exactly half-filled. For instance, 3 electrons in p-subshells can have $S = 3/2$ or $S = 1/2$, which results in a multiplicity of 4 and 2, respectively. A p-subshell with 4 electrons, on the other hand, can only have $S = 1$ or $S = 0$, resulting in a multiplicity of 3 and 1, respectively.
However, one has to pay attention to the fact that all combinations of the multiplicity and L are only possible if the electrons are not from the same subshell. If the electrons occupy the same subshell, the Pauli exclusion principle restricts the possible combinations. Constructing the possible states gets tedious and is not needed in detail to understand this thesis. The procedure can be found in the book by Bransden and Joachain [75]. A helpful rule is that the allowed states for a subshell with x electrons are the same as for one in which x electrons are missing. To continue with 3 electrons in p-subshells, if all electrons belong to the same subshell, the only possible combinations of multiplicity and L are ${}^4S$, ${}^2P$ and ${}^2D$. If all p-electrons occupy different shells, the possible values are ${}^2P$, ${}^2D$, ${}^2F$, ${}^4P$, ${}^4D$ and ${}^4F$.
J denotes the total angular momentum. It can take the following values: $|L-S|$, $|L-S|+1$,..., $L + S$.

Finally, the parity of the term can be denoted by an 'o' as a superscript if the parity is odd, as in the state $5s^2 5p\ ^2P^{\mathrm{o}}_{1/2}$. The parity of the state is odd, if there is an odd number of electrons in subshells with an odd value of l.

On a theoretical level, the parity operator $\hat{P}$ acting on a wave function $\psi(\boldsymbol{r})$ describes the following relation:

$$\hat{P}\psi(\boldsymbol{r}) = \psi(-\boldsymbol{r}) \tag{2.30}$$

If $\psi(\boldsymbol{r}) = \psi(-\boldsymbol{r})$, ψ is said to have *even parity*. If $\psi(\boldsymbol{r}) = -\psi(-\boldsymbol{r})$, ψ is said to have *odd parity*. The electric dipole operator, which in the electric dipole approximation is responsible for transitions between states, only connects states of opposite parity. This is another way of stating the selection rule $\Delta l = l - l' = \pm 1$. Since each transition changes the number of electrons in subshells with an odd value of l by 1, the parity of the state has to change which each transition (according to the dipole approximation).

2.5.2. Timescale

The fluorescence lifetime τ_{rad} is a crucial parameter in describing the decay of an excited state [75]:

$$N(t) = N_0 \cdot \exp\left(-t/\tau_{\mathrm{rad}}\right) \tag{2.31}$$

From this formula, it is evident that after a time $t = \tau_{\mathrm{rad}}$ has passed, the population of the excited state has dropped from N_0 to N_0/e. Figure 2.8 shows a schematic plot of this behavior. The important point to note is that, even though it takes a certain amount of time until only a population of N_0/e is left, fluorescence photons can be emitted instantly once the prerequisite state is present. The lifetime depends on the transition rate W^{s}_{ab} for spontaneous emission in the following way (see Bransden and Joachain [75]):

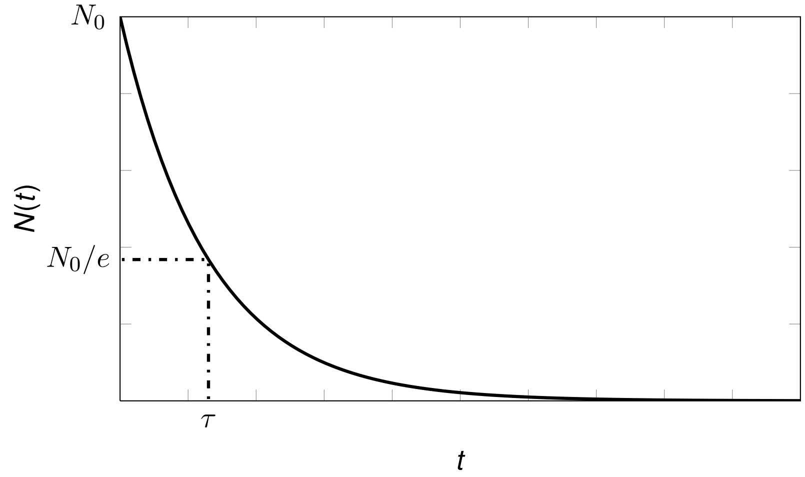

Figure 2.8.: Schematic representation of formula 2.31, showing the dependence of the population N of a fluorescing state on time t.

$$\frac{1}{\tau_{\text{rad}}} = \sum_k W_{kb}^{\text{s}} \tag{2.32}$$

The sum is over all values k which have a lower energy than the state b and are allowed by the selection rules. In the dipole approximation, W_{ab}^{s} is given by (see Bransden and Joachain [75]):

$$W_{ab}^{\text{s,D}} = \frac{4}{3\hbar c^3}\left(\frac{1}{4\pi\epsilon_0}\right)\omega_{ba}^3 |\boldsymbol{D}_{ba}|^2 \tag{2.33}$$

ω_{ba} is the angular frequency of the transition, given by $\frac{1}{\hbar}(E_b - E_a)$, where E_b and E_a are the energies of the upper and the lower level, respectively. $\boldsymbol{D}_{ba}$ is the *electric dipole moment matrix element*, related to the dipole matrix element M_{ba}^{D} defined in equation 2.29 by (see Bransden and Joachain [75]):

$$M_{ba}^{\text{D}} = \frac{m_e \omega_{ba}}{\hbar e}\hat{\boldsymbol{\epsilon}}\boldsymbol{D}_{ba}, \tag{2.34}$$

where m_e is the mass of the electron, e is the electron charge and $\hat{\boldsymbol{\epsilon}}$ is a unit vector in the direction of the polarisation of the electric field.

An important point to note is that the lifetime is proportional to ω_{ba}^{-3}. With this dependence, one can estimate the lifetime of the fluorescing states of xenon or argon by comparing them to the lifetime of a hydrogen level. The lifetimes of hydrogen are well known, as they can be calculated. The $2p$ level has the shortest lifetime, about 1.6 ns (see, for instance, Bransden and Joachain [75]). The wavelength of this transition, the Lyman-α line, is about 125 nm. Taking the ω_{ba}^{-3}-dependence of the lifetime from equation 2.33, we can estimate the lifetime of the shortest wavelength observable with our spectrometer (10 nm):

$$\frac{\tau_{10\,\text{nm}}}{\tau_{\text{L}\alpha}} \approx \frac{\omega_{ba\ 10\,\text{nm}}^{-3}}{\omega_{ba\ \text{L}\alpha}^{-3}} \Rightarrow \tau_{10\,\text{nm}} \approx \frac{\omega_{ba,\text{L}\alpha}^{3}}{\omega_{ba,10\,\text{nm}}^{3}}\tau_{\text{L}\alpha} = \left(\frac{10\,\text{nm}}{125\,\text{nm}}\right)^3 \tau_{\text{L}\alpha} \approx 1\,\text{ps} \tag{2.35}$$

Obviously, this calculation is far from exact, as it assumes identical electric dipole moment matrix elements for all elements. It gives, however, a rough estimate for the timescale on which the fluorescence of short wavelengths can occur. There are also additional effects, which are not considered in this estimate, which will be described in the following.

There is another scaling law, which describes the dependence of the lifetime of excited states of *hydrogenic ions*[5] on the nuclear charge Z (see Bransden and Joachain [75]):

$$\tau(Z) = Z^{-4}\tau_{\text{Hydrogen}} \tag{2.36}$$

Qualitatively, this equation shows that the lifetime of an electronic state becomes shorter as the influence of the nuclear charge becomes higher. Even though the ions observed in our studies are far from being hydrogenic, I would nevertheless expect a shortening effect on the lifetime of xenon and argon as a function of the charge state q of an atom. The higher the charge state, the higher the charge 'seen' by the electron.

The lifetimes of all fluorescent lines are reflected in the width of their spectral lines, because the natural linewidth Γ is given by $\Gamma = \hbar/\tau_{\text{rad}}$. If the lifetimes get shorter, the lines will get

---

[5] i.e. ions which have only one electron

broader. This is a manifestation of the uncertainty principle $\Delta t \Delta E \gtrsim \hbar$.

Equation 2.31 is only correct for a single, static, isolated atom. There are, however, two kinds of effects which can lead to a broadening of spectral lines. The following information can be found in the books by Griem [76] and Sobel'man, Vainshtein and Yukov [77]. The first effect, *Doppler broadening*, is caused by the wavelength shift which occurs if the source is moving. In a gas with a certain temperature or in a Coulomb-exploding cluster, there are atoms present which move away from the observer as well as atoms which move towards the observer, thereby not causing a shifting but a broadening of the spectral line. The second class of effects, *pressure broadening*, encompasses different phenomena, which all have in common that there must be atoms or ions in the vicinity of the emitting atom.

One effect is the so-called *collision broadening*. This name refers to the deexcitation of excited states by collisions on a shorter timescale than the natural lifetime. Shortening the lifetime leads to a larger uncertainty in the energy of the emitted photon and thus, a broader spectral line. According to Griem [76], collisions only affect the spectral line shape, not the integrated intensity of the line if one neglects the wavelength dependence of the radiative processes and also the possibility of the collisions leading to non-radiative transitions. It is stated that this is usually admissible even in very dense plasmas.

Another effect is *Stark broadening*, a broadening which is due to the presence of an electric field. In plasmas, this electric field can be generated by nearby ions.

There is also an effect called *resonance broadening*, which can occur if the radiating atom or ion and the perturbing atom or ion are of the same type. In this case, an exchange of excitation energy between particles becomes possible.

In summary, there a numerous effects which could lead to a reduction of the fluorescence lifetime in the cluster. By analyzing the fluorescence linewidth for different cluster sizes and FEL intensities (see chapters 4.4 and 4.2), it will be possible to determine whether the cluster environment and the plasma environment, respectively, have an influence on the radiative lifetime.

2.6. Fundamentals of reflectivity in the XUV range

Working with XUV light offers challenges not found at optical wavelengths, as optics do not work as one is accustomed to: lenses do not let light pass, mirrors reflect almost no light if used at normal incidence, i.e. if the wave's **k**-vector stands perpendicular to the surface. To understand this behavior, it is necessary to take a closer look at the refractive index $n(\omega)$.

The refractive index is a representation of the way light is scattered from the bound electrons into the direction the light is moving. The interaction of the scattered waves with the incident wave is responsible for phenomena like refraction, change of phase velocity, reflection or absorption in media. This, of course, is true for every electromagnetic wave, regardless of its wavelength. What is special about the XUV, however, is that its wavelength is comparable to the size of an atom and that the photon energies are close to electronic binding energies.

Evaluating how this sets apart the XUV from visible light requires some calculations. By applying a semi-classical model, in which a total number of Z electrons is treated as oscillators with resonant frequencies ω_s driven by the electric field of the incident wave, one arrives at the following general expression for the index of refraction. The derivations replicated in this section can be found in the book by Attwood [1]:

$$n(\omega) \equiv \left[1 - \frac{e^2 n_a}{\epsilon_0 m_e} \sum_s \frac{g_s}{(\omega^2 - \omega_s^2) + i\gamma\omega}\right]^{1/2} \tag{2.37}$$

Here e is the electron charge, m_e is its mass, ϵ_0 is the vacuum permittivity, n_a is the number density, i.e. the number of atoms per unit volume, i is the imaginary unit, γ, not to be confused with the Keldysh parameter, is a dissipative factor accounting for energy loss, g_s represents the assumed oscillator strengths of the electrons, which satisfy the following restriction:

$$\sum_s g_s = Z \tag{2.38}$$

The index s specifies each electron, their total number is s.
Finally, ω is the frequency of the incident wave and one can show that for XUV radiation it is much larger than $\sqrt{\frac{e^2 n_a}{\epsilon_0 m}}$:
A common glass, for example, is fused silica, $\mathrm{SiO_2}$, with a density ρ of approximately 2200 kg/m^3. The atomic masses of Si and O are 28 u and 16 u, respectively. Thus, n_a is

$$n_a = \frac{\rho}{m_{\mathrm{Si}} + 2m_{\mathrm{O}}} \approx 2.2 \cdot 10^{28} \text{ atoms/m}^3. \tag{2.39}$$

Therefore,

$$\sqrt{\frac{e^2 n_a}{\epsilon_0 m}} \approx 8.5 \cdot 10^{15}\,\mathrm{s}^{-1}. \tag{2.40}$$

Choosing 40 nm as the highest XUV wavelength, ω is at least

$$\omega = 2\pi \frac{c}{40\,\mathrm{nm}} = 4.7 \cdot 10^{16}\,\mathrm{s}^{-1}. \tag{2.41}$$

Therefore, one can approximate equation 2.37 by

$$n(\omega) = 1 - \frac{1}{2}\frac{e^2 n_a}{\epsilon_0 m} \sum_s \frac{g_s}{(\omega^2 - \omega_s^2) + i\gamma\omega}. \tag{2.42}$$

This equation can be rewritten as

$$n(\omega) = 1 - \frac{n_a r_e \lambda^2}{2\pi}[f_1^0(\omega) - i f_2^0(\omega)], \tag{2.43}$$

where r_e is the classical electron radius

$$r_e = \frac{e^2}{4\pi\epsilon_0 m c^2}, \tag{2.44}$$

and f_1^0 and f_2^0 are the components of the complex atomic scattering factor $f^0(\omega)$

$$f^0(\omega) = f_1^0(\omega) - i f_2^0(\omega) = \sum_s \frac{g_s \omega^2}{\omega^2 - \omega_s^2 + i\gamma\omega}. \tag{2.45}$$

The superscript ^{0} denotes the forward direction. Values for f can be found in tabulated form, for instance in [78].
Equation 2.43 is usually displayed in the following form:

$$n(\omega) = 1 - \delta + i\beta. \tag{2.46}$$

Comparison with equation 2.43 yields

$$\delta = \frac{n_a r_e \lambda^2}{2\pi} f_1^0(\omega) \tag{2.47}$$

and

$$\beta = \frac{n_a r_e \lambda^2}{2\pi} f_2^0(\omega). \tag{2.48}$$

Comparing δ and β for common materials in the XUV region shows that both are positive numbers of the order of 10^{-1} to 10^{-3}; the real part of the refractive index is slightly smaller than 1 for XUV radiation.

This has extensive consequences for the behavior of optics. The phase velocity v_φ is given by

$$v_\varphi = \frac{\omega}{k} = \frac{c}{n(\omega)}. \tag{2.49}$$

Therefore, if we consider a plane wave of the form

$$\mathbf{E}(\mathbf{r}, t) = \mathbf{E}_0 e^{-i(\omega - \mathbf{k} \cdot \mathbf{r})} \tag{2.50}$$

and insert equation 2.49 for k, we obtain the following:

$$\mathbf{E}(\mathbf{r}, t) = \underbrace{\mathbf{E}_0 e^{-i\omega(t - r/c)}}_{\text{vacuum propagation}} \underbrace{e^{-i(2\pi\delta/\lambda)r}}_{\text{phase shift}} \underbrace{e^{-(2\pi\beta/\lambda)r}}_{\text{absorption}} \tag{2.51}$$

The real part of the refractive index is responsible for a phase shift, the imaginary part causes absorption.
Some further calculations make it possible to determine the attenuation of the original intensity I_0 as

$$I = I_0 e^{-(4\pi\beta/\lambda)r}. \tag{2.52}$$

Therefore, we can define the exponential decay length l_{abs} as the distance after which the intensity has dropped to I_0/e:

$$l_{\text{abs}} = \frac{\lambda}{4\pi\beta}. \tag{2.53}$$

A comparison of decay lengths between visible light and XUV in air would be interesting but is impeded by the fact that it is difficult to find tabulated values for β for visible light. However, it is obvious that visible light is not absorbed significantly in air, even for distances of many kilometers like the earth's atmosphere, or else it would not be visible. On the other hand, for XUV radiation, values for β are easily available. For air and a wavelength of 40 nm, one can calculate l_{abs} to be on the order of several tens of micrometers.

It is obvious by this estimate that vacuum is absolutely necessary to experiment with XUV radiation. Reducing the pressure decreases n_a, which in turn makes β smaller, thereby enlarging l_{abs}.

But the transition into vacuum does not solve all problems. Lenses, for instance, can impossibly work for two reasons: first, because the index of refraction is so close to unity that almost no refraction is generated. Second, because radiation which enters optical elements will still undergo strong absorption. Even the reflection from mirrors, which also is an effect caused by the superposition of waves scattered from the atoms in the mirror, is drastically reduced. However, there is a way to achieve acceptable reflectivity, which becomes clear after a few calculations. By obeying the boundary conditions inflicted by Maxwell's equations, it is possible to derive *Snell's law*, here for the case of a vacuum, where $n_V = 1$ (see, for instance, Attwood [1]):

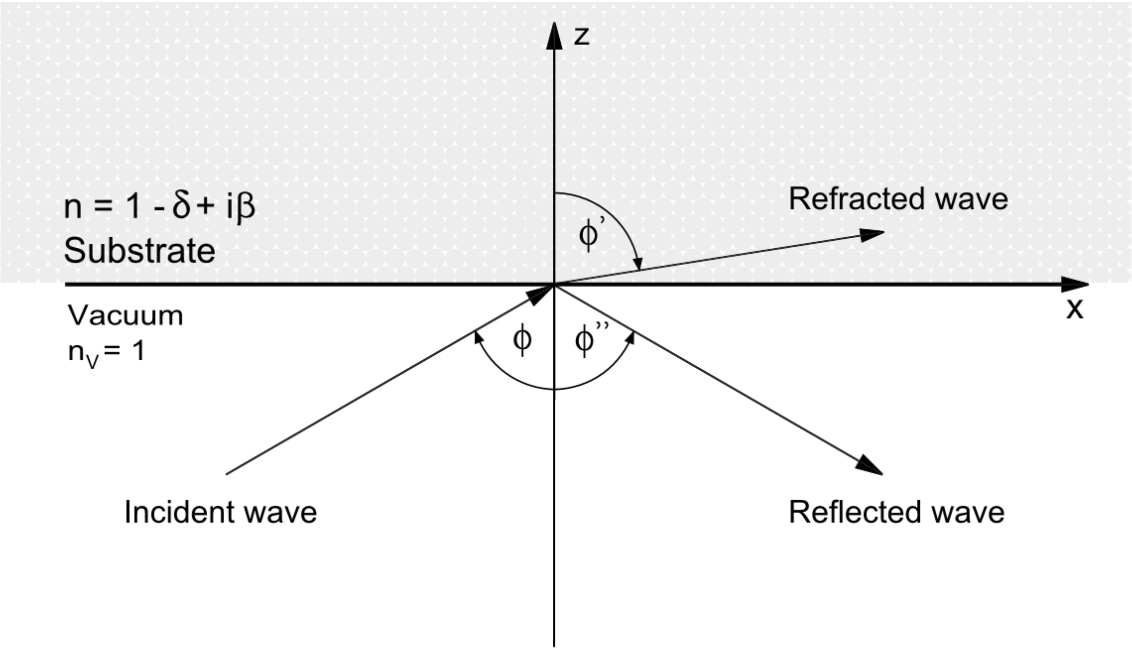

Figure 2.9.: An XUV light wave falls onto a substrate. A reflected and a refracted part are created. The part entering the substrate is refracted *away* from the surface normal, because n is slightly smaller than 1. (Adapted from [1])

$$\sin\phi' = \frac{\sin\phi}{n}. \tag{2.54}$$

The names of the angles can be found in figure 2.9. Even though this formula seems simple, it is valid for XUV radiation. One has to bear in mind, though, that n is complex and therefore, if ϕ is real, $\sin\phi'$ has to be complex, too.

But even if we consider n to be real and of the form $n \approx 1 - \delta$, Snell's law can be used to qualitatively understand a phenomenon which is very important for the manipulation of XUV radiation: *total external reflection*.

It is evident from Snell's law that XUV light entering the substrate will be refracted away from the surface normal, because n is slightly smaller than 1. If ϕ is enlarged, ϕ' at some point becomes 90°: the refracted wave cannot enter the surface. Therefore, all the light is reflected. The critical angle ϕ_c, at which total reflection occurs, is easy to calculate. For $\phi = \phi_c$, ϕ' is 90° and $\sin \phi'$ is 1. Therefore, we have

$$1 = \frac{\sin \phi_c}{n} = \frac{\sin \phi_c}{1 - \delta}. \tag{2.55}$$

Since n is only slightly smaller than 1, total external reflection only occurs for large angles. For this reason, angles in X-ray optics are usually defined not from the surface normal but from the surface. Introducing the complimentary angle θ

$$\theta + \phi = 90^\circ, \tag{2.56}$$

one obtains

$$\sin(90^\circ - \theta_c) = \cos(\theta_c) = 1 - \delta. \tag{2.57}$$

This expression can be rewritten in the following way:

$$\cos^2(\theta_c) = 1 - \sin^2(\theta_c) = (1 - \delta)^2 = 1 - 2\delta + \delta^2 \approx 1 - 2\delta. \tag{2.58}$$

Finally, this yields the critical angle θ_c:

$$\sin \theta_c = \sqrt{2\delta}. \tag{2.59}$$

It must be stressed that this calculation is not exact: terms higher than first order are neglected and absorption cannot be explained, because β is ignored from the start. Nevertheless, it illustrates an important point:
At XUV wavelengths mirrors have to be used at grazing incidence to achieve a significant reflectivity. For gold at 100 eV, for example, δ is $8.55 \cdot 10^{-2}$, yielding a critical angle of $\theta_c \approx 24^\circ$. As long as only flat mirrors are used, the use of grazing incidence solves most problems. If, however, light needs to be focused, the necessary use of grazing incidence generates a new problem, which will be explained in the next section.

2.6.1. Spherical mirrors at grazing incidence

All focusing optics suffer to some degree from aberrations. If a spherical mirror is used at grazing incidence, a well-known aberration, the astigmatism, becomes very pronounced. The effect of astigmatism is as follows. The focal length in the meridional plane differs strongly from the one in the sagittal plane. The meridional plane is the plane containing the chief ray of the ray bundle under examination and the optical axis of the mirror. The sagittal plane is perpendicular to the meridional plane and also contains the chief ray but not the optical axis. Figures 2.10 and 2.11 illustrate this convention. The focal length f_m in the meridional plane is given by

$$f_m = \frac{1}{2} R \sin\alpha, \tag{2.60}$$

where R is the radius of curvature of the mirror and α is the angle of incidence, measured from the mirror surface.

In contrast, the focal length f_s in the sagittal plane is given by

$$f_s = \frac{1}{2} \frac{R}{\sin\alpha}. \tag{2.61}$$

Both these formulas can be found in the paper by Kirkpatrick and Baez [79].

Therefore, for an angle of incidence of 10°, a common value when working with XUV radiation, f_s is roughly 33 times larger than f_m.

There is no easy way to remedy this problem; astigmatism is a natural consequence of grazing incidence on a spherical mirror. One possibility is the use of toroidal mirrors, which have a different radius in the meridional plane than in the sagittal plane. It is more difficult, though, and therefore more expensive, to produce such mirrors with the same optical quality as spherical mirrors. However, contrary to what has been said before, there are also special mirrors which can reflect XUV radiation even at normal incidence. They are discussed separately in the next section, because their working principle differs significantly from mirrors whose reflecting surface consists of a single material.

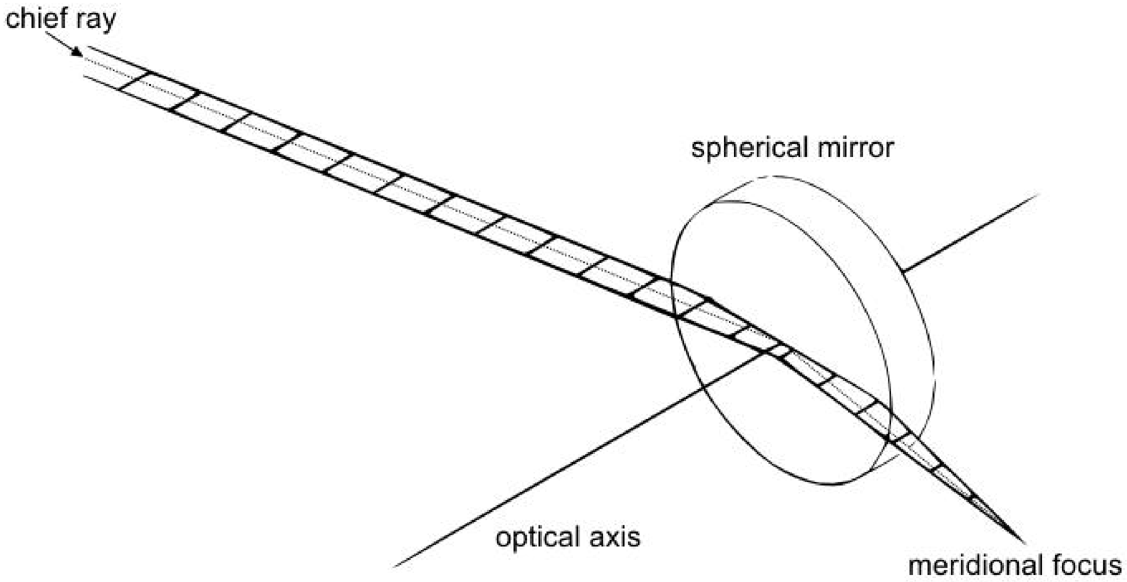

Figure 2.10.: Schematic drawing of the focal length of rays which lie in the meridional plane.

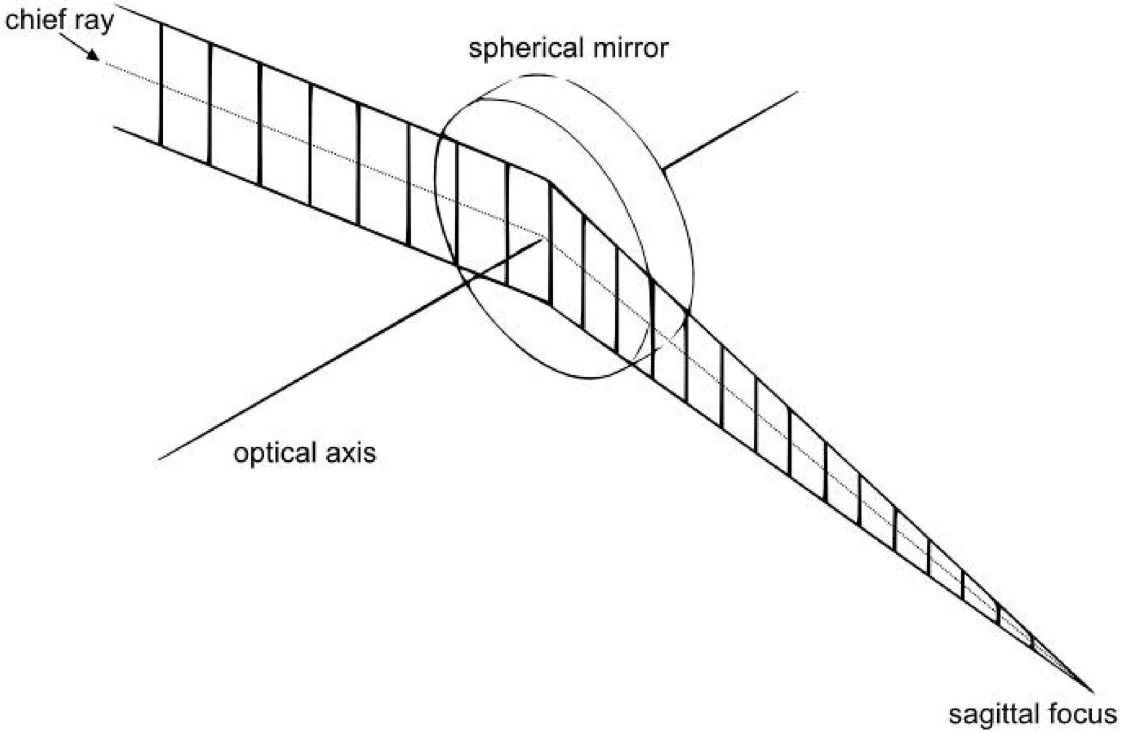

Figure 2.11.: Schematic drawing of the focal length of rays which lie in the sagittal plane. The sagittal focus lies significantly farther away from the mirror than the meridional focus.

2.6.2. Multilayer mirrors

So-called *multilayer mirrors* circumvent the restrictions inflicted by the refractive index and provide relatively high reflectivity for XUV wavelengths, even at normal incidence. Normal incidence reflectivities of almost 70 % have been achieved (Skulina et al. [80]). To achieve this, they are coated with an interference coating made up of alternating layers of two materials with different refractive indices. At each transition from one material to another the radiation is scattered. For normal incidence, the layer thicknesses are chosen in such a way that those parts of the incoming wave which are scattered back towards the direction of incidence interfere constructively. The information presented in this chapter about multilayer mirrors can be found in [1]. Employing Bragg's law

$$m\lambda = 2d\sin\theta, \tag{2.62}$$

one sees that to achieve this, each layer pair must have a thickness of $d = \lambda/2$. Here, m is the diffraction order, θ is the angle of incidence, measured from the scattering surface and d is the distance of the scattering sources. The layer thicknesses can be adapted if an angle of incidence other than perpendicular to the surface is required.

An alert look at equation 2.62 also reveals an inherent feature of multilayer mirrors, which, depending on the application, can either be a flaw or an asset: the condition $d = \lambda/2$ is only exactly satisfied for one wavelength. Therefore, a typical reflection curve looks like the one shown in figure 2.12. A multilayer mirror will always act as a bandpass, only reflecting a narrow wavelength range. Another fact, which can be derived from equation 2.62, is that

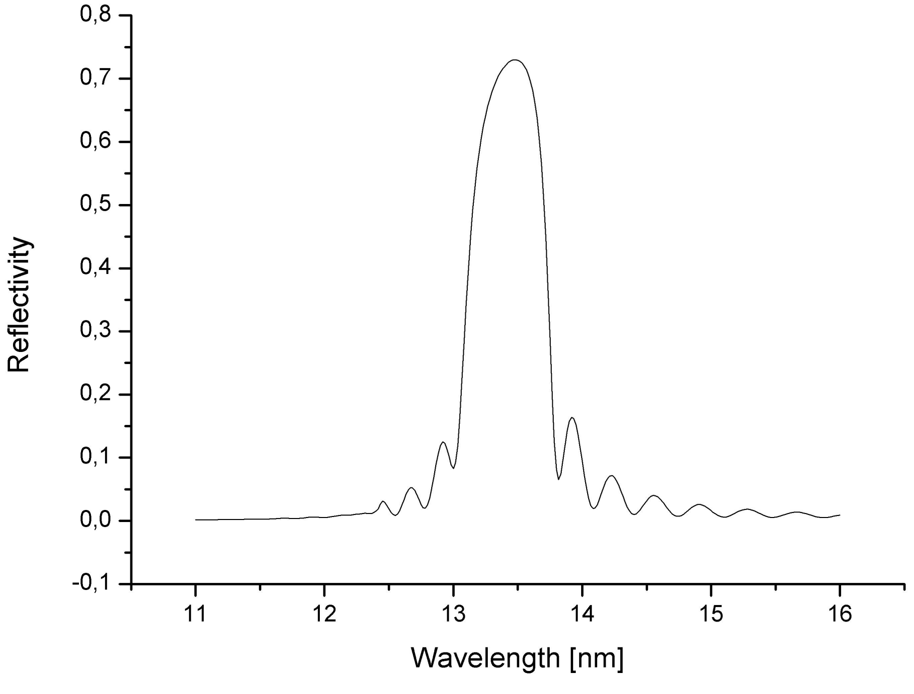

Figure 2.12.: An ideal reflection curve for a multilayer mirror. This is a calculated example from [81] for a mirror coating made of 40 alternating layers of silicon on top of molybdenum with a period of 6.9 nm. The Mo layers are 2.76 nm thick. The layers are assumed to be perfect. The incident light is s-polarized.

the manufacturing of multilayer mirrors becomes increasingly difficult with shorter wavelengths, because the higher the photon energies are, the smaller the layer thicknesses have to be. At high XUV energies, even imperfections on the scale of one atom monolayer have a significant effect.

Comparing the properties of multilayer and metal-coated mirrors, it is evident that multilayer mirrors are not superior to metal mirrors; they are merely different and choosing one or the other type depends on what one wants to achieve. The bandpass function of multilayer mirrors can be very useful and their ability to reflect XUV light at normal incidence allows for much smaller mirrors or for focusing a beam without astigmatism. If one wants to reflect a broad wavelength range, however, metal mirrors at grazing incidence are better suited.

After this entire chapter, we have the means to describe the how and why of the experiment in more detail.

As was shown in chapter 2.4, after irradiation with intense laser light, clusters exhibit complex ionization dynamics, which depend on many factors, including the wavelength of the radiation and its intensity. In the case of the experiments presented in this thesis, the radiation is supplied by FLASH (see chapter 2.2). Chapter 2.4.5 showed that there are indirect indications that the charge states which are detected in ion time-of-flight spectrometers, microseconds after the interaction of light and cluster, are not as high as those initially created. This is a limitation which is inherent to time-of-flight detectors. Consequently, it is still an open question what charge states are initially created in the cluster center. Therefore, in this thesis, we took an alternative approach. By concentrating on fluorescence emanating from the interaction region, we have a chance of observing a prompt signal of the initially created charge states. The influence of cluster and plasma effects could lead to a broadening and/or shifting of spectral lines. Lastly, the previous section introduced the technical challenges one faces in the work with XUV radiation. This knowledge will be put to use in the next chapter, which details the design and construction of the XUV fluorescence spectrometer and its implementation into an existing vacuum chamber.

3. Experimental setup

Our experiments can be described in just a few sentences: FEL radiation is focused into a target of rare gas clusters. The ionized clusters emit fluorescence radiation, which is analyzed by a fluorescence spectrometer. The FEL cluster interaction is studied as function of FEL intensity, cluster size and cluster composition.

The experiments took place at Beamline 2 (BL2) of FLASH. They were carried out in a so-called *tandem geometry*. The setup is shown in figure 3.1. One experiment, which is not the topic of this thesis, used the BL2 focus. The experiments described in this thesis, measuring XUV fluorescence of clusters, took place in a second chamber behind the first. A second focus was generated in the second chamber by refocusing the FEL beam with a multilayer mirror. The tandem setup allowed for an efficient use of the FLASH beamtime. The first experiment did not affect the second one very much. Its aim was to scatter light from single clusters. Such a dilute sample does not weaken the FLASH beam significantly, therefore operating the cluster fluorescence experiment behind it is unproblematic.

Figure 3.2 shows a schematic drawing of the experimental setup. In the drawing, the FEL beam passes through the chamber and is reflected from a multilayer mirror with a focal length of 450 mm. The angle of incidence is almost 90°(with respect to the mirror surface) so that the focus of the FEL beam is almost in the middle of the experimental chamber, just slightly to the right (with respect to the direction of travel of the light) and slightly upwards. Before hitting the multilayer mirror, the incoming beam is shielded within a metal tube so that it cannot cause any unwanted effects, namely scattered light and the premature ionization of clusters by the unfocused beam. The mirror is slightly tilted so that the focused beam lies outside of the metal tube.

The cluster beam intersects with the FEL beam at an angle of almost 90°. The nozzle of the cluster source has a diameter of 100 µm and a half opening angle δ of 15°. According to equation 2.2, this results in an equivalent nozzle diameter of 276 µm.

The spectrometer is mounted on top of the chamber, and therefore almost perpendicular to both the FEL beam and the cluster beam. Strictly speaking, the spectrometer defines the interaction point, since it cannot be moved with respect to the chamber. Thus, the FEL beam and cluster beam have to be overlapped in the focal point of the grating to ensure the imaging of the interaction point with the highest possible resolution. The design of the grating requires an entrance slit, but, as the refocusing mirror allows very fine focusing, it is possible to image the interaction region directly, without the need for an entrance slit.

While the spectrometer is fixed in space, both the cluster source and the focusing mirror can be adjusted. The cluster source is mounted on an xyz-manipulator, thereby ensuring that the source can be brought to the correct height and horizontal position, and also as close as possible to the FEL beam. This is very important because the density of clusters in the beam drops quadratically with increasing distance from the source, decreasing the fluorescence yield significantly.

The mirror mount can be tilted and moved perpendicular to the FEL beam. These adjustments make it possible to generate the desired beam path from the mirror through the interaction region and onto the beam dump. But there is another degree of freedom: the mirror can be moved along the beam path, thereby shifting the focus of the FEL beam along the beam path without altering the beam path. This equates to a variation of the FEL intensity within the

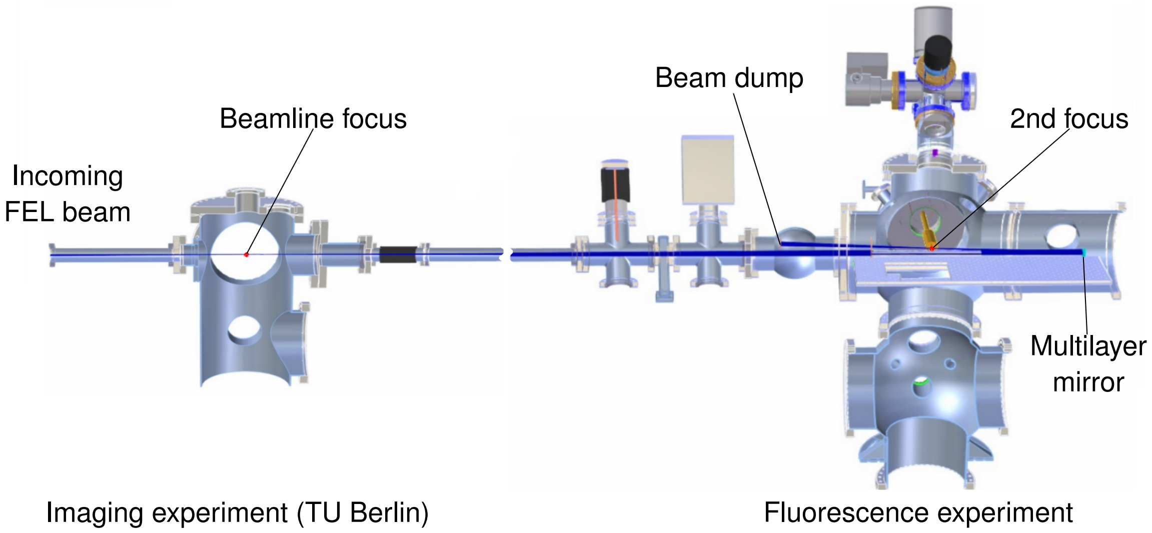

Figure 3.1.: Schematic overview of the entire experimental setup. The chamber used for the experiments presented in this thesis was located behind a primary chamber, which used the direct BL2 focus. (Picture courtesy of Maria Müller [82])

interaction region. The FEL intensity in the interaction region is an important quantity for the characterization of the interaction of rare gas clusters and XUV light. The higher the intensity, the more photons can be absorbed by the clusters in a given amount of time. The more photons are absorbed, the higher the resulting charge states can become. By recording a so-called *intensity scan*, that is recording successive spectra at different positions of the refocusing mirror and therefore different peak intensities in the interaction region, we can observe how the relative strength of individual spectral lines depends on the FEL intensity. Different dependencies of spectral lines help in assigning them to different charge states. Ultimately, the analysis of the evolution of the fluorescence in dependence on FEL intensity provides information on the energy deposition and redistribution processes.

Another option to change the power density at FLASH in a controlled way is to vary the available photon flux using the gas attenuator, but doing so would have affected the cluster imaging experiment performed by the TU Berlin, since the gas attenuator is located further upstream in the beam line.

Of course, an intensity scan is only useful if the absolute intensity and, even more important, the relative change in intensity are known. These values are calculated in the following.

First, it is important to realize that the incident beam is not collimated but divergent because there already is a focus in the first experimental chamber. This first focus is located 4050 mm in front of our multilayer mirror. If the size of the first focus and the focal length of the multilayer mirror are known, the size of the focus in our chamber can be calculated in the following way. From geometrical optics it is known (see for instance the book by Hecht [83]) that the image distance s_i depends on the object distance s_0 and the focal length f:

$$\frac{1}{f} - \frac{1}{s_0} = \frac{1}{s_i} \tag{3.1}$$

In our case, f is 450 mm and s_0 is 4050 mm as was mentioned before. Therefore, s_i is

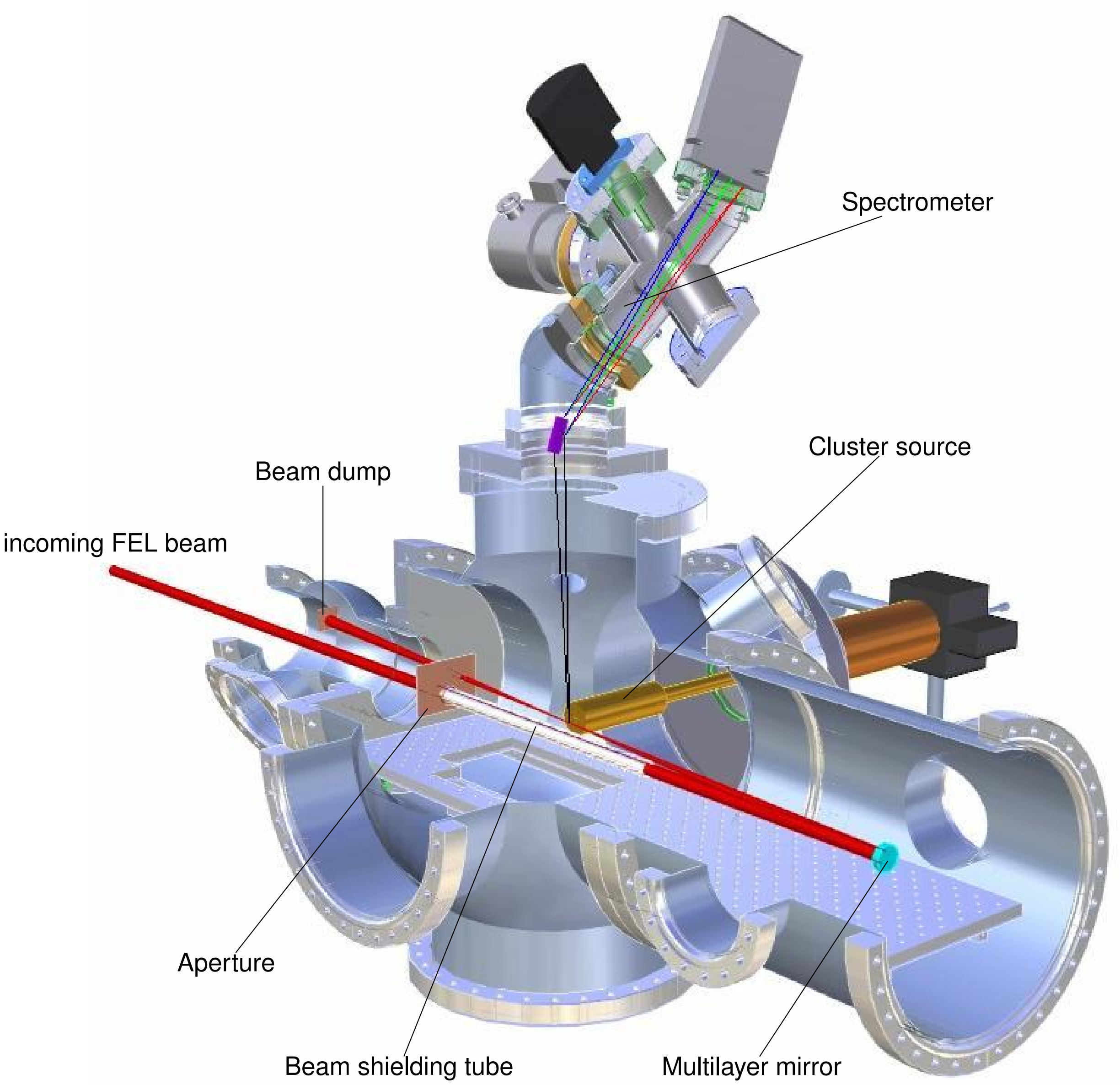

Figure 3.2.: Detailed view of the experimental setup. The divergent FLASH beam enters the chamber and passes through a tube (ensuring that it cannot ionize clusters). The beam is refocused with a movable multilayer mirror. The spectrometer focus defines the interaction point. Both the cluster beam and the FEL beam intersect in this point. (Picture courtesy of Maria Müller [82])

506.25 mm.
The magnification M_T is given by:

$$M_T = \frac{s_i}{s_0} = \frac{506.25 \text{ mm}}{4050 \text{ mm}} = 0.125 \tag{3.2}$$

This means that the focus in the second chamber is 8 times smaller than the focus in the first chamber. With the literature value for the focus at the BL2 beam line at FLASH, denoted by the subscript $_{\text{foc1}}$, being 20 µm (FWHM) ([39]), this amounts to a focus diameter in the cluster fluorescence experiment of about 2.5 µm (FWHM), denoted by the subscript $_{\text{exp}}$.
The focal dimension enables us to calculate the relative change in intensity as the focal point is moved away from the interaction region.
The intensity I in a Gaussian beam is given by:

$$I(r,z) = I_0 \frac{1}{1+(\frac{z\lambda}{\pi w_o^2})^2} e^{-\frac{2r^2}{w^2(z)}} \tag{3.3}$$

In this formula, z is the variable describing the beam direction and r is perpendicular to z. Since we are interested in the maximum intensity in the beam depending on z, which is obviously reached at $r = 0$, we can drop the exponential term and arrive at

$$I(r,z) = I_0 \frac{1}{1+(\frac{z\lambda}{\pi w_o^2})^2}, \tag{3.4}$$

where I_0 is the intensity at $z = 0$, where the beam diameter is smallest. $w(z)$ gives the point where the radial intensity has dropped to I_0/e^2 from the maximum value I_0. The beam waist w_0 is defined as $w(z)$ at the focal spot. Assuming a Gaussian beam profile, a spot size of 20 µm FWHM, corresponds to $w_{0,\text{foc1}} \approx 17$ µm. With the demagnification M_T calculated above, the waist size $w_{0,\text{exp}}$ in our experiment is approximately 2 µm.
The maximum amount the mirror was moved, was 15 mm. This corresponds to a reduction of intensity by a factor of 0.0012.
Apart from knowing the relative change in intensity, it is also important to know the absolute pulse intensity to allow comparisons with previous and future experiments. For short-wavelength SASE FELs, this is difficult to determine, for the following reason. Intensity is given by energy per area and time. The energy in the pulse is routinely measured pulse-to-pulse making use of gas monitor detectors (GMDs, see Tiedtke et al. [39, 84]). These detectors work in the following way: the FEL beam passes through a chamber filled with a rare gas. The gas pressure in the chamber is low, at about 10^{-6} mbar, so that any alteration of the FEL beam parameters is negligibly small. The FEL beam passing through the rare gas ionizes some atoms. Ions and electrons are accelerated onto separate eletrodes by an electric field. By measuring the resulting current, the FEL pulse energy can be determined with an accuracy of 10% [39].
The area is easily calculated from w_0, which has just been estimated. The problematic variable is the time. While it is known that the pulses produced by FLASH are 'very short' it requires an experiment on its own to determine the actual pulse length (see, for example, Frühling et al. [35], Mitzner et al. [85]). From a compilation of different pulse length measurements, it is however known that the pulse lengths is proportional to the bunch charge. During our experiments, the bunch charge varied between 0.42 and 0.49 nC. For these values, pulse lengths between 100 and 200 fs have been measured[1]. Therefore, the FEL intensity is calculated using

---

[1] Dr. Stefan Düsterer, private communication.

a pulse duration of $t_{\mathrm{pulse}} = 150$ fs ± 50 fs. The pulse energy varied during the measurements, of course. During some scans, the average pulse energy reached $E_{\max} = 150$ µJ.
According to Tiedtke et al. [39], the overall transmission T_{BL2} of BL2 is $(64 \pm 4)\%$. This value covers all losses up to the beamline focus (which in our case is located in the first experimental chamber of the tandem setup). Two components in our setup further reduce the intensity. An aperture clips the outer parts of the beam to ensure that the remaining beam passes through the beam shielding tube without generating stray light. According to simulations by M. Müller [82], 95.5% of the intensity pass through the tube. Finally, the multilayer mirror with a reflectivity of $R_{\mathrm{ML}} = 0.65$ plays a significant role.
With a focus area of $A = \pi(2.12\,\mu\mathrm{m})^2$, we arrive at

$$I_0 = \frac{E_{\max}}{t_{\mathrm{pulse}} \cdot A} \cdot T_{\mathrm{BL2}} \cdot R_{\mathrm{ML}} \cdot 0.955 = 3 \cdot 10^{15}\,\mathrm{W/cm^2} \pm 1 \cdot 10^{15}\,\mathrm{W/cm^2}. \qquad (3.5)$$

The error was calculated by Gaussian error propagation from the known errors. For some of the parameters, the cited works do not give an error. However, this is of minor importance, because the overall error is heavily dominated by the estimated error of the pulse length, which is the largest relative error by far.
Therefore, at a beam energy of 150 µJ we could vary the intensity in the interaction region from $3 \cdot 10^{15}\,\mathrm{W/cm^2}$ to $4 \cdot 10^{12}\,\mathrm{W/cm^2}$. These values have to be scaled according to the GMD data for the beam energy recorded during the experiments.

3.1. Fluorescence spectrometer

The fluorescence spectrometer consists of two essential elements: a reflective diffraction grating and an XUV-sensitive CCD-camera. A third element, which offers additional functionality, is a filter wheel with which thin metal foils can be introduced into the fluorescence beam path to attenuate certain wavelengths. All the other parts of the spectrometer only serve the purpose of aligning these elements correctly with respect to each other and to move them in a defined manner. Figure 3.3(b) shows a cross section through the spectrometer. The important elements have been highlighted. The central requirement for the spectrometer was the ability to discern spectral features from the VUV to the XUV spectral range, where xenon exhibits characteristic fluorescence from charge states between 1+ and 10+. Furthermore, as was shown in section 2.5, the expected fluorescence yield is low, making a high transmission efficiency a critical requirement of the spectrometer. As was shown in section 2.6, each optical element severely reduces the number of transmitted photons in the XUV wavelength range. Choosing a commercial grating from Horiba Jobin-Yvon (imaging range 10 to 110 nm, catalog number 541 00 200) enabled us to use only a single optical element. The spectrometer was designed accordingly.
The grating was recorded holographically on a toroidal substrate and has a variable line spacing (VLS) with an average of 450 lines/mm. The toroidal form allows focusing both in the meridional as well as in the sagittal plane. But the foci of a purely toroidal grating along the dispersion direction fall on the so-called Rowland circle (see, for instance, [86]), i.e. not on a plane but on a curved surface. The varying line spacing slightly alters the focusing properties of the grating, so that all the foci lie in a plane (see, for instance, [86]).
These are obviously very desirable properties as they enhance both the amount of light which falls onto the detector and the resolution on a plane detector. However, these improvements come at the price of having to mount the grating in the exact way for which it was designed, otherwise the spectral lines will not be focused on the detector plane. Figure 3.4 shows the

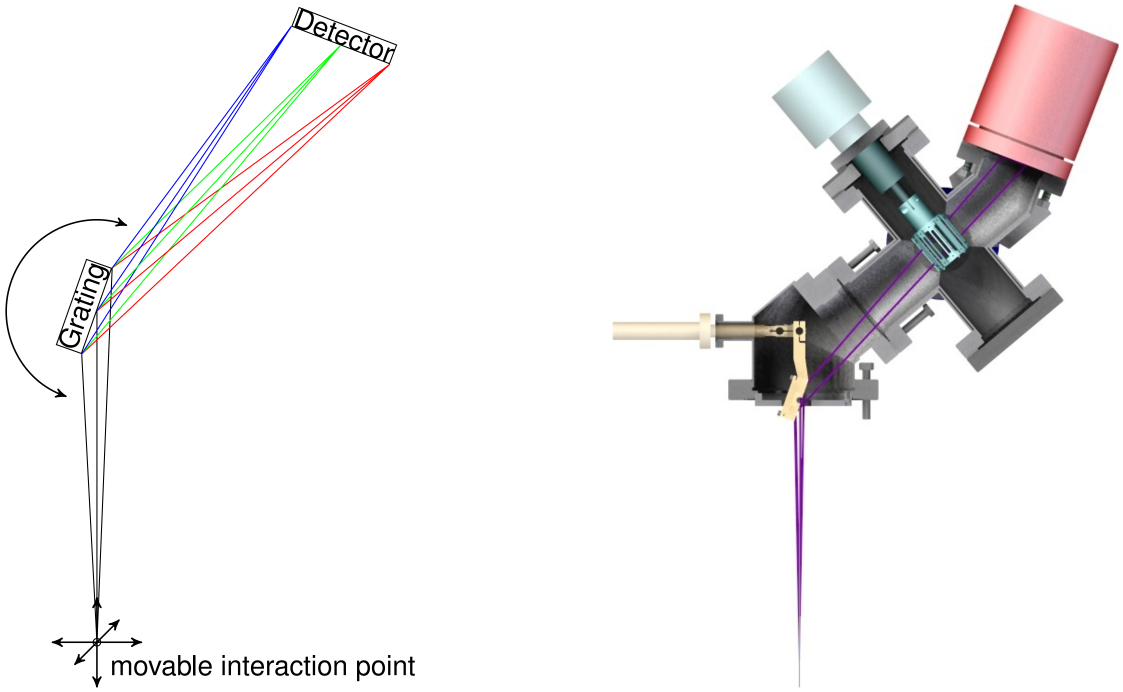

Figure 3.3.: Schematic drawing of the spectrometer design, in comparison to the rendered drawing of the constructed version on the right. In the cross-sectional view of the spectrometer, the grating tilter is highlighted in orange, the filter wheel in turquoise, the detector in red.

layout of a spectrometer using the grating as intended by the manufacturer. These values are the basis of the design shown in figure 3.3(b). Table 3.1 lists the most important parameters of the grating.

Wavelength range	10 - 110 nm
Length of spectrum on detector	40 mm
Distance from entrance slit D_S	292.05 mm
Angle of incidence α (to surface)	19.435°
Average number of grooves/mm	450
Grating dimensions (L×W×H)	$34 \times 12 \times 10\,\mathrm{mm}^3$
Ruled area	$30 \times 8\,\mathrm{mm}^2$
Coating	Gold

Table 3.1.: Parameters of the diffraction grating measured by the manufacturer

3.1.1. Design and technical construction

The construction of the spectrometer was guided by two constraints. As was mentioned above, the diffraction grating defined all angles and distances between the source, itself and the detector. The second constraint was the experimental chamber, which already existed during the planning stages for the spectrometer. The distance of the interaction point within the chamber to the flange was essentially fixed. This distance was close to the design distance between the source and the grating.

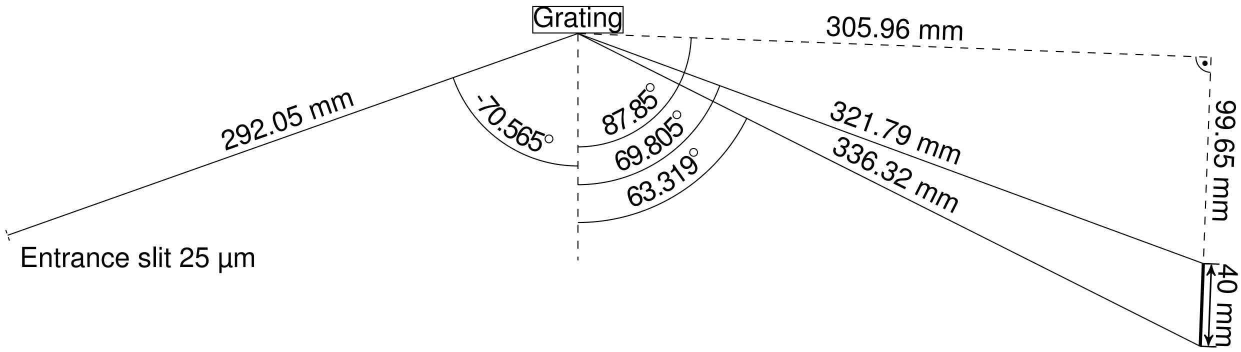

Figure 3.4.: Angles and distances for which the grating was designed.

Making the spectrometer a multi-purpose device, usable also in very different setups, would have required adding a manipulator to its base to be able to move it with respect to a possible fixed interaction point. In the current setup, such a manipulator is not needed, because both the FEL beam and the cluster source are fully adjustable, as was explained above. Nevertheless, for future experiments, a very compact manipulator was already designed (see chapter A.2). The basic design of the spectrometer, i.e. methods of translation of the components, travel ranges of the components, incorporation of metal filters, placement of flanges, was done by me. The technical implementation and detailed construction work was done by Angad Swiderski, an engineer from the group FS-FL.

The diffraction grating is mounted in a cradle, which can be tilted around an axis passing through the middle of the grating surface, parallel to the grooves. This tilting allows us to not only dial in the nominally correct position, but also to observe the zeroth order of the grating, which is useful for finding a signal and for calibration. Additionally, it is also possible to tilt the grating in the other direction to see the wavelength range up to 110 nm. These wavelengths will not be imaged as sharply as the ones in the correct position due to the incorrect angle of incidence, but this possibility of adjustment was incorporated because the chosen detector (see chapter 3.1.2) only offers a width of 27.6 mm, where 40 mm would be required to measure the entire design wavelength range of the grating as can be seen in figure 3.4.

The tilting of the grating is accomplished in the following way: the cradle is mounted so that it can swing around the axis mentioned above. Special springs are used on the axle to create a pretension. The cradle is moved by a small manipulator operated by a micrometer screw (Trinos 420MZF016-010). Again, the manipulator is coupled to the cradle with springs to keep the backlash at a minimum. By moving the micrometer screw inwards, towards smaller values, the angle of incidence with respect to the surface is increased.

The grating is held in the cradle only by its own weight to ensure that no stress is applied to the sensitive grating surface by clamping it in position. The grating nevertheless cannot fall out of the cradle because a plate is mounted 0.5 mm behind the backside of the grating. The grating is guaranteed to be in its designed position as long as the spectrometer is mounted with the grating surface facing downwards.

Table 3.2 summarizes the nominally correct angles and micrometer screw positions as determined from the technical drawings. The filter wheel, which is used to introduce thin metal foils into the beam path, is situated behind the diffraction grating and is adapted from a design developed during the Ph.D. thesis of Dr. Roland Fäustlin [87]. The filters were purchased mounted on aluminum frames from Lebow Company. The area where the metal foil is unsup-

Wavelength range	Angle	Mirometer screw position
Zeroth order	21.437°	2.605 mm
10 - 76 nm	19.435°	4.47 mm
up to 110 nm	18.3°	5.86 mm

Table 3.2.: Nominally correct angles and micrometer screw positions as determined from the technical drawings. Proper focusing of the light can only occur for 10 to 76 nm.

ported measures 28 mm× 3 mm. Two materials are used, aluminum (Al) and zirconium (Zr), each in thicknesses of 100 and 200 nm. Their transmission curves are shown in figure 3.5. As can be seen, Al efficiently absorbs the FLASH wavelength of 13.5 nm in our experiments, leaving wavelengths higher than 17 nm comparatively unaffected, while the transmission curve of Zr is, roughly speaking, the mirror image of the one of Al.

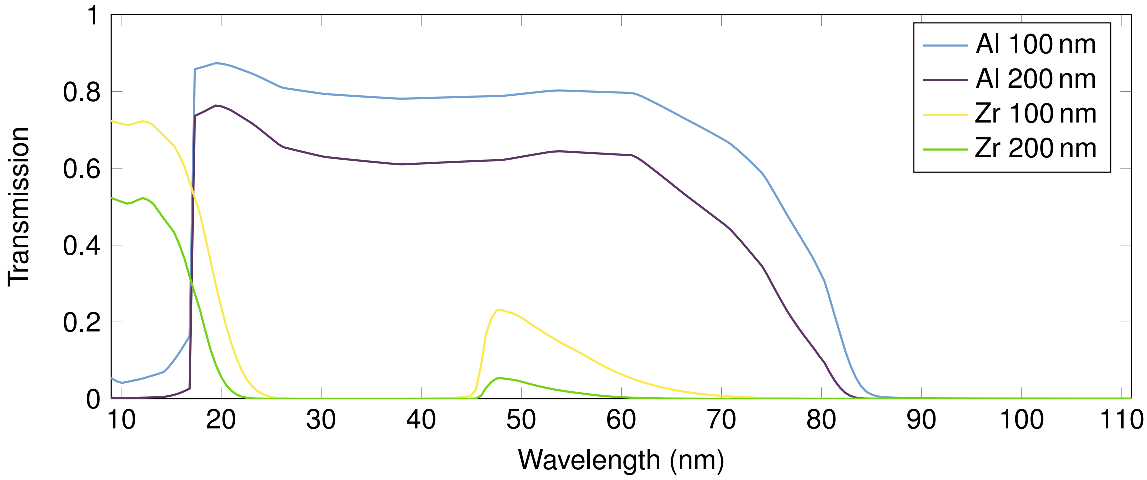

Figure 3.5.: Transmission curves for aluminum and zirconium for thicknesses of 100 and 200 nm.

The filters are arranged on the lateral surface of a cylindrical mount. This cylindrical mount can be turned around its center axis by a manual rotary feedthrough, moving either one of the four filters into the beam or a solid aluminum block to obstruct the beam. Of course, it is also possible not to introduce any filters into the beam path. Table 3.3 summarizes the positions of the filters on the scale of the rotary feedthrough. These positions are only correct for the current mounting orientation of the rotary feedthrough. If filters have to be replaced, care must be taken to mount the feedthrough in the same way as before.

Filter	Feedthrough position
Beam block	230.1°
Al, 100 nm	261.5°
Free beam path	292°
Al, 200 nm	323.5°
Zr, 100 nm	350.2°
Zr, 200 nm	22.1°

Table 3.3.: Positions of the rotary feedthrough used to introduce metal filters into the beam path.

3.1.2. Detector

The detector which is used in the spectrometer is a camera with a thermoelectrically cooled CCD-chip which is sensitive to photons roughly from 1000 nm to 0.15 nm. The camera is a PIXIS-XO: 2KB manufactured by Princeton Instruments. The reason that it, in contrast to a standard CCD-camera, is sensitive to XUV- and X-ray-radiation lies in the special treatment of the chip. A standard CCD-chip relies on the photoelectric effect to let photons create electron-hole-pairs. The produced charges are equivalent to the number of photons and since the chip is segmented into sections, or pixels, which are isolated from each other, an image can be reconstructed. This principle is still true for the camera used in our spectrometer, but it uses a so-called *back-thinned* CCD chip. In a standard chip, photons have to pass solid-state gate structures, which are necessary for the conduction of the produced charges, before they reach the light-sensitive portion of the chip. As we saw in chapter 2.6, however, XUV photons are highly likely to be absorbed in any kind of matter. Therefore, they do not reach the light-sensitive parts of a standard chip. A back-thinned chip is therefore turned around so that photons enter from the backside, without being obstructed by gate structures or anything else. The electron-hole-pairs still have to be produced near the gate structures, however. To make this possible, the chip is thinned to a thickness of only about 15 µm.

The PIXIS-XO: 2KB has a chip of 2048×512 pixels. Each pixel has a size of 13.5 µm $\times$ 13.5 µm. Consequently, the dimensions of the chip are 27.6 mm $\times$ 6.9 mm.

The width of the chip (27.6 mm) severely limits the spectral range which can be aquired in a single image. As was explained before, the grating is designed for a 40 mm wide detector. Due to the camera, the maximum observable wavelength is reduced from 110 nm to slightly more than 76 nm.

Alternatively, a multi-channel plate detector (MCP) could have been used. Wiza provides a good overview of these devices [88]. MCPs are essentially glass substrates which are perforated by closely spaced, tiny channels. They are coated with conductive coatings, which emit electrons via the photoelectric effect. A high voltage is applied along the channels. This voltage leads to the acceleration of electrons, always confined to their original channels. For each electron hitting the walls, several electrons are emitted. This leads to an amplification of the electrons by a factor of 10^4 to 10^7, depending on the number of MCPs in a stack. These electrons can then be used to excite a phosphor coating, which emits visible radiation. This radiation can easily be imaged.

Compared to a back-illuminated CCD camera, an MCP-based system has advantages and disadvantages. The most important advantage for our application is that MCPs with a diameter of 40 mm are commercially available. Therefore we would be able to reap the entire wavelength range the grating can properly focus. Another advantage is their 'solar blindness', i.e. their being insensitive to visible light. This property makes the avoidance of stray light on the spectra much easier.

However, MCPs also have severe disadvantages. From a purely practical standpoint, MCPs require much more effort to mount. The MCP has to be mounted in vacuum, while the camera system is typically outside. Both require custom-designed mounts. In addition to that, several high-voltage power supplies are needed for the MCPs and the phosphor screen. The PIXIS-XO: 2KB on the other hand is a single piece, which comes equipped with a vacuum flange. Another important point is the degree of vacuum needed to operate these detectors. MCPs may not be operated at pressures above $\approx 1 \cdot 10^{-6}$ mbar. The PIXIS-XO: 2KB works even at atmospheric pressure. One just has to remember not to use the cooling option of the chip at such high pressure, because gas atoms would condense on the chip.

The most important disadvantage for our experiment, though, is that the quantum efficiency of an MCP is significantly lower than that of a back-illuminated CCD. As we will see in the next section the quantum efficiency of our back-illuminated CCD varies between 15 and 45%.

In contrast, the quantum efficiency of an MCP is below 5% according to Carpenter et al. [89]. Additionally, even with a cleverly designed optical system to image the phophor screen about half of the emitted light will not reach the camera chip.

Considering the limited time in FLASH experiments and the very low fluorescence yield we expected in our experiments, we chose to sacrifice the larger wavelength range for a significant increase in quantum efficiency and therefore a significant increase in the chance to detect fluorescence.

3.1.3. Overall transmission

One important property for the characterization of the spectrometer is the number of photons which are detected compared to the number of photons which are emitted. This is given by the percentage of photons hitting the grating, multiplied by the efficiency of the grating and the quantum efficiency of the camera.

Fluorescence photons are emitted into all directions with equal probability[1]. Therefore, the percentage of photons hitting the grating T_{geom} can be estimated by comparing the grating area A_{proj} which the photons 'see' from the source point with the surface area A_{Sphere} of a sphere with a radius R_S equal to the distance from the source point to the grating. This is approximately given by:

$$T_{\mathrm{geom}} = \frac{A_{\mathrm{proj}}}{A_{\mathrm{Sphere}}} \approx \frac{\sin\alpha \cdot A_{\mathrm{grat}}}{4\pi R_S^2} \approx 7.5 \cdot 10^{-5} \tag{3.6}$$

A_{grat} is the surface area of the grating. Multiplied by $\sin\alpha$, where α is the angle of incidence 19.435°, this gives the projected area A_{proj}. To get the overall transmission, one has to multiply T_{geom} with the diffraction efficiency G_{eff} of the grating and the specified quantum efficiency C_{queff} of the camera. Curves for both values are shown in figure 3.6. According to the manufacturer, the real value for the grating efficiency is usually between 85 and 95% of the calculated value shown there. The reason for this discrepancy are manufacturing imperfections,

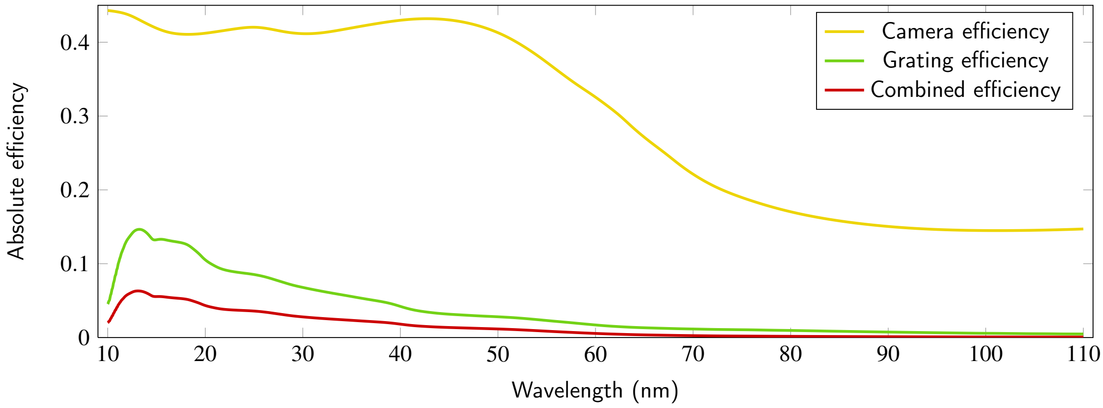

Figure 3.6.: The efficiency of the reflection grating for unpolarized light calculated by the manufacturer and the quantum efficiency of the detector.

---

[1] So-called *fluorescence anisotropy* can occur if transition moments for absorption and emission depend on the direction of the fluorophore (the fluorescing structure) with respect to the polarization of the exciting photon (see, for instance, the book by Lakowicz [90]). This can happen in molecules, for example. In a rare gas cluster, however, which is an isotropic system consisting of isotropic systems (the rare gas atoms) fluorescence is isotropic.

most importantly an imperfect surface roughness of the grating, which causes light to be scattered instead of refracted.
To get a worst case scenario, I will use the lowest relevant values, i.e. the values at 76 nm, because no spectra recorded at longer wavelengths (and therefore even lower efficiency) are used in this thesis. The overall transmission T amounts to

$$T = T_{\text{geom}} \cdot 0.85 \cdot G_{\text{eff}} \cdot C_{\text{queff}} = T_{\text{geom}} \cdot 0.85 \cdot 0.01 \cdot 0.18 = 1.1 \cdot 10^{-7} \tag{3.7}$$

Another way to put this is that of about 9 million emitted photons only one is detected. We note that in the data evaluation (chapter 4) the spectra are normalized with respect to the wavelength dependent spectrometer transmission T.

3.1.4. Wavelength scale

The toroidal shape and variable line spacing of the grating make for a powerful optical element. Unfortunately, the same properties also make for a grating which is very hard to simulate. In fact, the optical ray-tracing software ZEMAX is not equipped to handle diffraction gratings which are both toroidal and have a variable line spacing. Furthermore, the variation of the line spacing is not made public by the manufacturer. Therefore, I calculated the wavelength scale from the information provided. Values for the dispersion at different wavelengths and their respective positions on the detector given by the manufacturer are shown in table 3.4.

Wavelength (nm)	Dispersion (nm/mm)	Position on detector (mm)
10	2.3	0.04
35	2.4	10.75
60	2.5	20.85
85	2.6	(30.55)
110	2.7	(39.95)

Table 3.4.: Values for the dispersion and the position on the detector depending on the wavelength, as given by the manufacturer. Values in brackets are too large for the detector in use.

From a practical standpoint, the important information is which pixel of the camera corresponds to which wavelength. This wavelength scale can be calculated from the values in table 3.4. Naming the pixel number px and the dispersion D, we obtain[1]:

$$D = 2.3\,\text{nm/mm} + 0.00013(px - 1) \tag{3.8}$$

$$\lambda = 0.0325\,\text{nm/px}(px - 1) + 10\,\text{nm} \tag{3.9}$$

---

[1] Strictly speaking, the formula is not correct because it places 10 nm on the first pixel rather than on the third, as would be correct according to table 3.4. This inaccuracy, however, is not important since this theoretical wavelength scale has to be fitted to the experimental result later on anyway.

3.1.5. Expected resolution

The theoretical resolution of the spectrometer can be calculated from the dispersion given in table 3.4. Spectral lines can only be distinguished if their maxima do not fall on adjacent pixels, the maxima have to be separated by at least one pixel. Since the pixels have a width of 13.5 µm, this requirement corresponds to a separation of the lines of 27 µm. As can be seen in table 3.4, at 10 nm the dispersion is 2.3 nm/mm. Over 27 µm, this corresponds to a wavelength separation $\Delta\lambda$ of

$$\Delta\lambda = \frac{2.3\,\text{nm}}{1000\,\text{µm}} \cdot 27\,\text{µm} = 0.0621\,\text{nm} \tag{3.10}$$

The resulting resolution $\lambda/\Delta\lambda$ at 10 nm is

$$(\lambda/\Delta\lambda)_{@10\,\text{nm}} \approx 161. \tag{3.11}$$

The dispersion at 75 nm can be interpolated from the values in table 3.4 to be 2.56 nm/ mm. The rest of the calculation is analogous to the previous one and results in

$$(\lambda/\Delta\lambda)_{@75\,\text{nm}} \approx 1085. \tag{3.12}$$

These calculations only hold true if the resolution is not limited by the grating. The theoretical resolving power R_{grat} of a plane grating is (see the book by Loewen and Palmer [86]):

$$R_{\text{grat}} = \frac{\lambda}{\Delta\lambda_{\text{grat}}} = \frac{Nd(\sin\alpha + \sin -\beta)}{\lambda}, \tag{3.13}$$

where N is the number of illuminated grooves, d is the distance between grating lines and α and β are the angles of the incoming and outgoing light, respectively (for this formula defined with respect to the surface normal, as shown in figure 3.4). Of course, the grating used in the spectrometer is not flat and the line spacing is not constant, but using the average values from table 3.1 for an estimate of R_{grat}, the result is so much larger than the resolution calculated above that it is safe to say that the resolution of the spectrometer is limited by the pixel size of the camera: for $\lambda = 10\,\text{nm}$, R_{grat} is approximately 13500. For $\lambda = 75\,\text{nm}$, it is even a little bit larger, because the smaller β compensates for the larger wavelength.

4. Analysis of the experimental results

In our experiments we investigated the behavior of clusters consisting of xenon and argon, respectively, and also a mixture of both, which results in clusters with a xenon core and an argon shell. We wanted to determine how the variation of the FEL intensity and the variation of the average cluster size and compostion of clusters influence the resulting fluorescence spectra. Unless otherwise indicated, data which is compared in the following chapter was recorded in what is referred to in the following as a *scan*, meaning that all the spectra were recorded without significant interruptions in-between and that only one parameter was varied. This is important because, as was pointed out before, the experimental conditions at SASE-FELs not only fluctuate from shot to shot, but may also differ from day to day. The only additional parameter which was varied within scans was the exposure time, as the small clusters generated with low gas pressures produce less fluorescence than large clusters, simply because fewer particles are in the interaction region. Mostly, an exposure time between 2 and 10 minutes was used, equal to an accumulation over 1200 to 6000 FEL shots. For each exposure time within a scan, we recorded a background image, where the FEL was allowed to enter the chamber but the cluster source was turned off. Such a background image was automatically subtracted from each spectrum to ensure that straylight of the FEL hitting surfaces within the chamber or straylight from the outside did not have an effect on the spectra. In order to give an impression of the raw data aquired with the spectrometer, I included figure 4.1. It shows a xenon spectrum recorded at an FEL intensity of approximately $1 \cdot 10^{15}$ W/cm^2. The average cluster size is 6700 atoms. The exposure time was 2 minutes. To generate a spectral plot, if not otherwise indicated in the following chapters the following procedure was used:

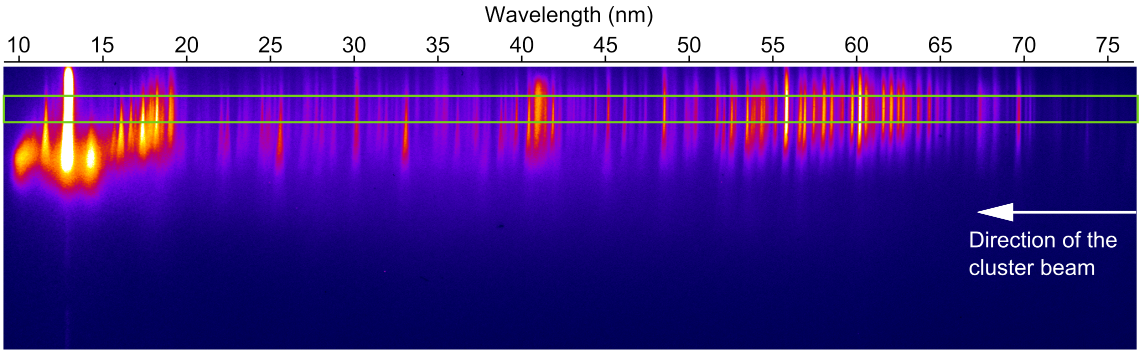

Figure 4.1.: A spectrum of xenon clusters with an average size of 6700 atoms at an FEL intensity of $\sim 1 \cdot 10^{15}$ W/cm^2 (in false color to make the features more easily discernible). The green rectangle indicates the nominal focus of the spectrometer which is evaluated for each spectrum. An approximate wavelength scale and an indication of the direction of the cluster beam have been added as an orientation help.

1. A narrow region of the spectrum is chosen, as is indicated by the green rectangle in figure 4.1. This region represents the vertical dimension which can be properly focused by the spectrometer grating. It has a height of 48 pixels (between pixels 66 and 114 in the raw images) and is situated in the middle of the spectral lines. The signal is summed vertically, along the direction of the spectral lines.

2. Spectra, although recorded in the same scan, show different offsets to the baseline after background subtraction. A possible explanation could be stray light from clusters that does not reach the detector via the grating but via scattering from metallic surfaces. Broadening of spectral lines due to inferior focusing at low FEL intensities (see figure 4.2) could also play a role. Therefore, each spectrum is shifted after background subtraction so that its minimum value is equal to 0.

3. If different exposure times were used, the spectra with longer exposure times are scaled down accordingly.

4. If the recorded FLASH machine data show different average pulse energies for different spectra in the same scan, which in turn affects the FEL intensity in the focus, the spectra are corrected by multiplying them by a factor $E_{\mathrm{max}}/E_{\mathrm{sp}}$, where E_{max} is the highest average pulse energy in the scan and E_{sp} is the average pulse energy of the spectrum which is being corrected[1].

5. For the scans in which the cluster size was varied by varying the gas pressure, a similar correction is necessary. According to the ideal gas law, a linear increase in pressure would lead to a linear increase in the number of particles. Assuming there were no cluster formation, this would just equate to an increased number of atoms in the interaction region. More atoms naturally lead to an increase in signal. Such an increase, however, is not what we are interested in. We want to find out if there is a change in the signal which is due to the changing of the cluster size, i.e. the condensation of atoms.
   Therefore, we allow for the increased particle number by multiplying each spectrum of a cluster size scan by a factor $p_{\mathrm{max}}/p_{\mathrm{sp}}$, where p_{max} is the pressure of the spectrum with the largest cluster size and p_{sp} is the pressure of the spectrum which is being corrected. This step can be thought of as normalizing each spectrum to the same number of total atoms present in the interaction region, the only difference between them being the size of the clusters that are formed.

6. The last step is accounting for the wavelength-dependent efficiency of the spectrometer as is outlined in chapter 4.1.2.

A close look at the spectral lines in figure 4.1 shows that the lines become broader at the top and at the bottom. In the vertical direction, the spectral lines are an image of the source point. The source point has an hourglass shape in the FEL focus, since the FEL focus converges toward the focal point and diverges after it. The second factor which contributes to the widening of the lines is that the grating cannot accurately focus light which is emitted from a point other than the nominal source point. Whenever one compares line widths, these two factors play a role. The spectrum also shows the effect of the FEL intensity on different lines. The above spectrum was not recorded with the FEL focus located in the nominal focus of the spectrometer. For most of the lines on the right side of the spectrum, the maximum fluorescence yield lies within the rectangle indicated in green. For the ones on the left, though, maximum fluorescence is achieved further down, at the FEL focus position (highest FEL intensity). The reason for the missing hourglass shape close to the FEL focus is the spectral resolution of the spectrometer grating outside its nominal focus. This is illustrated in figure 4.2.

The first section of this chapter deals with the calibration of the spectra. After a wavelength

---

[1] This method cannot, of course, make spectral lines appear in spectra in which the real intensity was too low to produce the charge state required for this particular line. It also neglects the possibility of a particular charge state and its spectral lines being produced by multiphoton processes. Multiphoton processes scale with I^n, where I is the FEL intensity in the interaction region and n is the number of photons needed. However, the normalization always comes closer to the true result one would have gotten if the FEL pulse energy had stayed constant.

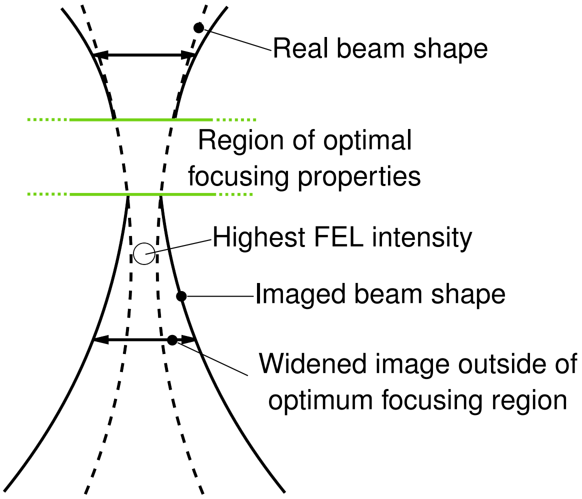

Figure 4.2.: Schematic drawing illustrating the evaluation of a spectrum recorded at less than maximum FEL intensity, as seen in figure 4.1. Spectra are only evaluated in the region where the spectrometer has optimal focusing properties. This region is located between the two green lines. The refocusing mirror has been moved, so that the FEL focus is below this region. In the FEL focus, the highest charge states are produced and the FEL beam is narrowest at this point. However, because of the bad focusing properties of the diffraction grating outside of the above region, the *image* of the FEL focus is widened so much that it appears wider than the portion of the beam situated in the focal region. Therefore, the spectra only show the image of an hourglass shape when the FEL focus is in the middle of the focal region.

scale has been established, spectral lines are assigned to specific charge states. In order to achieve this, the intensity scans are evaluated. The next section deals with effects of the cluster size and compares atomic and cluster spectra. The last section compares the spectra of pure xenon, pure argon and xenon-core-argon-shell clusters.

4.1. Calibration of the spectrometer

The first, and essential, step in analyzing the data is assigning a reliable wavelength scale to the spectra. The nominal wavelength scale has been calculated in the previous chapter and if one could be sure that all the design parameters are met in the experiment, this would be sufficient. However, there are a number of points where a deviation from the design is highly likely: the manufacturing of the spectrometer components and of the vacuum chamber, the mounting of the components with respect to each other, the adjustment of the position of the focusing mirror and the diffraction grating and also pointing instabilities of the FLASH beam. All these uncertainties dictate a wavelength calibration of the acquired spectra. One possible way to do this is by comparing our data with published data, as shown in the next section.

4.1.1. Comparison with published data

Not much fluorescence data of rare gases in the XUV wavelength range has been published, and even less close enough to our experimental conditions to show even a passing resemblance to our spectra.

Figure 4.3 shows data from Böwering et al. [69] and Brühl [91]. Böwering et al. cover experiments performed with a plasma focus discharge developed for XUV lithography. They also did theoretical work to determine the spectral line positions. The analyzed wavelength range extends from 8.5 to 20.5 nm. Brühl studied the fluorescence emission from 17 to 39 nm of atomic xenon irradiated with a synchrotron source. To calibrate our spectra, the published data were digitized to make the comparison easier. The measurements of Böwering et al. show high similarity to our spectra at the highest FEL intensity of $2.5 \cdot 10^{15}$ W/cm^2, whereas the spectral distribution of the data of Brühl is more easily recognized in our spectra at lower intensity $0.4 \cdot 10^{15}$ W/cm^2. This is a consequence of intensity dependent charge state formation that will be discussed in detail in chapter 4.2.1.

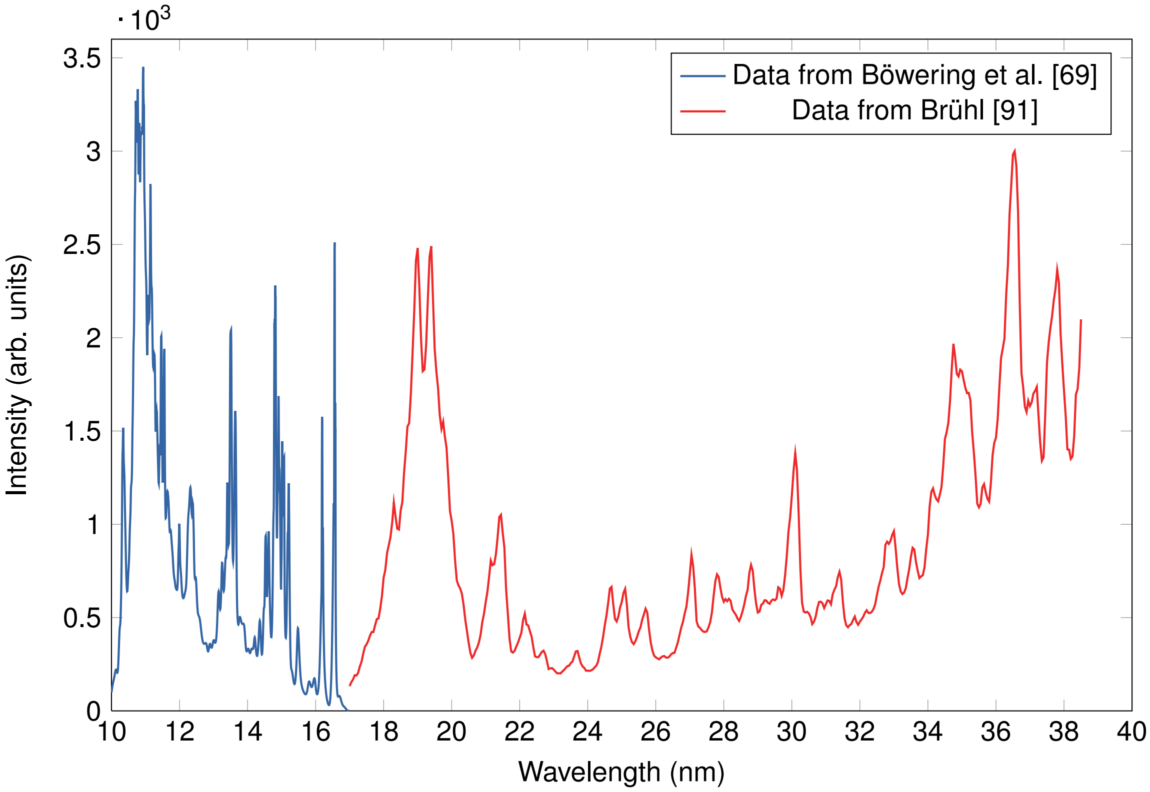

Figure 4.3.: Xenon fluorescence spectra measured by Böwering et al. [69] in a plasma focus discharge and by Brühl [91] at a synchrotron facility. The spectra were used to calibrate the data of this thesis (see text and table 4.1).

However, even though different spectra of ours are optimally suited for the comparison with the reference spectra, the calibration of the wavelength scale was performed on one spectrum, recorded at an FEL intensity of $1.5 \cdot 10^{15}$ W/cm^2. This is a compromise between the two intensities of highest similarity mentioned above. The obtained assignment was subsequently transferred to the other spectra, because individual measurements are shifted randomly with respect to each other by a few pixels. A possible explanation for this behavior are pointing instabilities of the FEL beam[2].

Table 4.1 lists the peaks which were chosen for the calibration. The assignment of fluorescence lines to certain transitions of (multiply charged) ions will be discussed in chapter 4.2.1. With these sampling points, a fit is calculated which modifies the nominal wavelength scale, which was introduced in chapter 3.1.4, in the following way:

---

[2] A wandering interaction point, which could be caused by a possibly misaligned refocusing mirror, does not account for the shifting, as it is randomly distributed and not correlated with the mirror position.

Uncalibrated line positions (nm)	Corresponding published line (nm)
11.17	11.14
11.98	11.99
12.31	12.34
15.63	15.48
15.98	15.81
16.08	15.95
16.34	16.17
16.73	16.53
30.57	30.1
39.06	38.5

Table 4.1.: Peaks which were chosen to calibrate the xenon spectra.

$$\lambda_{\mathrm{kal}} = 0.52495 + 0.94764 \cdot \lambda_{\mathrm{nom}} + 6.4 \cdot 10^{-4} \cdot \lambda_{\mathrm{nom}}^2 \tag{4.1}$$

Now, the first spectrum has a calibrated wavelength scale. In order to transfer the calibration to the remaining spectra, they are shifted so that the scattered light peak of all spectra is centered at the same pixel value. (If the machine data confirms that the wavelength was constant during the scan.) This procedure ignores the fact that a different angle of incidence on the grating should very slightly change the dispersion of the grating. However, even at long wavelengths, the lines appear at the same positions within the resolution of the spectrometer, so shifting the scattered light peaks to the same position is a valid way of calibration.

Figure 4.4 shows the data of Böwering et al. and one of our spectra from xenon clusters consisting of approximately 6700 atoms, recorded at maximum FEL intensity. Our spectra have a lower resolution but the major structures are clearly reproduced. Figure 4.5 shows the same kind of comparison with the data of Brühl. Here, a cluster spectrum at $0.4 \cdot 10^{15}$ W/cm^2 is used. Many spectral features can be recognized. The very different experimental conditions of Brühl at a synchrotron facility, compared to our FEL studies, can explain the noticable difference in abundace of some spectral lines.

This method of calibration was also used for the spectra of argon and core-shell-clusters because the peak of scattered FEL radiation can be found in those spectra as well.

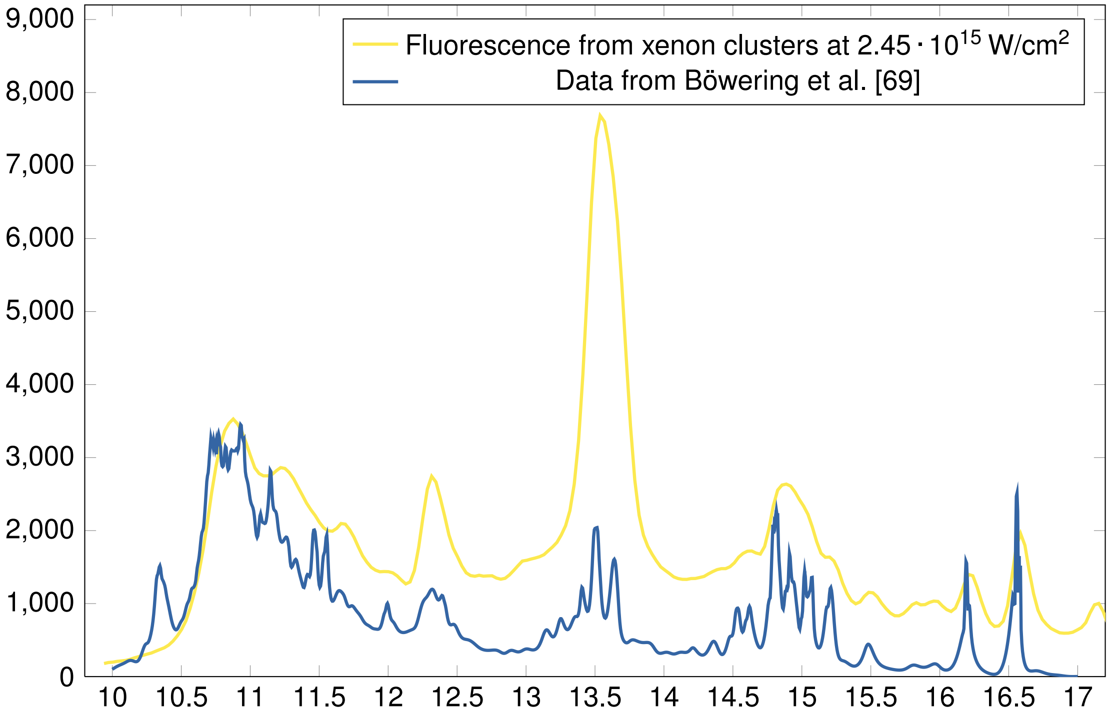

Figure 4.4.: Comparison between the data from Böwering et al. [69] and a spectrum of xenon clusters consisting of approximately 6700 atoms, recorded at maximum FEL intensity.

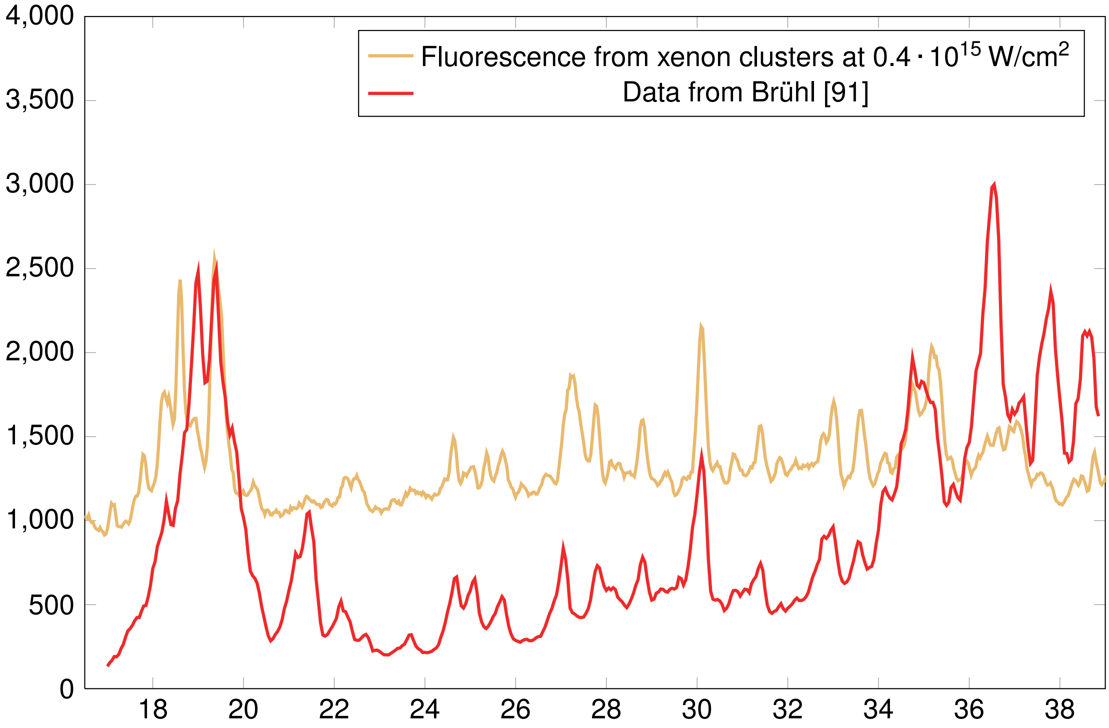

Figure 4.5.: Comparison between the data from Brühl [91] and a spectrum of xenon clusters consisting of approximately 6700 atoms, recorded at $0.4 \cdot 10^{15}$ W/cm^2.

4.1.2. Correcting for grating efficiency and detector efficiency

Whenever one wants to compare the fluorescence yield of different regions of a single spectrum, it is necessary to account for the varying sensitivity of the spectrometer across its wavelength range. Both the efficiency of the diffraction grating and the quantum efficiency of the XUV camera are not flat but show significant changes across the spectrum, as was already shown in figure 3.6. By dividing each point of a spectrum by the corresponding value of the combined efficiencies of the diffraction grating and the XUV camera the influence of the spectrometer efficiency on the spectra is accounted for.

4.1.3. Resolution of the spectrometer

Having measured a spectrum, determining the resolution $\lambda/\Delta\lambda$ of the spectrometer is a simple matter of measuring the full width at the half maximum (FWHM) of several lines and multiplying its inverse by the respective wavelength position. Care must be taken to choose lines which presumably do not consist of a superposition of several lines. Table 4.2 lists the width of several lines across the range of the spectrometer, measured either for argon or for xenon. As can be seen, the width of the lines does not change significantly across the spectrum but, since the resolution depends on the wavelength of the spectral line, the resolution increases towards longer wavelengths.

Wavelength postion (nm)	Line width $\Delta\lambda$ (nm)	$\frac{\lambda}{\Delta\lambda}$
12.3	0.23	53
15.2	0.18	84
16.6	0.19	87
25.7	0.21	122
29.9	0.17	176
33	0.19	174
46.3	0.21	220
47.6	0.17	280
55.4	0.17	326
58.5	0.13	450
63.5	0.17	374
69.5	0.19	366
73.6	0.15	491

Table 4.2.: Measured resolution of the spectrometer.

It can also be seen that the width of the lines is not strongly correlated to wavelength position. Narrow lines can be found in any part of the spectrum, with slightly broader ones scattered in-between. The most likely explanation is that, even though each line appears smooth and uniform, it consists of contributions from several transitions, with the possible exception of the line at 58.5 nm. In this sense, the given resolution should be taken as a lower experimentally derived boundary in comparison to the theoretically expected values of $\lambda/\Delta\lambda_{@12.3\,\text{nm}} = 197$ and $\lambda/\Delta\lambda_{@73.6\,\text{nm}} = 1067$.

4.2. Xenon clusters

4.2.1. Identifying charge states

One main purpose of this experiment is, as was stated before, the identification of charge states initially created in the clusters, before possible recombinations. This is not an easy task, because not too much data has been published covering the whole wavelength range we observed.

Dependence of xenon charge states on FEL intensity

A promising way of getting a grip on the charge states that are generated by the FEL is to vary the intensity and to compare the resulting spectra. It is to be expected that higher charge states will require higher intensities to be produced than lower charge states. Groups of spectral lines which peak at the same FEL intensity should, in first order approximation, originate from the same charge state. Figure 4.6 shows fluorescence spectra of xenon clusters measured at varying FEL intensities. The clusters had an average size of approximately 6700 atoms. The spectra shown have not yet been corrected with respect to the spectrometer efficiency. For the analysis in this section, this is valid because no comparisons between lines of different wavelengths within

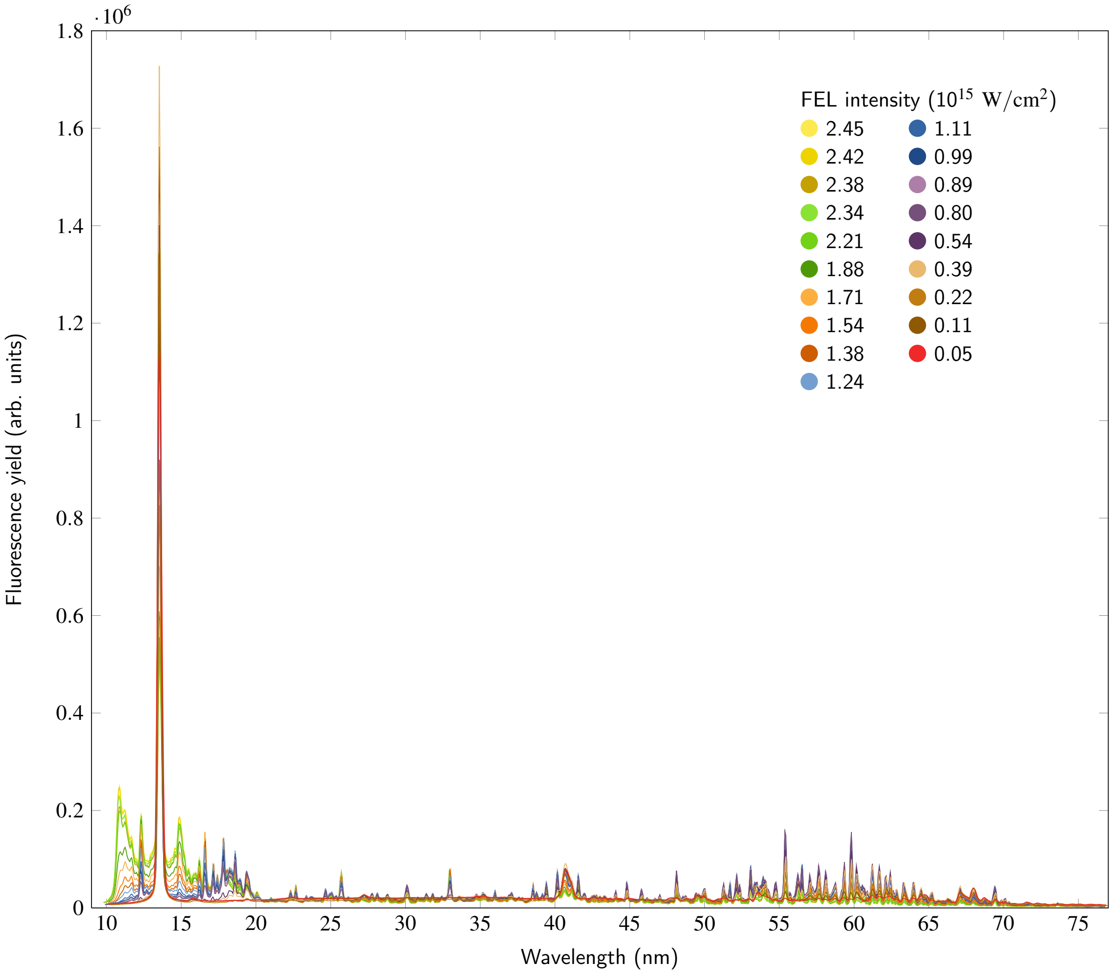

Figure 4.6.: Spectra of xenon clusters with an average size of about 6700 atoms at different FEL intensities. The spectrometer efficiency has not yet been accounted for.

the same spectrum are made. I only compare the peak heights and ratios of the same spectral line for different FEL intensities.

As can be seen, the fluorescence yield at short wavelengths increases significantly for higher FEL intensity. This is shown in more detail in figures 4.7: figure 4.6 has been split up and magnified and each peak has been marked with a colored circle corresponding to the FEL intensity at which the spectral line reaches its maximum value. The general trend is that spectral lines which reach their maximum value at higher FEL intensity are situated at shorter wavelengths.

From Böwering et al. [69] it is known to which charge states the peaks from 10 to 20 nm correspond. The highest charge states, of at least 11+, peak at the highest FEL intensity. The 9+ peak at 15 nm reaches its maximum at the second-highest intensity. The 8+ peak at 16.5 nm peaks at an even lower FEL intensity of about $2/3$ of the maximum value. Unfortunately, the peak at 16.2 nm, which has also been attributed to Xe^{8+}, shows a small deviation from the general trend; it reaches its maximum for the highest intensity. However, slightly lower FEL intensities than the peak value result in virtually the same fluorescence yield for this line. Peaks from 17 to 19 nm have been assigned by Böwering et al. to Xe^{7+}. Again, the intensity responsible for the maximum value is lower than for the higher charge states. All these observations show that, while not a fool-proof way to pin-point the exact charge states, this analysis seems to portray the charge state distribution over the whole spectrum reasonably well.

Looking at the result of this evaluation over the whole spectrum, one sees that areas are dominated by certain FEL intensities, which are represented by specific colors as defined in figure 4.7. From 23 to 57 nm light blue circles, i.e. intensities of half the maximum value are prevalent. Most lines between 44 and 64 nm peak at FEL intensities of about $1/4$ of the maximum value. These must correspond to an even lower charge state. Between 61 and 67 nm lines appear which reach their maximum at FEL intensities of about $1/8$ of the maximum value, again a significant difference to the preceding peaks and therefore likely a lower charge state. Peaks at 68 and 68.7 nm reach their maximum at about a third of the previous intensity. Finally, lines between 64 and 76 nm max out at the lowest FEL intensity that we used in this scan of about $1/50$ of the maximum value.

The sheer amount of possible lines, combined with the comparatively low resolution of our spectrometer, makes it in many cases difficult to unambiguously assign a specific transition to a spectral line. However, as was shown, there is a clear correlation between the FEL intensity responsible for maximizing the yield of a certain spectral line and the charge state of that line according to Böwering et al.. Therefore, we now have a basis for comparing all spectral lines with tabulated values found in the NIST (National Institute of Standards and Technology) atomic spectra database [67]. This database comprises many papers which have measured spectral lines of atoms. By looking for correlations between the Böwering data, our FEL intensity dependent evaluation and possible candidates given in the NIST data base we can assign specific charge states to about half of the lines in the spectrum and a narrow region ($q \pm 1$) of charge states to a few more lines. The results are shown in table 4.3. By this method, no charge state could be assigned to about 60 lines, or about $2/5$ of all lines. 34 of those lines occur at wavelengths at which no line is tabulated in the NIST database. These lines are marked 'unknown' in table 4.3. The remaining spectral lines show no correlation between the FEL intensity dependent evaluation and the lines in the NIST database at those wavelengths. These lines are marked 'no fit' in table 4.3. Many of the unidentified lines could be assigned by an evaluation procedure which is described in chapter 4.2.1. The charge states which were assigned in this way are written in red in table 4.3.

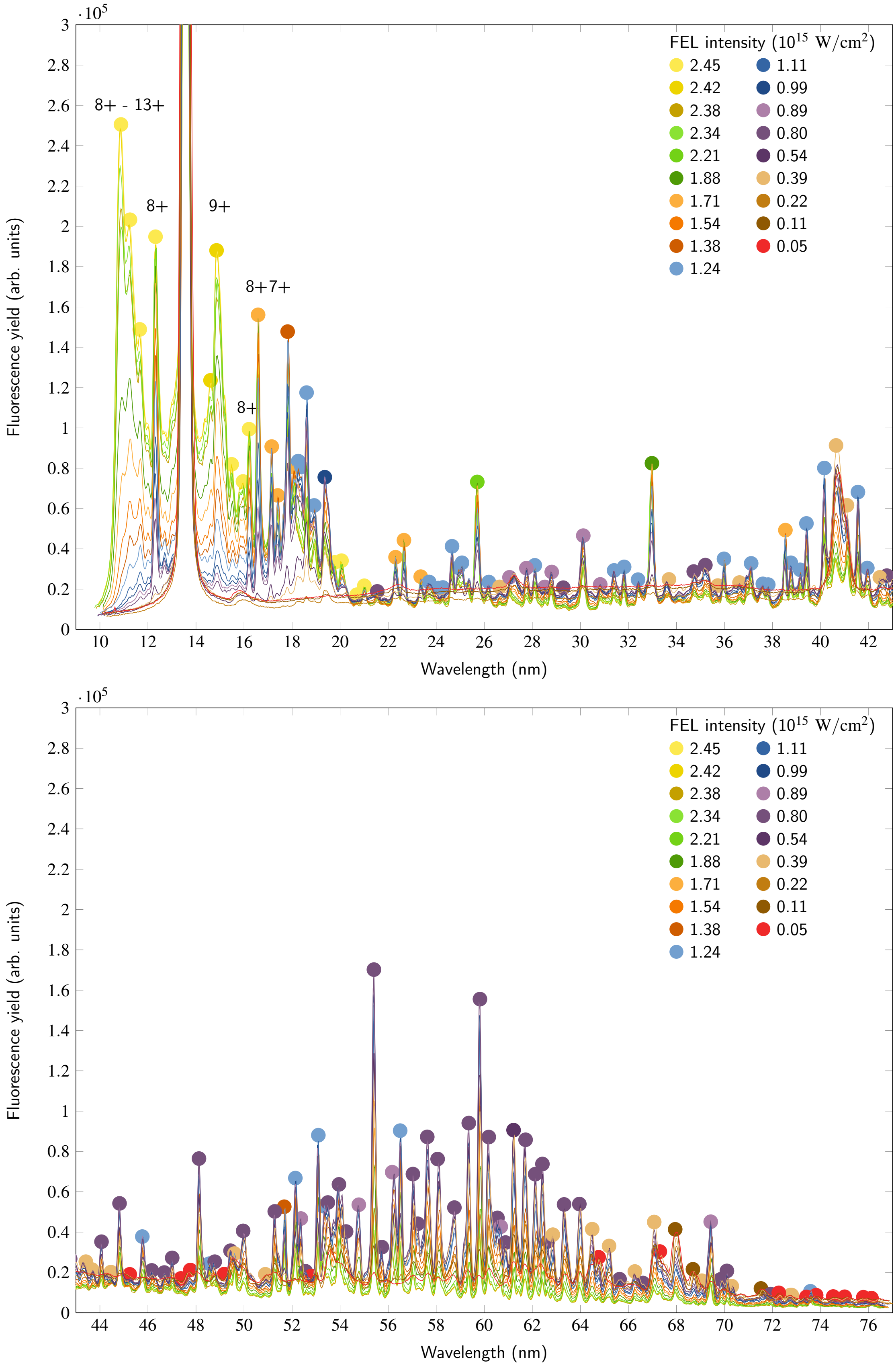

Figure 4.7.: Evolution of fluorescence yield in dependence on FEL intensity from xenon clusters with an average size of about 6700 atoms. Colored circles indicate the intensity at which the respective peak reaches its maximum. The spectrometer efficiency has not yet been accounted for.

Measured (nm)	NIST (nm)	Transition (Configuration, Term, J)	Charge state	Color code
10.9	no fit		>10+	●
11.3	11.3021	$4p^6 4d^7 4f$, mix, 4 - $4p^6 4d^8$, ^1G, 4	10+	●
11.7	2 poss		9+	●
12.3			8+	●
13.5	FEL stray			●
14.6	14.5983	$4d^8 5p$, mix, $5/2$ - $4d^9$, ^2D, $3/2$	9+	●
14.9	many poss		9+	●
15.5	15.4935	$4d^8 5p$, mix, $3/2$ - $4d^9$, ^2D, $3/2$	9+	●
16.0	15.9387	$4d^8 5p$, mix, $3/2$ - $4d^9$, ^2D, $3/2$	9+	●
16.2	16.1742	$4d^9 5p$, $^3D^o$, 1 - $4d^{10}$, ^1S, 0	8+	●
16.6	16.5323	$4d^9 5p$, $^1P^o$, 1 - $4d^{10}$, ^1S, 0	8+	●
17.2	17.0856	$4d^9(^2D_{5/2})5s5p(^1P^o_1)$, $5/2^{2,1}P^o_1$, $3/2$ - $5s$, ^2S, $1/2$	7+	●
17.4	17.4147	$4d^9(^2D_{3/2})5s5p(^3P^o_2)$, $3/2^{2,3}P^o_2$, $3/2$ - $5s$, ^2S, $1/2$	7+	●
17.8	17.77	$4d^9(^2D_{3/2})5s5p(^3P^o_1)$, $3/2^{2,3}P^o_1$, $3/2$ - $5s$, ^2S, $1/2$	7+	●
18.1	17.966	$4d^9(^2D_{3/2})5s5p(^3P^o_0)$, $5/2^{2,3}P^o_2$, $3/2$ - $5s$, ^2S, $1/2$	7+	●
18.3	18.188	$4d^9 5s^2 5p$, $^3D^o$, 1 - $5s^2$, ^1S, 0	6+	●
18.4	unknown		6+	●
18.6	18.544	$4d^9 5s^2 5p$, $^1P^o$, 1 - $5s^2$, ^1S, 0	6+	●
18.9	unknown		6+	●
19.4	unknown			●
19.8	unknown			●
20.1	unknown			●
20.7	unknown			●
21.0	unknown		7+	●
21.5	unknown		6+	●
22.3	22.28	$7s$, ^2S, $1/2$ - $5p$, $^2P^o$, $1/2$	7+	●
22.7	22.554	$6p$, $^2P^o$, $1/2$ - $5s$, ^2S, $1/2$	7+	●
23.4	23.243	$7s$, ^2S, $1/2$ - $5p$, $^2P^o$, $3/2$	7+	●
23.7	unknown		6+	●

24.1	unknown		6+	🔵
24.3	unknown		6+	🔵
24.7	24.522	$5s6p$, $^1P^o$, 1 - $5s^2$, ^1S, 0	6+	🔵
24.9	24.944	$5s6p$, $^3P^o$, 1 - $5s^2$, ^1S, 0	6+	🔵
25.1	unknown		6+	🔵
25.7	25.56	$6g$, ^2G, 9/2 - $4f$, $^2F^o$, 7/2	7+	🟢
26.2	unknown		6+	🔵
26.6	unknown		6+	🟡
27.1	unknown		6+	🟣
27.8	unknown			🟣
28.1	unknown		6+	🔵
28.5	unknown		6+	🟣
28.8	unknown		6+	🟣
29.3	unknown		6+	🟣
30.1	unknown			🟣
30.8	unknown		6+	🟣
31.4	unknown		6+	🔵
31.8	unknown		6+	🔵
32.4	unknown		6+	🔵
33.0	32.84	$5g$, ^2G, 9/2 - $4f$, $^2F^o$, 7/2	7+	🟢
33.7	unknown		6+	🟡
34.7	unknown		6+	🟣
35.2	unknown		6+	🟣
35.7	no fit			🟡
36.0	36.04	$5s7p$, $^3P^o$, 2 - $5p^2$, ^3P, 2	6+	🔵
36.6	36.617	$4f5p$, ^1D, 2 - $5s5p$, $^1P^o$, 1	6+	🟡
37.1	unknown		6+	🔵
37.6	unknown		6+	🔵
37.8	unknown		6+	🔵
38.5	38.4	$6s$, ^2S, 1/2 - $5p$, $^2P^o$, 3/2	7+	🟠
38.8	38.656	$5s6s$, ^3S, 1 - $5s5p$, $^3P^o$, 0	6+	🔵
39.2	39.311	$5s6s$, ^3S, 1 - $5s5p$, $^3P^o$, 1	6+	🔵
39.4	39.392	$5p6s$, $^1P^o$, 1 - $5p^2$, ^1D, 2	6+	🔵
40.2	no fit		6+	🔵
40.6	unknown			🟡
41.1	unknown			🟡
41.6	41.467	$5s6s$, ^3S, 1 - $5s5p$, $^3P^o$, 2	6+	🔵
41.9	41.998	$5p6s$, $^1P^o$, 1 - $5p^2$, $^3P^o$, 2	6+	🔵

42.5	no fit		6+	●
42.8	no fit			●
43.4	no fit			●
43.7	no fit		6+	●
44.1	no fit			●
44.5	44.416	$4d^95f$, $^1P^o$, 1 - $4d^95d$, ^3F, 2	8+	●
44.8	44.747	$5s^26s$, ^2S, 1/2 - $5s^25p$, $^2P^o$, 1/2	5+	●
45.2	no fit			●
45.8	45.785	$5s6s$, ^1S, 0 - $5s5p$, $^1P^o$, 1	6+	●
46.2	no fit			●
46.7	no fit			●
47.0	no fit			●
47.4	no fit			●
47.8	no fit			●
48.1	48.105	$5s^26s$, ^2S, 1/2 - $5s^25p$, $^2P^o$, 3/2	5+	●
48.5	no fit		6+	●
48.8	no fit			●
49.4	49.425	$5p5d$, $^1F^o$, 3 - $5p^2$, ^1D, 2	6+	●
49.5	49.625	$5s^25p^3(^2D^o)6d$, $^3D^o$, 2 - $5s^25p^4$, ^3P, 2	2+	●
49.6	no fit			●
50.0	50.0558	$5s^25p(^2P^o)6s$, $^3P^o$, 2 - $5s^25p^2$, ^3P, 1	4+	●
50.9	50.95243	$5s^25p^3(^2D^o)6d$, $^3G^o$, 3 - $5s^25p^4$, ^3P, 2	2+	●
51.3	51.2973	$5s^25p(^2P^o)6s$, $^3P^o$, 2 - $5s^25p^2$, ^3P, 2	4+	●
51.7	51.7007	$5d$, ^2D, 3/2 - $5p$, $^2P^o$, 1/2	7+	●
52.1	52.1408	$5s5p5d$, mix, 5/2 - $5s5p^2$, ^2D, 3/2	5+	●
52.4	52.4474	$5s^25p(^2P^o)5d$, $^1P^o$, 1 - $5s^25p^2$, ^3P, 1	4+	●
52.6	no fit			●
52.8	52.8235	$5s^25p^3(^2D^o)6d$, $^3S^o$, 1 - $5s^25p^4$, ^3P, 1	2+	●
53.1	53.118	$5s5d$, ^3D, 2 - $5s5p$, $^3P^o$, 1	6+	●
53.3	53.376	$5p5d$, $^3D^o$, 1 - $5p^2$, ^3P, 0	6+	●
53.5	53.565	$5s5p5d$, mix, 1/2 - $5s5p^2$, ^4P, 3/2	5+	●
54.0	54.0713	$5s^25p(^2P^o)6s$, $^3P^o$, 1 - $5s^25p^2$, ^3P, 1	4+	●

54.2	54.3043	$5s^25p(^2P^o)5d$, $^3P^o$, 1 - $5s^25p^2$, ^3P, 0	4+	●
54.8	54.74	$5s5p5d$, mix, 3/2 - $5s5p^2$, $^4P^o$, 1/2	5+	●
55.4	55.4786	$5s^25d$, ^2D, 3/2 - $5s^25p$, $^2P^o$, 1/2	5+	●
55.7	55.824	$5s5p5d$, mix, 5/2 - $5s5p^2$, ^4P, 5/2	5+	●
56.2	56.171	$5s5p5d$, mix, 7/2 - $5s5p^2$, ^4P, 5/2	5+	●
56.5	56.605	$5s5d$, ^3D, 3 - $5s5p$, $^3P^o$, 2	6+	●
57.0	no fit			●
57.2	57.19	$5s^25p(^2P^o)5d$, $^3P^o$, 1 - $5s^25p^2$, ^3P, 1	4+	●
57.6	many poss			●
58.1	no fit			●
58.8	58.816	$5s^25p(^2P^o)5d$, $^3P^o$, 1 - $5s^25p^2$, ^3P, 2	4+	●
59.4	59.424	$5s5p5d$, mix, 3/2 - $5s5p^2$, ^2S, 1/2	5+	●
59.8	59.985	$5s^25d$, ^2D, 5/2 - $5s^25p$, $^2P^o$, 3/2	5+	●
60.2	no fit		5+	●
60.7	60.735	$5s^25d$, ^2D, 3/2 - $5s^25p$, $^2P^o$, 3/2	5+	●
60.9	60.890	$5s5p5d$, mix, 3/2 - $5s5p^2$, ^2P, 3/2	5+	●
61.2	no fit		5+	●
61.7	61.66	$5s5p5d$, mix, 5/2 - $5s5p^2$, ^4P, 3/2	5+	●
62.1	62.07	$5s5p5d$, mix, 3/2 - $5s5p^2$, ^2D, 3/2	5+	●
62.4	62.49	$5s5p5d$, mix, 7/2 - $5s5p^2$, ^4P, 5/2	5+	●
62.7	62.697	$5s5p5d$, mix, 5/2 - $5s5p^2$, ^2D, 3/2	5+	●
62.9	62.915	$5s^25p(^2P^o)5d$, $^3D^o$, 1 - $5s^25p^2$, ^3P, 2	4+	●
63.3	63.293	$5s5p^2$, ^2S, 1/2 - $5s^25p$, $^2P^o$, 1/2	5+	●
64.0	63.994	$5s5p5d$, mix, 1/2 - $5s5p^2$, ^2S, 1/2	5+	●
64.5	64.633	$5s^25p^2(^1S)5d$, ^2D, 3/2 - $5s^25p^3$, $^2P^o$, 3/2	3+	●
64.8	no fit			●
65.2	65.368	$5s^25p^2(^3P)6s$, ^4P, 5/2 - $5s^25p^3$, $^2D^o$, 5/2	3+	●
65.6	unknown			●
66.3	66.341	$5s5p^4$, ^2S, 1/2 - $5s^25p^3$, $^4S^o$, 3/2	3+	●

66.6	no fit			🟣
67.1	67.2565	$5s^25p^2(^3P)5d$, ^4D, $5/2$ - $5s^25p^3$, $^4S^o$, $3/2$	3+	🟡
67.3	67.3796	$5s^25p^3(^2D^o)5d$, $^1F^o$, 3 - $5s^25p^4$, ^3P, 2	2+	🟡
67.9	68.0606	$5p^4(^3_1)6d$, $^2[3]$, $5/2$ - $5p^5$, $^2P^o$, $3/2$	1+	🟤
68.7	68.8038	$5s^25p^3(^2P^o)5d$, $^3F^o$, 3 - $5s^25p^4$, ^3P, 2	2+	🟤
69.1	69.103	$5s^25p^3(^2D^o)5d$, $^1D^o$, 2 - $5s^25p^4$, ^1D, 2	2+	🟡
69.4	69.459	$5s5p5d$, mix, $3/2$ - $5s^25d$, ^2D, $5/2$	5+	🟣
69.8	69.855	$5s^25p^2(^1D)5d$, ^2G, $7/2$ - $5s^25p^3$, $^2D^o$, $5/2$	3+	🟣
70.1	70.1377	$5s^25p(^2P^o)5d$, $^3P^o$, 2 - $5s^25p^2$, ^1D, 2	4+	🟣
70.3	70.357	$5s^25p^2(^3P)5d$, ^4P, $5/2$ - $5s^25p^3$, $^2D^o$, $5/2$	3+	🟡
71.5	71.5987	$5s^25p^3(^2D^o)5d$, $^3S^o$, 1 - $5s^25p^4$, ^3P, 0	2+	🟤
71.9	2 poss		1+ or 2+	🟣
72.3	2 poss		2+	🔴
72.7	72.864	$5s^25p^2(^1D)5d$, ^2P, $1/2$ - $5s^25p^3$, $^2P^o$, $3/2$	3+	🟡
73.4	no fit			🔴
73.6	73.7206	$5p^2$, ^1D, 2 - $5s5p$, $^3P^o$, 1	6+	🔵
73.8	many poss		1+ or 2+	🔴
74.5	74.4138	$5s^25p^3(^2P_0)6s$, $^3P^o$, 1 - $5s^25p^4$, ^1D, 2	2+	🔴
75.0	3 poss		2+ or 1+	🔴
75.8	75.8466	$5p^4(^3P_1)7s$, $^2[1]$, $3/2$ - $5p^5$, $^2P^o$, $1/2$	1+	🔴
76.1	76.1781	$5s^25p^3(^2D^o)5d$, $^3P^o$, 2 - $5s^25p^4$, ^1D, 2	2+	🔴

Table 4.3.: Xenon: Comparison of measured wavelengths with tabulated values from the NIST database [67]. The 2nd, 3rd and 4th columns are taken from the NIST database. The color code gives the FEL intensity which maximizes the peak as seen in figure 4.7. The label 'mix' denotes terms which are comprised of a complex mixture of different terms. Charge states in red could not be assigned via the NIST database but are based on a comparison of lines which is described in chapter 4.2.1.

Having pinned down those values which can be found in the NIST database, the next step is to try to assign charge states to the lines which are not tabulated in the NIST database. This can be done by comparing the evolution of unknown lines to that of assigned lines. The procedure is described in the next section.

Comparison of the evolution of spectral lines depending on FEL intensity

A more refined way of analyzing the data is to not just take into account those spectra which maximize a certain peak, but to compare the ratio of peak values for all FEL intensities. In other words, one identifies peaks which grow and shrink in similar ways in dependence on the FEL intensity. This analysis is especially useful to assign charge states to spectral lines which are not tabulated in the NIST database by being able to link them to other, known, lines.

In more detail, one proceeds as follows:

Starting with a single spectrum for a single FEL intensity, the first spectral line in the spectrum is chosen as the reference line. Now the ratios of this reference peak and all other peaks in the spectrum are calculated. To ensure a symmetric matrix, the larger value is always divided by the smaller one. For a spectrum with 151 peaks, this gives 150 ratios (plus the ratio of 1 where the reference peak is compared to itself). These 151 values are stored in the first row of a matrix.

As the next step, the second spectral line in the spectrum is chosen as the reference line and the above procedure is repeated. The resulting values are stored in the second row of the matrix. After all peaks have been chosen as the reference peak, one ends up with a 151×151-matrix for each fluorescence spectrum, with a diagonal consisting of ones, where each line has been compared to itself.

This analysis is performed for all spectra taken as function of FEL intensity[3]. Now it is possible to compute a mean value $\overline{x}_{ij}$ over the different FEL intensities for each position in the matrix. The index i denotes the row, j denotes the column. The standard deviation σ_{ij} is also calculated, by the following formula.

$$\sigma_{ij} = \left(\frac{1}{n-1} \sum_{k=1}^{n} (x_{ij_k} - \overline{x}_{ij})^2 \right)^{1/2} \tag{4.2}$$

Here, n is the total number of spectra. The index k designates each spectrum. Consequently, x_{ij_k} is the matrix element for spectrum k in line i and row j.

The different matrices of an intensity dependent scan are summarized in a single correlation matrix where each value is replaced by the value $\sigma_{ij}/\,\overline{x}_{ij}$. Each value in the correlation matrix is a measure of how closely two spectral lines are correlated in their intensity dependent behavior, i.e. if they may belong to the same charge state. The closer to 0, the stronger the correlation, because in the extreme case of two spectral lines developing in exactly the same way, the ratio is always 1 and the standard deviation is 0. Consequently, the matrix element in the correlation matrix is 0, too. This is obviously the case on the diagonal of the correlation matrix (self-correlation).

Figure 4.8 shows a color-coded representation of such a correlation matrix. Most points of high correlation are relatively close to the diagonal, which means they are spectrally close together. It confirms the result from the peak maximum analysis in chapter 4.2.1 that the charge states are distributed across the spectrum in groups belonging to different charge states[4]. To see which peaks evolve in a similar way, one can sort the data so that all peaks which are correlated are assigned to the same 'compartment'. To clarify, by the term *correlation* I refer to the following:

---

[3] For the analysis, the spectrum was divided into segments, because not all FEL intensities are sufficient to create the charge states responsible for spectral lines in certain regions. Incorporating all the FEL intensities for each line would have meant unnecessarily incorporating noise. Therefore, between 10 and 17 nm the 5 lowest FEL intensities were left out, from 17 to 45 nm the 3 lowest intensities were left out and only from 45 to 76 nm were all FEL intensities considered. This segmentation was chosen by eye from a plot of the spectra as in figure 4.7.

[4] With some notable exceptions, where strong correlations are found between fluorescence lines that are relatively far apart from each other in the spectrum.

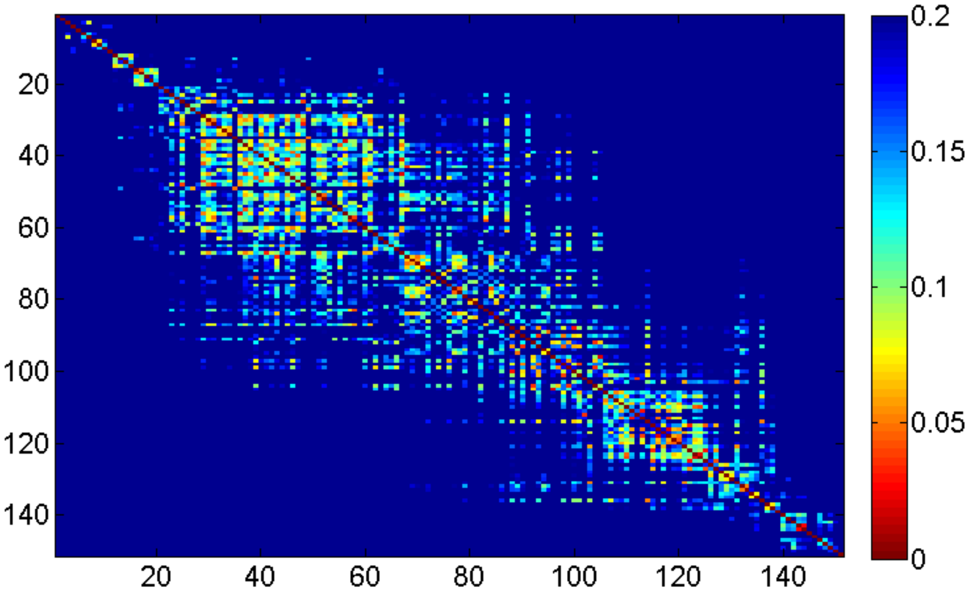

Figure 4.8.: Correlation plot of the intensity dependent study of xenon clusters. Numbers correspond to the peaks in table 4.3. The closer to 0, the better the correlation.

two peaks are correlated if their corresponding value in the correlation matrix is close to 0. Such cases are easily seen in figure 4.8. To determine if three peaks, called 1, 2 and 3 for simplicity, are correlated, however, it is not sufficient to check in row 1 if the values for correlation of 1 and 2 and 1 and 3 are close to 0. The value for correlation of 2 and 3 (in row 2) also has to be close to 0. These cases are not easily found by eye and get increasingly difficult to spot as the number of correlated peaks increases.

In fact, even to solve this problem computationally is highly demanding. The computer employed for the calculations was not able to compute the solution analytically. Therefore, an approximate solution has to be used. (Computationally, this problem is equivalent to the so-called *maximum clique problem*. The MATLAB subroutine which I implemented to solve the problem was written by J. Wildman and can be freely downloaded [92]. It is based on the papers by Bron and Kerbosch [93] and Cazals and Karande [94]).

The method described above was used to determine the charge state of unknown spectral lines in the following way. The threshold, which determines which values are accepted as correlated, was chosen iteratively in such a way that there were no contradictions to the previous charge state assignment. When compartments were created which contained more than one charge state, the threshold was further reduced until these compartments were either split up or gone altogether. The remaining compartments were checked to see if unknown lines evolve similarly to lines with an assigned charge state. If so, the according charge state was assigned.

In this way, charges states have been assigned to 38 lines of the FEL intensity dependent study of xenon which could not be identified by the previous method. These charge states are marked in red in table 4.3. About 1/5 of the total number of fluorescence lines remain unassigned.

Distribution of charge states

Having assigned a charge state to over 80 % of the spectral lines of xenon, it is possible to determine the charge state distribution in dependence on the FEL intensity. For this analysis, the spectrometer efficiency, consisting of the wavelength dependent grating efficiency and quantum efficiency of the detector, has to be taken into account.

The big advantage of analyzing the charge state distribution via fluorescence is that fluorescence signal from all stages of the interaction is integrated, thereby in principle giving information on the fast (sub-ps) charge state formation. This information is not represented in TOF spectra, because a TOF detects ions which are present microseconds after the interaction. However, it is important to note that the charge state distribution derived from a fluorescence spectrum is not as complete as one recorded with a TOF. In principle, a TOF can collect all ions present at the end of the interaction. Our fluorescence spectrometer, on the other hand, only detects a spectral window of all fluorescing states[5]. Furthermore, different states do not necessarily have the same probability of decaying via fluorescence. Some states may also decay alternatively via Auger decay, while for other states the released energy may not be sufficient to emit an electron, leaving fluorescence as the only viable decay channel.

For these reasons, the ratio between different charge states seen in the spectra might not accurately portray the real initial charge state distribution. Therefore, the following analysis is based on relative changes of the charge distribution depending on the FEL intensity, which is more reliable than absolute statements about, for instance, the mean charge state.

For plotting the distribution of charge states, one additional normalization step is necessary, because in the FEL intensity scan the volume of the interaction region varies, for the following reason. As was explained in chapter 3, the intensity is varied by moving the refocusing mirror. The number of photons is not reduced but merely spread out over a larger interaction volume. Provided that the process under question only requires one photon[6], reducing the FEL intensity in this way does not reduce the fluorescence yield. Therefore, the signal has to be normalized with respect to the volume of the interaction region[7]. The volume at each mirror position can be calculated with the parameters introduced in chapter 3. In a Gaussian beam, the distance from the beam axis at which the intensity has dropped to $I(z)/e^2$ is given by

$$w(z) = w_0\sqrt{1+\left(\frac{z\lambda}{\pi w_0^2}\right)^2} = w_0\sqrt{1+\left(\frac{z}{z_0}\right)^2}. \tag{4.3}$$

I_z is the intensity in the beam center at a distance z along the beam axis from the focal point. The beam waist w_0 is 2.21 µm, as was calculated in chapter 3, z is the displacement of the focusing mirror and $z_0 = \pi w_0^2/\lambda$ is a constant, the so-called Rayleigh length. The volume of the interaction region can be calculated by first determining the area of the projected overlap between the FEL and the cluster beam. By rotating this area about the FEL axis by 180 °, one gets the volume. The shaded area (half of the overlap area) in figure 4.9 can be calculated by

---

[5] Xenon fluorescence could be observed *by eye*. This is clear proof that more fluorescing states than the ones to which the spectrometer is sensitive were excited.

[6] and that the FEL beam is not expanded so much that its cross section is no longer entirely contained within the cluster beam

[7] Strictly speaking, this normalization would have had to be applied before the assignment of charge states. However, the effect would have been an enhancement of high FEL intensities relative to low FEL intensities, thereby reducing the variety of FEL intensities which maximize specific spectral lines. In effect, the assignment method for the charge states would have been less specific. The method employed in chapter 4.2.1 is not affected by this normalization. The ratios between the intensities of the spectra are modified by constant factors. In essence, spectral lines which evolve similarly before the normalization also evolve similarly after the normalization.

integrating $w(z)$.

$$\int_{z_1}^{z_2} w(z)\,dz = w_0 \int_{z_1}^{z_2} \sqrt{1+\left(\frac{z}{z_0}\right)^2}\,dz \tag{4.4}$$
$$= \frac{1}{2} w_0 z_0 \left[\frac{z}{z_0}\sqrt{1+\left(\frac{z}{z_0}\right)^2} + \operatorname{arcsinh}\left(\frac{z}{z_0}\right) \right]_{z_1}^{z_2}$$

The cluster beam expands as it travels from the cluster source, so it would seem that the surface area shown in figure 4.9 should not have parallel sides. The reason is that we select a narrow slice along the cluster beam axis during the evaluation of the spectra, as can be seen in figure 4.1. The slice has the same height of 48 pixels or 648 μm regardless of mirror position, therefore the distance between z_1 and z_2 is constant for all spectra.

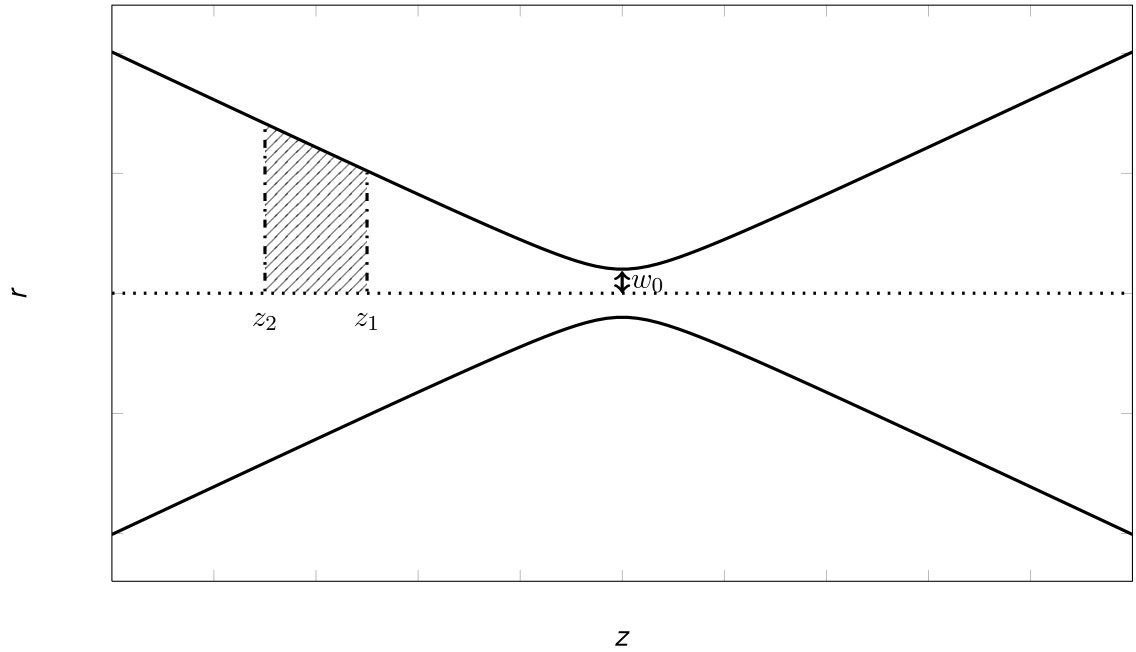

Figure 4.9.: Schematic cross section of a focused Gaussian beam. The shaded area is calculated in equation 4.4 in order to compute the change of the interaction volume (see table 4.4).

Calculating the area for the values used in the FEL intensity dependent study on xenon clusters shows that it is very close to the area of a rectangle with width $z_2 - z_1$ and a height equal to formula 4.3 evaluated at $\frac{z_2+z_1}{2}$. The values are given in table 4.4. Even at the beam waist, the error is below 1.5%. As it is much easier to calculate the volume resulting from the rectangle, a cylinder after rotation, these values are used. The resulting volume is called V_{approx} in table 4.4. By dividing the yield at each intensity position by the corresponding volume, the effect of the expanding interaction region is properly taken into account. The result of the corrected focus volume effect can be seen in figure 4.10. The plot shows the distribution of Xe charge states in dependence on FEL intensity. Clearly, Xe^{5+} exhibits the highest yield of any charge state for each FEL intensity. Regarding the dependence on FEL intensity, individual charge states seem to show one of three general behaviors: the yield of Xe^{1+} and Xe^{2+} increases from low to medium FEL intensity but then reaches a plateau and does not not increase further for higher FEL intensities. The yield of Xe^{3+}, Xe^{4+} and Xe^{5+} also increases from low to medium FEL intensities, but it decreases again after having reached a maximum. The yield of Xe^{8+} and higher charge states increases with increasing FEL intensity throughout the entire intensity range. Xe^{6+} and Xe^{7+} are in-between these two last cases, appearing to be on the verge of

z (μm)	FEL peak intensity ($10^{15}\,$W/cm^2)	A_{exact} (μm^2)	A_{approx} (μm^2)	$\frac{A_{\text{exact}}}{A_{\text{approx}}}$	V_{approx} (μm^3)
0	2.45	1451.2	1432.1	1.0134	9942.8
125	2.42	1459.6	1440.7	1.0131	10063
187.5	2.38	1469.9	1451.4	1.0127	10213
250	2.34	1484.2	1466.3	1.0122	10424
375	2.21	1524.5	1508	1.011	11025
625	1.88	1647.4	1634.3	1.008	12949
750	1.71	1727.1	1715.8	1.0066	14272
875	1.54	1817	1807.3	1.0054	15836
1000	1.38	1915.7	1907.5	1.0043	17640
1125	1.24	2022	2015	1.0035	19684
1250	1.11	2134.7	2128.7	1.0028	21969
1375	0.99	2252.8	2247.7	1.0023	24495
1500	0.89	2375.6	2371.3	1.0018	27261
1625	0.8	2502.3	2498.6	1.0015	30267
2125	0.54	3038.5	3036.4	1.0007	44699
2625	0.39	3605.4	3604.2	1.0003	62978
3625	0.22	4787.2	4786.7	1.0001	111083
5125	0.11	6614.5	6614.3	1	212103
7625	0.05	9713.6	9713.6	1	457437

Table 4.4.: Results for the focus volume correction factor V_{approx} for each mirror position z in the FEL-intensity dependent study of Xe. The second column gives the FEL peak intensity at each mirror position. A_{exact} and A_{approx} are intermediate results for the surface area shown in figure 4.9 and described above. $\frac{A_{\text{exact}}}{A_{\text{approx}}}$ gives the relative error of the approximate result compared to the exact result.

decreasing again if the FEL intensity could have been increased further. Black lines in figure 4.10 mimic the general slope of the bar plots. They are intended as a guide to the eye in judging the dependence on FEL intensity of each charge state.

It can also be seen that for those charge states which exhibit a clear maximum yield at a certain FEL intensity, this FEL intensity shifts to higher values from low to high charge states: the Xe^{3+} yield is maximized at $1.2 \cdot 10^{15}\,$W/cm^2, whereas the Xe^{6+} yield peaks at $1.7 \cdot 10^{15}\,$W/cm^2 and the Xe^{8+} yield peaks at $2.5 \cdot 10^{15}\,$W/cm^2.

Of the three behaviors with FEL intensity described above, the two extreme cases can be explained qualitatively rather easily. On the one hand, the generation of the highest charge states requires simultaneous absorption of multiple photons. Thus, higher intensity leads to higher yields. On the other hand, the formation of low charge states (q=1,2) proceeds via single photon absorption. Increasing the intensity provides more photons, thereby increasing the yield. Saturation occurs once the intensity becomes so high that higher charge states are formed on the beam axis, while outer regions of the FEL beam at lower intensity still contribute to the formation of low charge states. However, the rise and fall of the signal observed for Xe^{3+}, Xe^{4+} and Xe^{5+} is surprising. A possible explanation could be that these charge states, starting at a certain intensity, are depleted in order to produce even higher charge states in a stepwise process.

As can be seen in equation 2.9, an important piece of information about the yield of a charge state is to which power of the light intensity it is proportional. The proportionality reveals how many photons need to be absorbed simultaneously for the formation of a charge state, i.e. it reveals the order of the underlying multiphoton process. It is easily seen in a double-logarithmic version of figure 4.10. In this representation, all power laws form straight lines of different slopes. Such a plot is shown in figure 4.11. It provides interesting information. First of all,

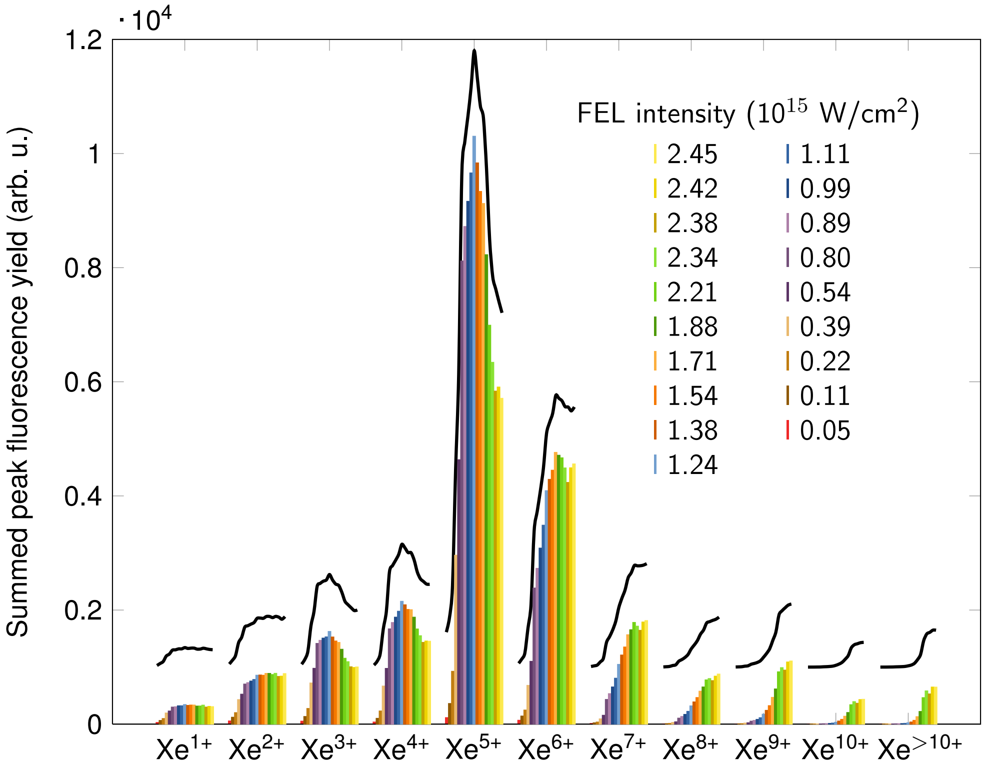

Figure 4.10.: Distribution of Xe charge states from clusters with an average size of 6700 atoms in dependence on FEL intensity. The line plots above the bar plots mimic the general slope of the bar plots and are meant as a visual aid in judging the dependence on FEL intensity of each charge state. Spectral lines which could not be unambiguously assigned to a charge state (see table 4.3) were not considered.

the formation of Xe^{1+} and Xe^{2+} exhibits a slope of 1 at low FEL intensities, as expected for a single-photon process. Xe^{3+}, Xe^{4+} and Xe^{5+} all show a slope larger than 1 and smaller than 2. The slope is greatest for Xe^{5+} and smallest for Xe^{3+}. A slope larger than 1 suggests that already at these relatively low FEL intensities their production is not exclusively due to single-photon processes. As was shown in chapter 2.4, there are cluster effects, for instance electron impact ionization and plasma heating by the excess energy of quasi-free electrons, which could play a role here. Xe^{6+} shows a behavior which is similar to Xe^{3+} to Xe^{5+} but shifted to higher FEL intensities. At the point where the decrease in yield, observed in Xe^{3+} to Xe^{5+}, might start, the highest FEL intensity is reached. For higher charge states, the trend observed in Xe^{6+} continues: the increase in yield of Xe^{7+} starts a little later than for Xe^{6+} but it also exhibits a slightly steeper slope. The slope of Xe^{8+} is steeper than the slope of Xe^{7+}, the slope of Xe^{9+} is steeper still, and so on, with $Xe^{>10+}$ having the steepest slope of all. The FEL intensity at which a charge state is first formed also shifts to higher values for higher charge states.

This behavior clearly shows the onset of nonlinear processes, which seem to play a role even at low charge states which could be reached by sequential single-photon absorption. The origin of this phenomenon will be discussed in more detail in chapter 4.3.1, after the argon spectra have been analyzed in the same way.

More theoretical work is required to pinpoint details of the energy deposition process. In particular the role of the giant resonance in the simultaneous absorption of many photons needs to be further investigated both theoretically and experimentally.

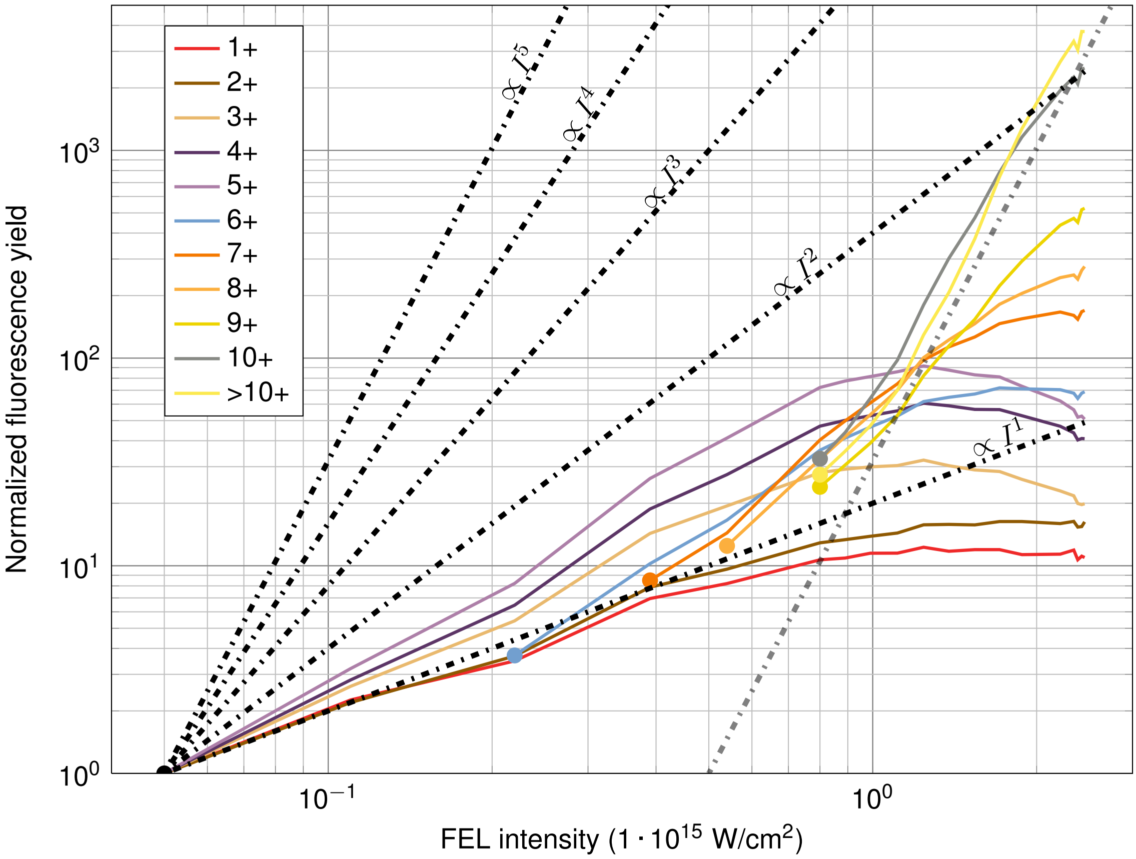

Figure 4.11.: The data shown in figure 4.10 in a double-logarithmic plot: Distribution of Xe charge states from clusters with an average size of 6700 atoms in dependence on FEL intensity. The value at the lowest FEL intensity was normalized to 1 for each charge state. Colored dots indicate the minimum FEL intensity required to generate a certain charge state. For comparison different power laws are given (the grey line also shows a slope $\propto I^5$, shifted to the right for easier comparison with high charge states at high FEL intensities.).

4.2.2. Comparison with ion time-of-flight spectra

As was explained in the introduction, an important aspect of the experiments was to gain insight into the transient charge states created during the interaction of strong XUV FEL pulses with the cluster.

Therefore, the results from fluorescence spectroscopy are compared with previously published works by Thomas et al. [20], whose experimental conditions were very close to ours. Thomas et al. [20] report charge states up to Xe^{9+} in atomic spectra at an FEL intensity of $5 \cdot 10^{14}$ W/cm^2. These results are in good agreement with measurements by Sorokin et al. [46]. For clusters, a direct identification of the highest charge states proved difficult for Thomas et al. because the kinetic energy of the ions broadens the peaks in the TOF, resulting in overlapping, indistinguishable peaks. They could, however, deduce a maximum charge state of Xe^{10+} by modeling the measured kinetic energy distribution of the ions resulting from a combination of Coulomb explosion and hydrodynamic expansion of clusters. From their measurements one can conclude that the difference in the formation of high charge states comparing atomic and cluster targets is rather small.

In our fluorescence experiments, Xe^{8+} is the highest charge state found in clusters at an intensity of $5.4 \cdot 10^{14}$ W/cm^2. This can be seen in figure 4.7. Given the uncertainty in the calculation of the FEL intensity, this result is in reasonable agreement with the results of Thomas et al. and Sorokin et al..

4.3. Argon clusters

Apart from the experiments on pure xenon clusters, we also performed very similar experiments on pure argon clusters. Spectra were recorded at varying FEL intensity and cluster size, respectively. The evaluation process is very similar to the one established for xenon clusters in chapter 4.2. Again, the first step is to identify the fluorescing charge states.

4.3.1. Identifying charge states

As in the case of xenon, one first analyses the evolution of the spectral lines in dependence on the FEL intensity. All the spectra stem from clusters with an average size of about 400 atoms, generated at a pressure of 6.7 bar. The exposure time for each spectrum was 2 minutes, which is equivalent to 1200 FEL shots.

Dependence of argon charge states on FEL intensity

The procedure of generating line plots from the raw fluorescence spectra was described at the beginning of chapter 4. In the following analysis, changes in the relative abundance of different charge states are measured as a function of FEL intensity. In the case of FEL intensity dependent study of argon clusters, however, there was a significant change in FEL pulse energy during the scan. The highest average pulse energy during the intensity dependent study of argon clusters was 134 µJ, the lowest was 94 µJ, about 70% of the maximum value. As was described at the beginning of chapter 4, a change of the pulse energy during the data acquisition is partially compensated by using a linear scaling approximation, with the reservations given there. The results will have to be checked later on to find out if any unexpected features may

be attributable to the changing FEL intensity.
The normalized spectra are shown in figure 4.12. The dots at the peak positions signify which FEL intensity maximizes a certain peak. One can see that the emerging picture is not as clear as in the case of xenon. Almost all of the fluorescence lines between 10 and 40 nm peak at the highest or second highest intensity, but a comparison with the NIST Atomic Spectra database [67] shows that not all of these lines can belong to the same charge state. It turned out that an important additional criterion for the assignment of lines is the minimum FEL intensity at which a fluorescence line appears in the spectrum. This procedure allows to define groups of lines with similar appearance intensities which are consistent with the tabulated lines in the NIST database. The results can be seen in table 4.5.
Note that for argon two methods (correlation plot and maximum line strength) do not give unambiguous assignments. One reason is that in argon an intensity range similar to the one used for xenon generates a significantly smaller variety of charge states. In argon, we observe charge states between 1 and 7, in xenon, we observe charge states between 1 and at least 11. This means that in argon the dependence on FEL intensity is not as pronounced as in xenon. This is expected because of the significantly lower absorption cross section of argon. Consequently, relative changes between charge states of argon, contrast in general and changes in the evolution of fluorescence lines are not as pronounced as in the case of xenon. The appearance intensity, however, remains a useful criterion.
About 74 % of all fluorescing lines of argon could be assigned in this manner, only slightly less than in xenon. Based on this assignment, the next section will deal with the overall charge distribution depending on the FEL intensity.

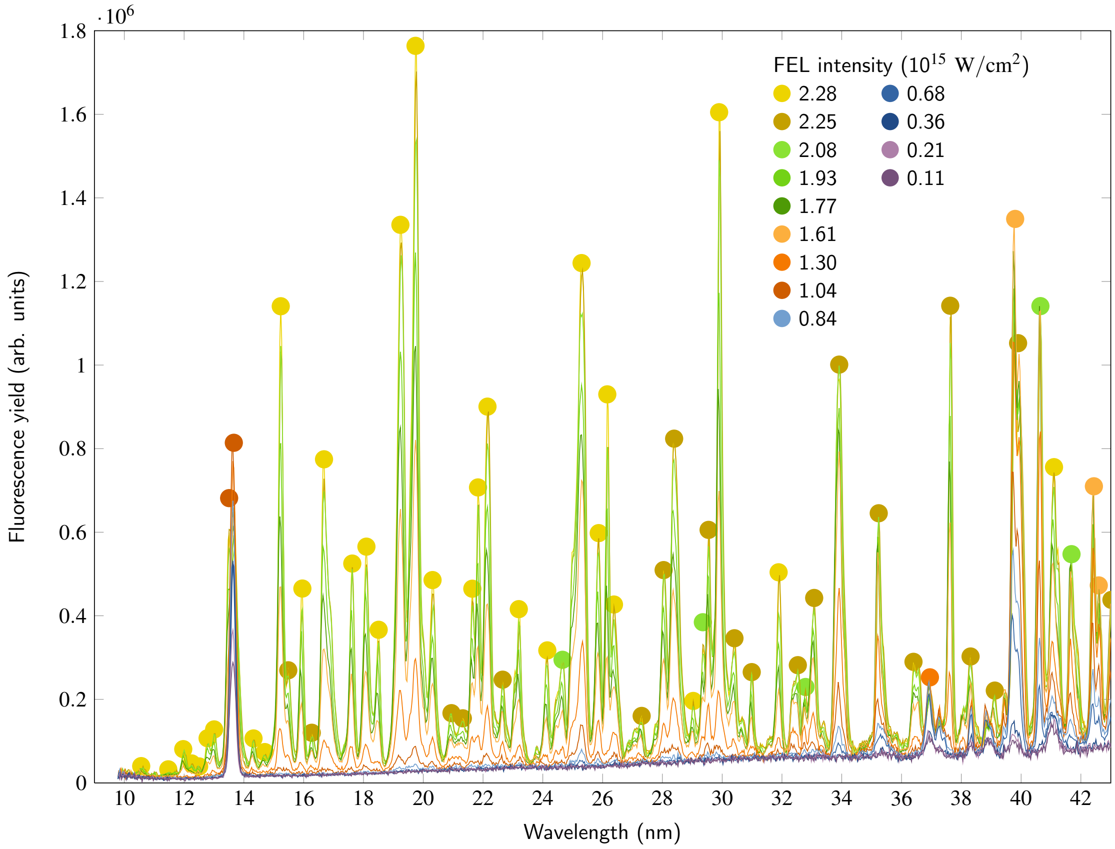

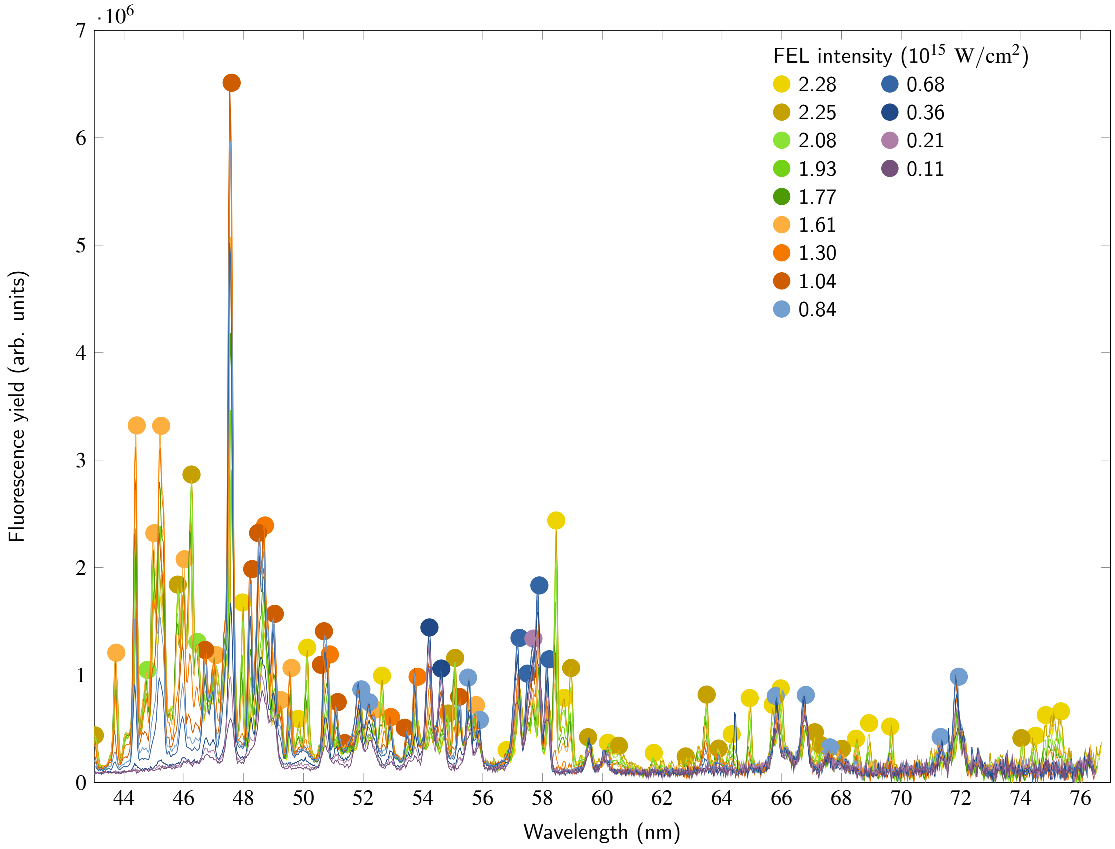

Figure 4.12.: Evolution of fluorescence yield in dependence on FEL intensity from argon clusters with an average size of about 400 atoms. Colored circles indicate the intensity at which the respective peak reaches its maximum. Note the different intensity scales of the two plots.

Measured (nm)	NIST (nm)	Transition (Configuration, Term, J)	Charge state	Color code
10.6	10.608	$2p^6 10d$, ^2D, $5/2$ - $2p^6 3p$, $^2P^o$, $3/2$	7+	●
12.0	12.008	$2p^6 5p$, $^2P^o$, $3/2$ - $2p^6 3s$, ^2S, $1/2$	7+	●
12.3	12.303	$2p^6 6d$, ^2D, $5/2$ - $2p^6 3p$, $^2P^o$, $3/2$	7+	●
12.5	12.507	$3s8d$, ^3D, 3 - $3s3p$, $^3P^o$, 2	6+	●
12.8	12.81	$2p^6 6s$, ^2S, $1/2$ - $2p^6 3p$, $^2P^o$, $3/2$	7+	●
13.0	13.019	$3s7d$, ^3D, 2 - $3s3p$, $^3P^o$, 1	6+	●
13.5	13.48	$3s5p$, $^1P^o$, 1 - $2p^6 3s^2$, ^1S, 0	6+	●
13.7	FEL stray			●
14.3	14.319	$3s6s$, ^3S, 1 - $3s3p$, $^3P^o$, 2	6+	●
14.7	14.691	$2p^6 7f$, $^2F^o$, $7/2$ - $2p^6 3d$, ^2D, $5/2$	7+	●
15.2	15.226	$3s5d$, ^3D, 2 or 3 - $3s3p$, $^3P^o$, 2	6+	●
15.5	no fit			●
16	15.917	$2p^6 4p$, $^2P^o$, $1/2$ - $2p^6 3s$, ^2S, $1/2$	7+	●
16.3	16.349	$3s9f$, $^3F^o$, 4 or 3 - $3s3d$, ^3D, 3	6+	●
16.7	16.616	$3s5s$, ^3S, 1 - $3s3p$, $^3P^o$, 1	6+	●
17.6	17.616	$3s7f$, $^3F^o$, 4 - $3s3d$, ^3D, 3	6+	●
18.1	18.073	$3s^2 5d$, ^2D, $5/2$ - $3s^2 3p$, $^2P^o$, $3/2$	5+	●
18.5	18.43	$2p^6 5f$, $^2F^o$, $7/2$ - $2p^6 3d$, ^2D, $5/2$	7+	●
19.2	19.204	$3s4d$, ^3D, 2 - $3s3p$, $^3P^o$, 1	6+	●
19.7	19.771	$2p^6 10p$, $^2P^o$, $1/2$ or $3/2$ - $2p^6 4s$, ^2S, $1/2$	7+	●
20.3	no fit			●
20.9	no fit			●
21.3	no fit			●
21.6	21.525	$3s4d$, ^1D, 2 - $3s3p$, $^1P^o$, 1	6+	●
21.8	21.872	$2p^6 10d$, ^2D, $3/2$ - $2p^6 4p$, $^2P^o$, $1/2$	7+	●
22.1	22.174	$2p^6 10s$, ^2S, $1/2$ - $2p^6 4p$, $^2P^o$, $1/2$	7+	●
22.7	no fit			●

23.2	23.187	$3s^23p5s$, $^3P^o$, 2 - $3s^23p^2$, ^3P, 1	4+	●
24.2	no fit			●
24.4	24.407	$3s7d$, ^3D, 2 - $3p3d$, $^3P^o$, 2	6+	●
24.7	no fit			●
25.3	25.267	$3s^23p4d$, $^3D^o$, 3 - $3s^23p^2$, ^3P, 2	4+	●
25.9	no fit			●
26.2	no fit			●
26.4	no fit			●
27.3	unknown			●
28	27.918	$3s4s$, ^1S, 0 - $3s3p$, $^1P^o$, 1	6+	●
28.4	28.354	$3s3p(^3P^o)4s$, $^4P^o$, 3/2 - $3s3p^2$, ^4P, 5/2	5+	●
29	no fit			●
29.4	no fit			●
29.5	no fit			●
29.9	unknown			●
30.4	unknown			●
31	unknown			●
31.9	31.665(obs. 31.8)		7+	●
32.5	32.615		5+	●
32.8	32.807	$3s7s$, ^3S, 1 - $3s4p$, $^3P^o$, 2	6+	●
33.1	unknown			●
33.9	33.902	$3s^23p4s$, $^3P^o$, 0 - $3s^23p^2$, ^3P, 1	4+	●
35.2	unknown			●
36.4	36.404	$2p^612d$, ^2D, 5/2 - $2p^65p$, $^2P^o$, 3/2	7+	●
36.6	36.436	$2p^610p$, $^2P^o$, 1/2 - $2p^65s$, ^2S, 1/2	7+	●
36.9	36.831	$3s^23p^3(^2D^o)4d$, $^3P^o$, 2 - $3s^23p^4$, ^3P, 2	2+	●
37.6	unknown			●
38.3	38.261	$3s^23p^3(^2P^o)4d$, $^1F^o$, 3 - $3s^23p^4$, ^1D, 2	2+	●
39.1	39.016	$2p^65p$, $^2P^o$, 1/2 - $2p^64s$, ^2S, 1/2	7+	●
39.8	39.688	$3s^23p^2(^3P)4s$, ^4P, 5/2 - $3s^23p^3$, $^4S^o$, 3/2	3+	●
39.9	39.856	$3s^23p^2(^3P)4s$, ^4P, 3/2 - $3s^23p^3$, $^4S^o$, 3/2	3+	●
40.6	40.564	$3s^23p^2(^1D)4s$, ^2D, 5/2 - $3s^23p^3$, $^2D^o$, 5/2	3+	●
41.1	41.009	$3s3p(^1P^o)3d$, $^2F^o$, 7/2 - $3s3p^2$, ^2D, 5/2	5+	●

41.2	41.102	$3s^23p3d$, $^1F^o$, 3 - $3s^23p^2$, ^3P, 2	4+	●
41.7	41.706	$3s4p$, $^3P^o$, 0 - $3s3d$, ^3D, 1	6+	●
42.4	42.351	$3s^23p^2(^3P)4s$, ^2P, 3/2 - $3s^23p^3$, $^2D^o$, 5/2	3+	●
42.6	42.554	$3s^23p^2(^3P)4s$, ^2P, 1/2 - $3s^23p^3$, $^2D^o$, 3/2	3+	●
43	42.969	$3s^23p^2(^1D)4s$, ^2D, 5/2 or 3/2 - $3s^23p^3$, $^2P^o$, 3/2	3+	●
43.7	43.663	$3s^23p3d$, $^1F^o$, 3 - $3s^23p^2$, ^1D, 2	4+	●
44.4	44.364	$3s^23p^2(^3P)3d$, ^2F, 5/2 - $3s^23p^3$, $^2D^o$, 5/2	3+	●
44.8	44.752	$3s^23p3d$, $^3D^o$, 1 - $3s^23p^2$, ^3P, 1	4+	●
45	44.95	$3s^23p3d$, $^3D^o$, 2 - $3s^23p^2$, ^3P, 2	4+	●
45.2	45.201	$3s^23p^2(^3P)4s$, ^2P, 1/2 - $3s^23p^3$, $^2P^o$, 1/2	3+	●
45.8	45.805	$3s3p(^3D^o)3d$, $^4D^o$, 1/2 - $3s3p^2$, ^4P, 3/2	5+	●
46	45.987	$3s^23p^2(^1D)3d$, ^2D, 5/2 - $3s^23p^3$, $^2D^o$, 5/2	3+	●
46.3	46.28	$3d^2$, ^1D, 2 - $3p3d$, $^1D^o$, 2	6+	●
46.5	46.427	$3s3p(^3P^o)3d$, $^4P^o$, 5/2 - $3s3p^2$, ^4P, 3/2	5+	●
46.7	46.74	$3s^23p^3(^2D^o)3d$, $^3P^o$, 2 - $3s^23p^4$, ^3P, 2	2+	●
47	46.99	$3s^23p^3(^2D^o)3d$, $^3P^o$, $1, 2, \text{resp.}$ - $3s^23p^4$, ^3P, $0, 1, \text{resp.}$	2+	●
47.1	overlain			●
47.4	47.393	$3s3d$, ^3D, 1 - $3s3p$, $^3P^o$, 0	6+	●
47.6	47.64323	$3s^23p^3(^2P^o)3d$, $^3D^o$, 2 - $3s^23p^4$, ^3P, 1	2+	●
48	47.935	$3s3d$, ^3D, 3 - $3s3p$, $^3P^o$, 2	6+	●
48.3	48.255	$3s^23p^3(^2P^o)4s$, $^3P^o$, 2 - $3s^23p^4$, ^3P, 2	2+	●
48.5	48.515	$3s^23p^3(^2P^o)4s$, $^3P^o$, 2 - $3s^23p^4$, ^3P, 1	2+	●
48.7	48.703	$3s^23p^3(^2D^o)3d$, $^1D^o$, 2 - $3s^23p^4$, ^1D, 2	2+ (1+ underl.)	●
49	49.023	$3s^23p^3(^2P^o)3d$, $^1P^o$, 1 - $3s^23p^4$, ^1S, 0	2+	●
49.2	49.252	$3p3d$ $^3P^o$ 1 - $3p^2$, ^3P, 0	6+	●

49.6	49.57	$3s3p^4$, ^2P, 3/2 - $3s^23p^3$, $^2D^o$, 5/2	3+	●
49.8	no fit			●
50.1	50.107	$3s3d$ ^1D 2 - $3s3p$, $^1P^o$, 1	6+	●
50.7	50.748	$3s^23p^3(^2P^o)4s$, $^1P^o$, 1 - $3s^23p^4$, ^1D, 2	2+	●
50.9	blended lines		5+,6+	●
51.1	51.15	$3s^23p^3(^2D^o)4s$, $^3D^o$, 2 - $3s^23p^4$, ^3P, 1	2+	●
51.9	51.89	$3s^23p^4(^3P)4d$, ^2D, 3/2 - $3s^23p^5$, $^2P^o$, 3/2	1+	●
52.2	52.279	$3s^23p^4(^3P)4d$, ^2D, 3/2 - $3s^23p^5$, $^2P^o$, 1/2	1+	●
52.4	52.433	$3s^23p^3(^2D^o)3d$, $^3S^o$, 1 - $3s^23p^4$, ^1D, 2	2+	●
52.6	52.659	$3s^23p^2(^3P)3d$, ^2D, 3/2 - $3s^23p^3$, $^2P^o$, 1/2	3+	●
52.9	52.99	$3s^23p^3(^2D^o)3d$, $^3D^o$, 3 - $3s^23p^4$, ^3P, 2	2+	●
53.8	53.746	$3s^23p^3(^2D^o)3d$, $^3D^o$, 1 - $3s^23p^4$, ^3P, 1	2+	●
54.2	54.291	$3s^23p^4(^3P)4s$, ^4D, 1/2 - $3s^23p^5$, $^2P^o$, 3/2	1+	●
54.6	54.618	$3p^4$, ^1S, 0 - $3s3p^3$, $^3P^o$, 1	1+	●
54.8	no fit			●
55.1	55.136	$3s3p^2$, ^2P, 3/2 - $3s^23p$, $^2P^o$, 3/2	5+	●
55.2	55.224	$3s^23p^3(^2D^o)3d$, $^3P^o$, 1 - $3s^23p^4$, ^1S, 0	2+	●
55.5	55.577	$3s^23p^4(^1S)3d$, ^2D, 3/2 - $3s^23p^5$, $^2P^o$, 3/2	1+	●
55.8	no fit			●
55.9	no fit			●
57.2	57.201	$3s^23p^4(^1D)3d$, ^2P, 1/2 - $3s^23p^5$, $^2P^o$, 3/2	1+	●
57.5	57.412	$3s^23p^2(^3P)4p$, $^4S^o$, 3/2 - $3s^23p^3$, ^4P, 5/2	3+	●
57.7	57.674	$3s^23p^4(^1D)3d$, ^2P, 1/2 - $3s^23p^5$, $^2P^o$, 1/2	1+	●
57.9	57.811	$3s^23p^4(^1D)3d$, ^2P, 3/2 - $3s^23p^5$, $^2P^o$, 1/2	1+	●
58.2	58.229	$3s^23p^2(^3P)4p$, $^2D^o$, 3/2 - $3s3p^4$, ^4P, 3/2	3+	●
58.5	58.446	$2p^68f$, $^2F^o$, 7/2 - $2p^65g$, ^2G, 9/2	7+	●
58.7	58.701	$3p^3$, $^4S^o$, 3/2 - $3s3p^2$, ^4P, 1/2	5+	●
59	58.978	$3p^3$, $^4S^o$, 3/2 - $3s3p^2$, ^4P, 3/2	5+	●

59.5	no fit			●
60.6	60.728 - 60.454	$3p5s$, $^{3}P^{\mathrm{o}}$, 1 - $3p4p$, ^{3}D, 2 or 1	6+	●
63.5	63.515	$3s3p^{3}$, $^{1}P^{\mathrm{o}}$, 1 - $3s^{2}3p^{2}$, ^{1}S, 0	4+	●
63.9				●
64.3	no fit			●
64.9	no fit			●
65.7	65.712	$3d^{2}$, ^{3}P, 0 - $3p3d$, $^{1}P^{\mathrm{o}}$, 1	6+	●
65.8	no fit			●
66	65.982 - 66.081		6+	●
66.8	66.756	$3s^{2}3p^{2}(^{3}P)4p$, $^{2}P^{\mathrm{o}}$, $3/2$ - $3s3p^{4}$, ^{2}D, $5/2$	3+	●
67.1	no fit			●
68.5	no fit			●
68.9	no fit			●
69.6	69.705	$3p4p$, ^{3}S, 1 - $3s4p$, $^{3}P^{\mathrm{o}}$, 2	6+	●
71.9	71.809	$3s^{2}3p^{4}(^{3}P)4s$, ^{2}P, $1/2$ - $3s^{2}3p^{5}$, $^{2}P^{\mathrm{o}}$, $3/2$	1+	●

Table 4.5.: Argon: Comparison of measured wavelengths with tabulated values from the NIST database [67]. The 2nd, 3rd and 4th columns are taken from the NIST database. The color code gives the FEL intensity which maximizes the peak as seen in figure 4.12.

Distribution of charge states

To determine the charge distribution in dependence on the FEL intensity, the peak values of all spectral lines assigned to a certain charge state were summed, separately for each spectrum, corresponding to a different FEL intensity. The spectra were normalized to correct the influence of the interaction volume, as was previously done for xenon. The result is shown in 4.13. A striking difference between the intensity dependent studies of Ar and Xe clusters (see figure 4.10) is that for argon we observe a bimodal charge state distribution. At lower intensity, Ar^{2+} dominates the spectrum whereas at high intensity Ar^{3+} and Ar^{6+} provide the highest yield. As discussed in chapter 4.2.1, fluorescence of Xe^{5+} was dominant for all intensities available in the present study ($5 \cdot 10^{13}$ W/cm^2 - $2.5 \cdot 10^{15}$ W/cm^2).

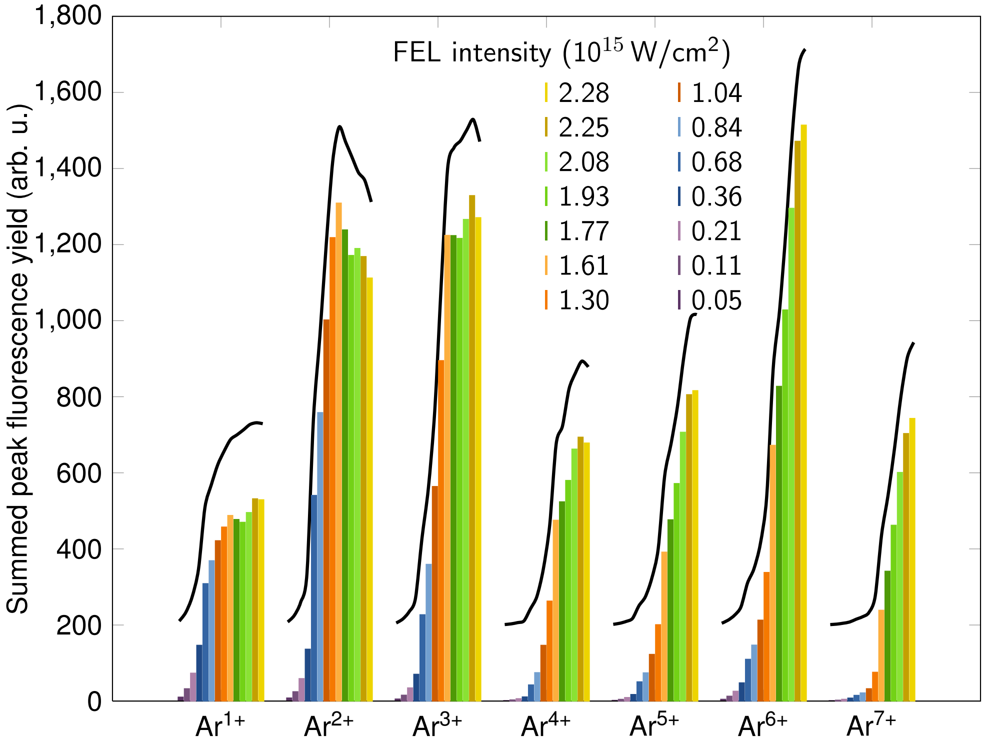

Figure 4.13.: Distribution of Ar charge states from clusters with an average size of 400 atoms in dependence on FEL intensity. The line plots above the bar plots mimic the general slope of the bar plots and are meant as a visual aid in judging the dependence on FEL intensity of each charge state. Spectral lines which could not be unambiguously assigned to a charge state (see table 4.5) were not considered.

A predominance of lower charge states than in xenon at comparable FEL intensities is expected because of the significantly lower cross section of argon. The lower cross section also explains why the maximum charge state in argon (7+) is significantly lower than for xenon (at least 11+). The higher ionization potential of argon also plays a role. However, as already pointed out in the previous discussion, one has to be careful with the interpretation of the charge state distribution. The same reservations which were mentioned in the analysis of xenon apply: because we do not observe the entire range of fluorescence photons and because different states may have varying probabilities of decaying via fluorescence, we do not necessarily record a true image of the ratio between charge states generated in the interaction of FEL photons with clusters. Still, relative information from intensity dependent fluorescence yields should provide important insight into the mechanism of energy deposition and energy redistribution.

Figure 4.14 shows the normalized fluorescence yield of charge states as a function of FEL intensity in a double-logarithmic representation. It shows that the fluorescence yield of Ar^{1+} is close

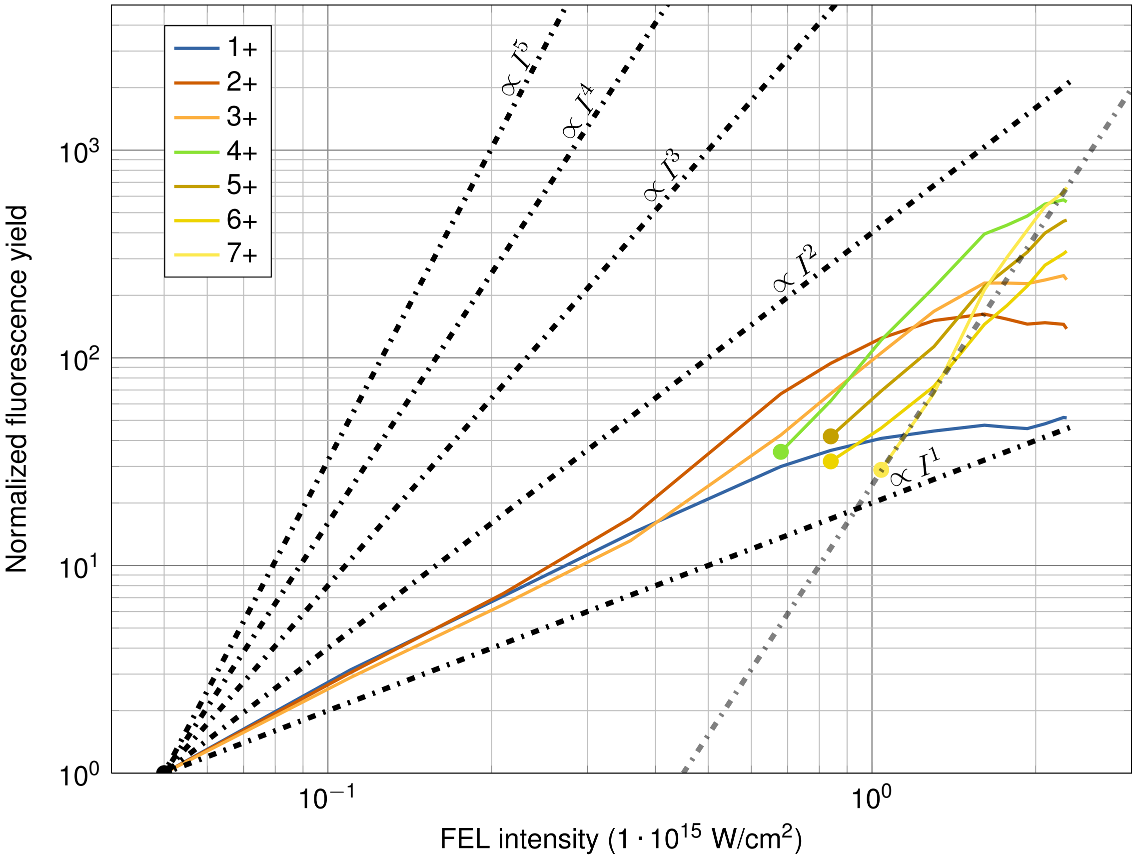

Figure 4.14.: The data shown in figure 4.13 in a double-logarithmic plot: Distribution of Ar charge states from clusters with an average size of 400 atoms in dependence on FEL intensity. The value at the lowest FEL intensity was normalized to 1 for each charge state. Colored dots indicate the minimum FEL intensity required to generate a certain charge state. For comparison different power laws are given (the grey line also shows a slope $\propto I^4$, shifted to the right for easier comparison with high charge states at high FEL intensities.).

to saturation. Interestingly, Ar^{2+} shows the decrease in yield at high FEL intensities which was observed for Xe^{3+}, Xe^{4+} and Xe^{5+}, indicating a stepwise formation of the highest charge states via depletion of a particular precursor. The remaining charge states increase with increasing FEL intensity.

From the slopes in the log-log plot shown in figure 4.14 information on the number of simultaneously absorbed photons can be derived. The most surprising observation is that all charge states exhibit a slope larger than 1. At least for the lowest FEL intensities, we naïvely expected to see a slope of 1, pertaining to single-photon ionization. The steeper slope shows that, in general, the formation of electronically excited species in argon requires the simultaneous absorption of more photons than needed for ionization. In other words, the outgoing electron usually does not leave behind an ion in an electronically excited state. As was mentioned in chapter 2.3, Arbeiter and Fennel [54] state that in argon at a photon energy of 90 eV ionization from the 3p-shell is the strongest ionization channel. The 3p-electron in argon is the most weakly bound electron. This means that while a single 92 eV photon is sufficient to generate a singly charged ion, it usually does not generate a singly charged ion that can emit fluorescence. In other words, it usually does not generate an ion in an electronically excited state.

This ionization behavior is in stark contrast to xenon, where the most likely ionization process is the ionization of an electron of the 4d-shell, as was discussed in chapter 2.3. One could say that at 13.5 nm, argon is ionized from the "outside" to the "inside", whereas xenon is ionized from the "middle" to the "outside". Therefore, in xenon a single photon generates a potential fluorescing state on average, whereas in argon a single photon generates a non-fluorescing state on average. This is illustrated by the slopes of Xe^{1+} and Xe^{2+} in figure 4.11, which show a slope of 1, corresponding to a single-photon process. In argon, on the other hand, even the lowest charge states exhibit slopes larger than 1, because argon needs to absorb additional energy to form a potential fluorescing state. This argument gives a qualitative explanation for the increased slopes of low argon charge states at low FEL intensities compared to xenon.

Along these lines, one may also understand the steep slope of Ar^{7+} starting at about $1 \cdot 10^{15}\,\text{W/cm}^2$. A nonlinear behavior is expected for Ar^{7+}, which is the first charge state of argon which should require the absorption of two photons to be generated even in the electronic ground state. However the slope of about 4 is steeper than expected. Drawing on the discussion above, it is plausible that the fluorescing states of Ar^{7+} require additional energy absorption (by multi-photon absorption and inelastic electron collisions) to populate electronically excited charge states, which finally fluoresce. An analogous model could be employed to explain the steep slopes observed in the highest charge states of xenon (see the discussion belonging to figure 4.11). We must keep in mind that the prerequisite for fluorescence (an excited ion) is different from the prerequisite for detection in TOF mass spectrometry (any ion, also in the ground state). Consequently, the dependence of charge states on FEL intensity is different for the two methods.

4.4. Cluster size effects

4.4.1. Total fluorescence yield of xenon and argon in dependence on cluster size

Apart from varying the FEL intensity, we also recorded studies where the cluster size was varied while the position of the refocusing mirror was kept fixed, thereby keeping the FEL intensity in the interaction region as constant as the machine performance allowed.

We recorded two scans for xenon, separated by several days, and two scans for argon, also separated by several days. In the first xenon scan, the cluster size was varied by varying the pressure from 200 to 6200 mbar, which corresponds to average cluster sizes of 2 to 6200 atoms, according to formula 2.3. The spectra were recorded at the maximum possible intensity. In the second scan, fewer pressures were used but higher pressures than in the first scan were included, resulting in larger average cluster sizes. The pressures used were 1600 mbar, 5200 mbar, 7000 mbar and 10000 mbar, corresponding to average cluster sizes of about 250, 4000, 8000 and 19000 atoms, respectively.

For argon, the first scan used pressures between 200 and 15000 mbar, but only pressures between 3000 and 15000 mbar, corresponding to average cluster sizes of about 60 to 2900 atoms, produced analyzable results, because of the following problem: the normalization with respect to the total number of atoms in the interaction volume (via the pressure, as was described at the beginning of chapter 4) causes the noise in the fluorescence spectra of small clusters, especially at long wavelengths, to be scaled up to values much higher than the signal strength measured in case of larger clusters. In other words, the signal to noise ratio measured at low stagnation pressure was not good enough to compare the recorded spectral distribution quantitatively with that recorded at high stagnation pressure. The second scan used pressures between 200 and 21000 mbar, but, again, only pressures between 2350 and 21000 mbar, corresponding to cluster sizes of about 40 to 6300 atoms, could be analyzed.

The most basic way of comparing the behavior of xenon and argon clusters is to look at the evolution of the overall fluorescence signal. Figure 4.15 shows the total fluorescence yield in the region of interest chosen in the raw spectra for each pressure (see figure 4.1). The general trend towards large cluster sizes is that the yield *decreases* both for xenon and argon[8]. It is obvious that the results of the first scans could not be exactly reproduced in the second scans. Firstly, the overall yield is higher in the second scans both for xenon and for argon. Secondly, both xenon and argon in the first scan show a clear rise in the signal from the smallest cluster to slightly larger ones. This rise is absent in the second scans. A possible explanation for this discrepancy is that in the days between the first and second scans, the gasket in the cluster valve had to be replaced. A slightly leaking gasket may have influenced the cluster generation at low pressures.In the following evaluation, only the reproducible decrease of the yield will be considered. As was explained in the beginning, the spectra have been normalized with respect to the number of atoms in the interaction region. *Therefore, if there were no cluster formation, the normalized overall fluorescence yield should not change at all with the variation of pressure.* Consequently, the plots essentially show a signal that is proportional to the yield *per atom*; any change signifies a cluster size effect.

The trend of the evolution of the cluster signal can be explained with a simple model. The model is based on two reasonable assumptions:

1. Not all atoms of the cluster emit fluorescence but only atoms from an outer shell of a certain thickness.

---

[8] We note that for the first measurement in argon there are significant dips in the signal. One of these dips can be partly explained by a simultaneous decrease of the FEL pulse energy from 117 to 100 µJ. This will be discussed in chapter 4.4.2, see figure 4.19 (a).

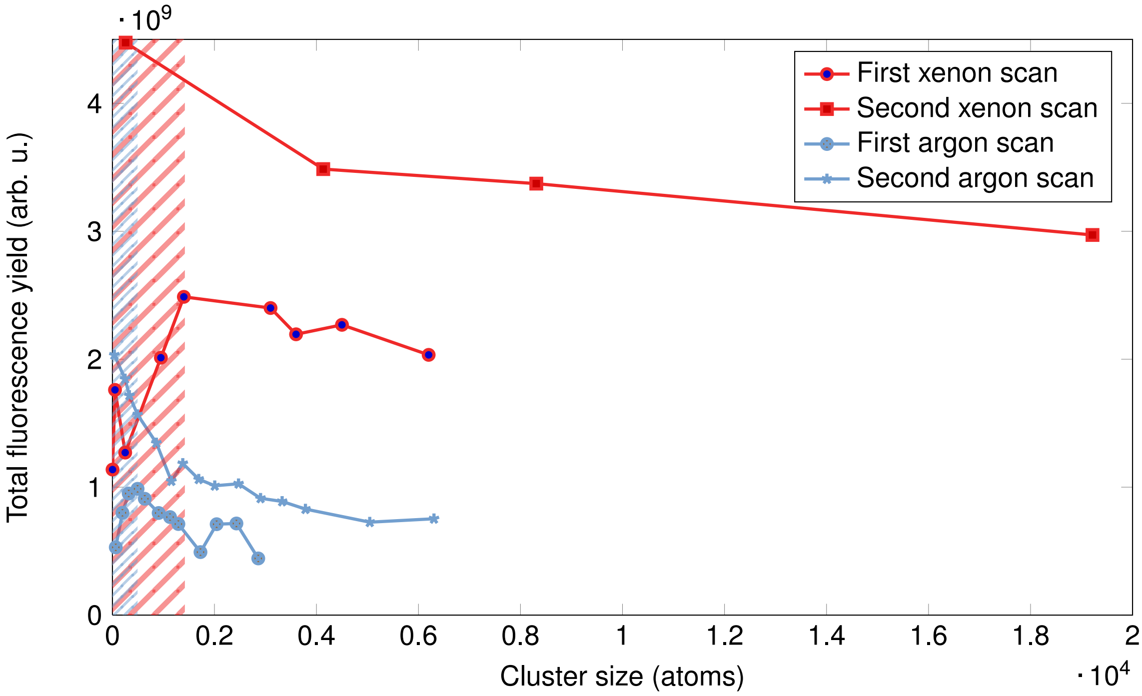

Figure 4.15.: Total fluorescence yield for argon and xenon clusters (two separate scans for each) in dependence on the cluster size. The spectra have been normalized so that the signal is proportional to a fluorescence yield per atom. The shaded areas indicate a region where there are discrepancies between the scans, both for xenon and for argon (possibly due to a gas leakage at the cluster source, see text).

2. The thickness of the fluorescing shell has to be different for xenon compared to argon.

These two points qualitatively lead to the behavior observed in figure 4.15. One simply has to take into account that the ratio of atoms in the surface layer to atoms on the inside of the cluster changes with cluster size. For the calculations, it was assumed that the cluster form icosahedra, whose number of atoms N in dependence on a number n of completely filled shells can be calculated by Mackay's formula given in equation 2.5. As was discussed, this assumption is not strictly correct for larger clusters, but since the goal of this model is only to reproduce the general trend of the recorded data, absolute precision is not required.

According to this formula, a very small cluster of 13 atoms has 12 atoms in the surface layer and just 1 atom on the inside. A cluster of 309 atoms has 162 atoms in its surface layer. A cluster of 6525 atoms has 1442 atoms in its surface layer. As the clusters become larger, the fraction of shell atoms decreases, which means that the fraction of fluorescing atoms per cluster decreases accordingly. Figure 4.16 shows the resulting curves for different thicknesses of the fluorescing shell.

Figure 4.18 shows the overall fluorescence yield[9] in dependence on the cluster size, both for xenon and argon, overlayed with the different curves from the shell model (cf figure 4.16). The non-reproducible rise at small cluster sizes was omitted from the plots. Both xenon and argon follow curves of the model reasonably well. Given the simplicity of the model, it is not surprising that the measured curves cannot be replicated exactly. The values of xenon are closest to the curve corresponding to a fluorescing shell with a thickness of 5 atom layers, whereas those of argon suggest that only a shell with a thickness of 2 atom layers contributes to the fluorescence signal.

---

[9] The Xe and Ar fluorescence yields are scaled to best match the theoretical curves. Each value of a scan is divided by a common factor. Obviously, different scans require different factors.

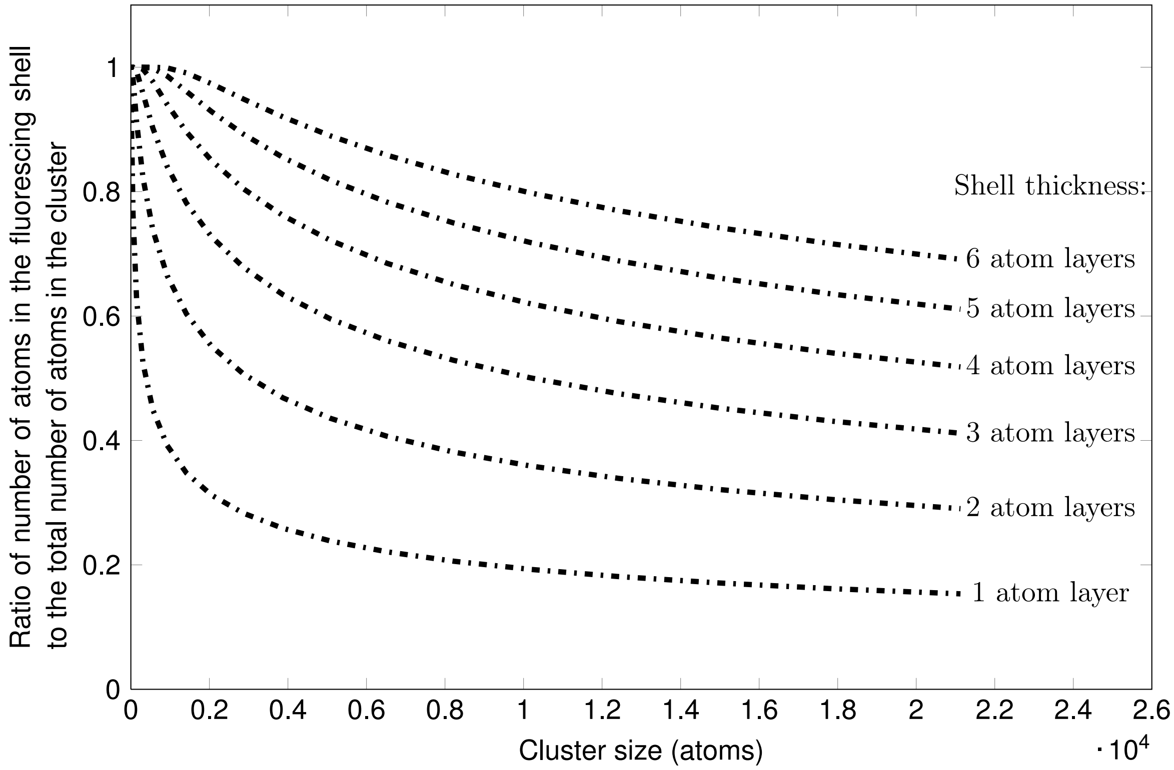

Figure 4.16.: Shell model showing the following: The effect on the overall fluorescence yield if only an outer shell of atoms emits fluorescence. The different curves correspond to different shell thicknesses. The signal is normalized with respect to the total number of atoms. Therefore, if all the atoms emitted fluorescence, the signal would stay constant for all cluster sizes.

This shell model as an explanation for the recorded data is in principle agreement with results obtained in mass spectrometry. Both Hoener et al. [9] and Thomas et al. [20] concluded from ion TOF data recorded under similar experimental conditions to ours that the cluster core is efficiently neutralized before the cluster disintegration (hydrodynamic expansion of the core and Coulomb explosion of the shell). Several theoretical works confirm a recombination of ions and electrons in the cluster core, which leads to the outer shells disintegrating by Coulomb explosion, whereas the quasi-neutral core expands hydrodynamically (see, for instance, Ziaja et al. [95], Gnodtke, Saalmann, and Rost [61]).

Apparently, non-radiative recombination is so fast in comparison to the radiative lifetime that it is also clearly visible in the fluorescence signal as a reduced fluorescence yield per atom. Thomas et al. [20] derived a thickness of the charged shell of xenon clusters with an average size between 50 and 7800 atoms by modeling the measured kinetic energy distribution of the ions with an electrostatic model. The results show a shell thickness of 3 atom layers for any cluster size, as can be seen in figure 4.17. The modeled mean charge state of the atoms in this layer drops from 2 for $\overline{N}$=50 to 0.5 for $\overline{N}$=7800. The difference of shell thicknesses derived from mass spectrometry (3 layers) and from fluorescence spectroscopy ($\approx$5 layers) could have several reasons. A straightforward explanation is the higher FEL intensity in the fluorescence experiments ($2.5 \cdot 10^{15}$ W/cm^2) compared to the mass spectroscopy experiments of Thomas et al. ($5 \cdot 10^{14}$ W/cm^2). Future FEL intensity dependent fluorescence experiments will help to clarify if a variation of the FEL intensity influences the dependence of the fluorescence yield per atom on the cluster size.

However, the difference in the number of charged, fluorescing shells might also be a sign that fluorescence spectroscopy observes a moment in time in which the recombination in the cluster core has not yet finished. Consequently, the charged outer shell of the cluster would still be thicker. The shell model identifies the origin of the decrease of the fluorescence signal towards larger clusters both for argon and xenon. However, the question remains why only a shell of atoms emits fluorescence and why this shell is thinner for argon.

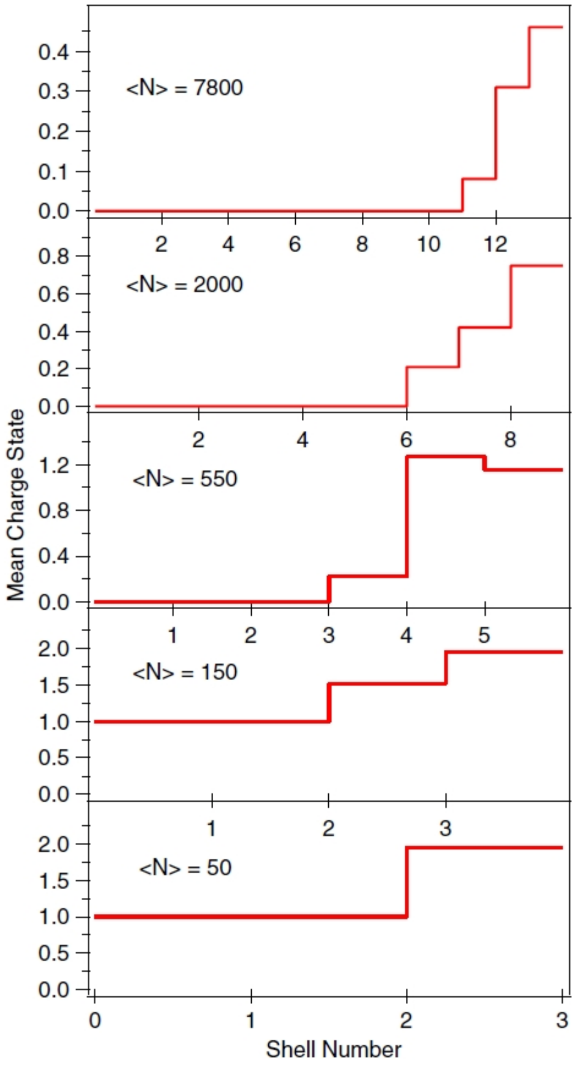

Figure 4.17.: Charge distribution of xenon clusters of various sizes (from Thomas et al. [20]). The distribution was obtained by an electrostatic model of the measured kinetic energy distribution of ions. For each cluster size, the 3 outermost shells are the only ones carrying charge.

A possible explanation is the following. As was explained in chapter 2.4.4, both xenon and argon clusters become frustrated[10] after having absorbed a certain number of photons. All further electrons can initially be only inner ionized. The radius of the nanoplasma of quasi-free electrons is given by equation 2.14 (see Saalmann [8]):

$$R_{\mathrm{el}} = \sqrt[3]{\frac{Q_{\mathrm{el}}}{Q_{\mathrm{ion}}}} R \tag{4.5}$$

---

[10] The term frustration refers to the point in the interaction at which the excess energy of photoionized electrons is no longer sufficient to overcome the overall potential formed by the ions in the cluster.

One can assume that ions decay non-radiatively by inelastic collisions with quasifree electrons before they can emit fluorescence. To explain the thicker fluorescing shells in xenon, the radius of the nanoplasma would have to be smaller in xenon.

For an equal number of atoms, the cluster radius R is very similar for xenon and argon. Ignoring secondary heating and ionization mechanisms for the moment, the ratio $Q_{\mathrm{el}}/Q_{\mathrm{ion}}$ of the total charge of quasi-free electrons to the total charge of ions in the cluster depends only on the number of ionizations that are necessary until the cluster is frustrated. This point is reached when the excess energy $(\hbar\omega_{\mathrm{las}} - E_{\mathrm{IP}})$ of the electrons is no longer sufficient to overcome the cluster potential (see chapter 2.4.4). Electrons can be ionized from many different levels, so it is impossible to give one specific excess energy for xenon and argon, respectively. However, according to Arbeiter and Fennel [54], ionization at 90 eV (13.8 nm) in argon occurs predominantly for the 3p-shell ($E_{\mathrm{IP}} = 15.76$ eV) whereas for xenon, ionization from the 4d-shell predominates. The excess energy of the photoelectron from the 4d-shell is approximately 20 eV, according to Bostedt et al. [60]; the maximum excess energy is 32 eV (Auger electron). Thus, the excess energy of the electrons ionized from xenon should on average be lower than for argon. Consequently, the cluster is frustrated after fewer ionization events and the ratio $Q_{\mathrm{el}}/Q_{\mathrm{ion}}$ is closer to 1 than for argon. Therefore, at this point in the reasoning, one would expect the nanoplasma radius[11] in xenon to be *larger* than in argon, which would lead to charged - and therefore fluorescing - shells, which are *thinner* than in argon.

However, secondary heating and ionization mechanisms were deliberately neglected so far, but in fact they play a fundamental role in the understanding of the observed difference between argon and xenon: inner ionization continues after the nanoplasma has formed. The nanoplasma thermalizes and a Maxwell-Boltzmann-distribution is formed. The hottest electrons possess enough energy to escape from the cluster, thereby reducing the number of quasi-free electrons and consequently also the radius of the nanoplasma. The process of ionization and thermalization continues. Bostedt et al. [60] measured and theoretically modelled this phenomenon for xenon clusters with an average size of 2000 atoms irradiated by 90 eV FEL pulses with intensities between $1 \cdot 10^{13}$ W/cm^2 and $5.8 \cdot 10^{14}$ W/cm^2. It is also described theoretically in detail by Gnodtke et al. [62], Arbeiter and Fennel [53] and Ziaja et al. [58].

This heating mechanism applies both to xenon and argon cluster. The difference between the two, however, lies in the fact that the cross section of xenon is about 17 times higher than that of argon (see chapter 2.3). Therefore, for xenon, frustration of the cluster occurs at a much earlier time in the FEL pulse than for argon. The remaining photons of the pulse can all contribute to the heating of the nanoplasma, which is again more efficient for xenon because the probability of ionization is higher. For xenon, many more electrons are emitted from the cluster than for argon. Therefore, the ratio of the charge of quasi-free electrons to the charge of the cluster ions, $Q_{\mathrm{el}}/Q_{\mathrm{ion}}$ in formula 2.14, is significantly smaller for xenon than for argon. Consequently, the radius of the remaining nanoplasma is smaller and the fluorescing shell is significantly thicker. The described recombination and relaxation process, which evidently occurs on a time-scale shorter than the fluorescence lifetime, will be referred to as *non-radiative recombination* from here on.

---

[11] The nanoplasma radius defines the neutral cluster core.

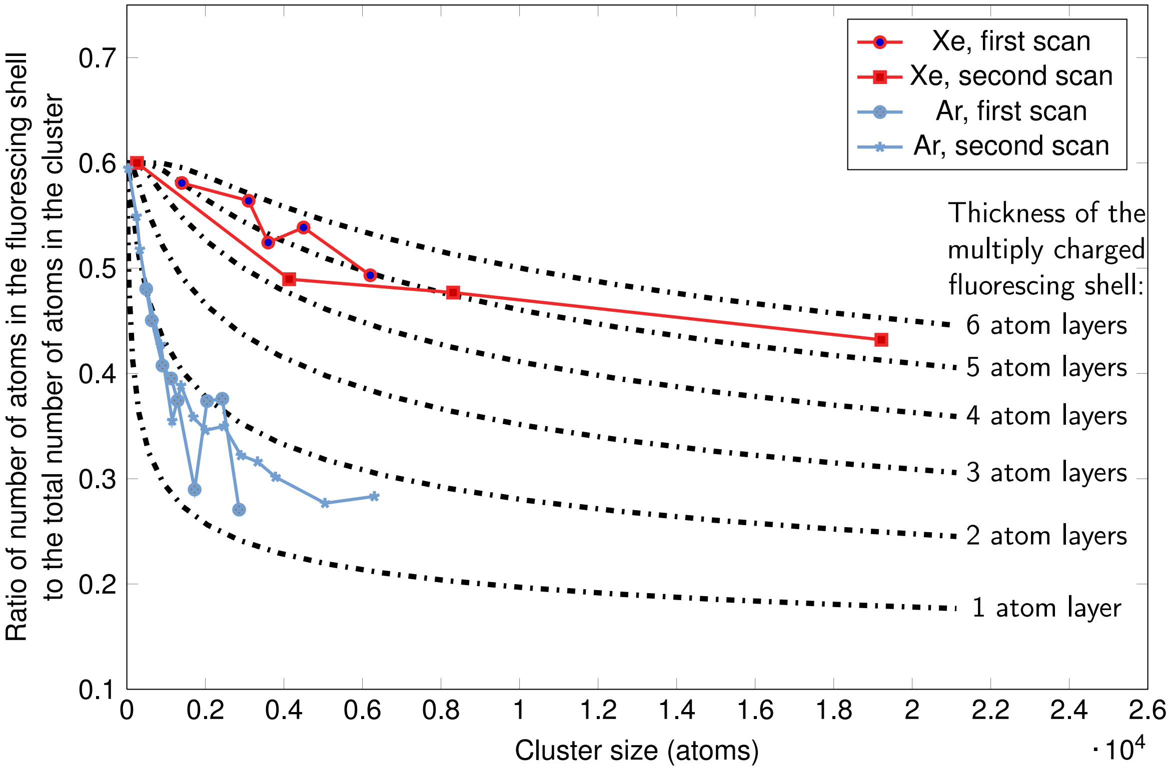

Figure 4.18.: Scaled total fluorescence yield in dependence on cluster size, compared to the shell model.

4.4.2. Cluster size effects in argon

The intent of this chapter is to find out if the dependence of the fluorescence yield per atom on the cluster size differs for individual charge states. In contrast to chapter 4.4.1, not the total fluorescence yield is taken into account but only the peak values of spectral lines which could be assigned to certain charge states[12] in table 4.5.

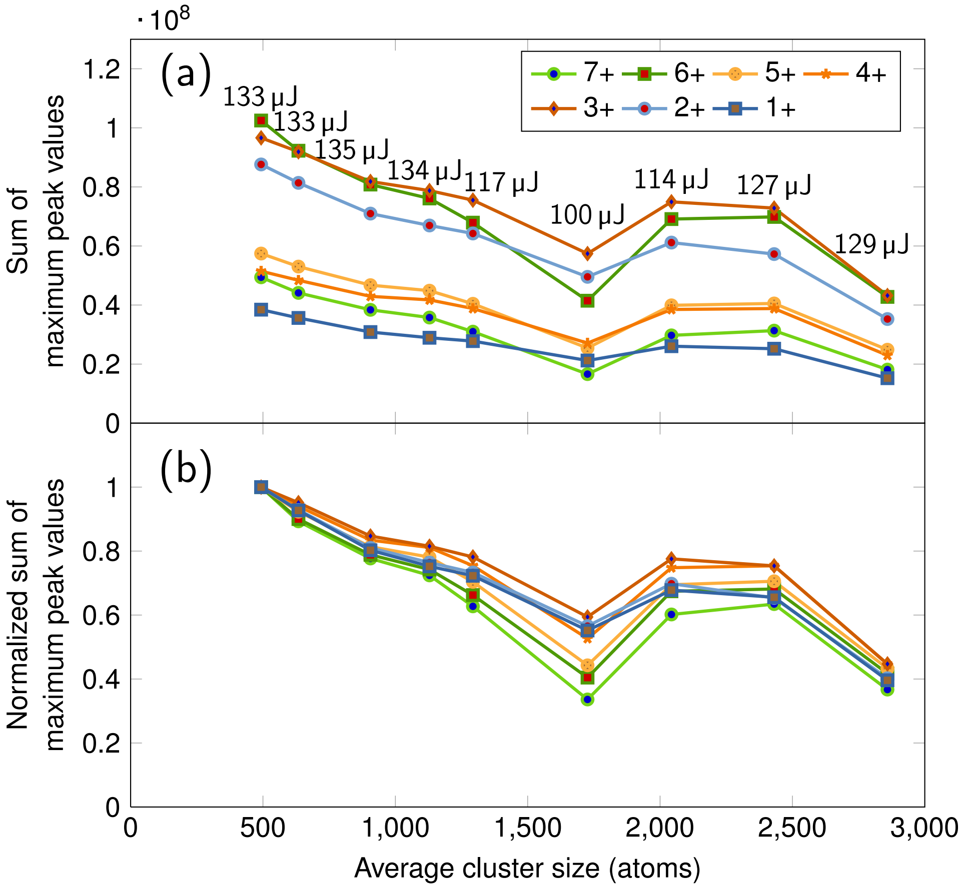

Figure 4.19.: First argon scan: (a) Evolution of the yield of different charge states in dependence on cluster size. Peaks which could not be identified were not considered. Pulse energies have been added at each position. (b) All charge states normalized to 1 at the smallest cluster size. The evolution of all charge states is very similar, except for the dip at a cluster size of about 1700 atoms, which is due to instability of the FEL pulse energy.

As was previously mentioned, machine instabilities led to a variation in the FEL intensity varied between $1.7 \cdot 10^{15}$ W/cm^2 and $2.33 \cdot 10^{15}$ W/cm^2.

Figure 4.19 (a) shows the summed yield of the separate charge states, according to the assignment in table 4.5. The average FEL pulse energies during each individual spectrum have been added to the plot. Clearly, the behavior of all charge states is very similar. This can also be seen in figure 4.19 (b), in which each yield has been normalized to 1 at the smallest cluster size. Consequently, the behavior of the individual plots is also very similar to the overall signal

---

[12] It has been checked for the total fluorescence yield that the peak evaluation gives essentially the same information as the analysis of the area below the fluorescence lines, which simplifies the analysis tremendously.

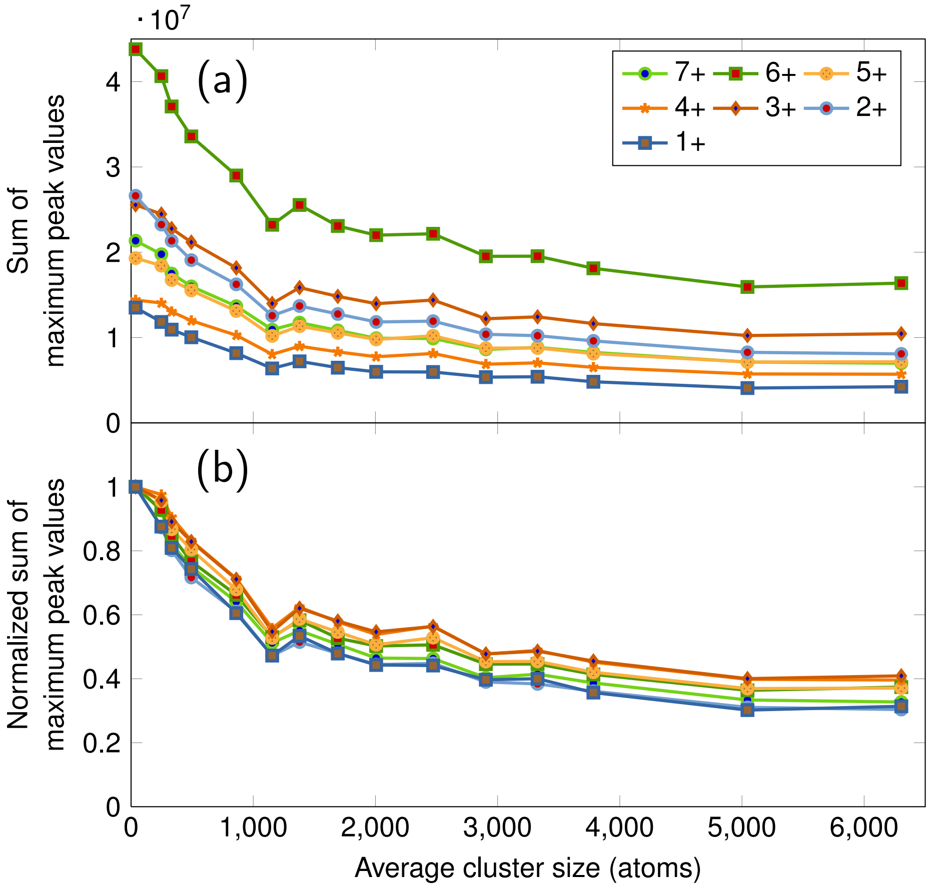

Figure 4.20.: Second argon scan: (a) Evolution of the yield of different charge states in dependence on cluster size. Peaks which could not be identified were not considered. (b) All charge states normalized to 1 at the smallest cluster size. The evolution of all charge states is very similar.

shown in figure 4.15.

An interesting exception to the similarity occurs at about 1700 atoms, where there is a reduction in the fluorescence yield whose severity varies depending on the charge state. The reduced fluorescence yield is an experimental artifact. It is due to the reduced FEL pulse energy for this particular measurement compared to the others in this size dependent study[13]. However, the observed behaviour for individual charge states corroborates the non-linear population of fluorescing states as discussed in detail in chapter 4.3.1. The severity of the dip follows a pattern: the higher the charge state, the more severe the decrease in yield. Ar^{7+} exhibits the most significant decrease, the yield of Ar^{6+} and Ar^{5+} is reduced slightly less. The lower charge states show progressively less reduction of the fluorescence yield. However, even Ar^{1+} still exhibits a certain reduction of the yield despite the normalization with respect to the FEL pulse energy, which assumed a linear dependence on FEL intensity (see beginning of chapter 4). The observed behavior confirms that in argon, the formation of all fluorescing states requires in general more than one photon.

Figure 4.20 shows the same kind of plot for the second argon cluster size scan, which extends to larger clusters of about 6300 atoms. As for the first scan, the behavior of different charge

---

[13] The pulse energies have been added to show that, while drops in pulse energy influence the yield, they are not responsible for the general decrease in yield for larger cluster sizes

states does not differ significantly[14], as can also be seen in the normalized version in figure 4.20 (b). The important finding of this analysis is that in argon the behavior of individual charge states resembles the behavior of the overall yield. Following the shell model introduced in the previous chapter, the fluorescence of all Ar charge states originates from an ionic shell of similar thickness. In other words, fluorescence spectroscopy of argon clusters does not reveal different radial distributions of charge states but a rather homogeneous distribution within a relatively thin outermost shell, consisting of approximately 2 atom-layers.

4.4.3. Cluster size effects in xenon

This chapter will take a closer look at the dependence of the yield of individual charge states of xenon on the cluster size. Figure 4.21 shows the evolution of each charge state depending on cluster size[15]. In contrast to the case of argon - where all charge states evolve nearly in the same manner -, the evolution of individual charge states with cluster size differs significantly in xenon.

One effect that is especially apparent is that the yield of Xe^{9+} decreases rapidly. Within the framework of the shell model of chapter 4.4.1, this behavior would suggest that the shell from which Xe^{9+} fluoresces is thinner than for the other charge states. Another possibility is that for increasing cluster size the non-radiative recombination, discussed in chapter 4.4.1, becomes more efficient for Xe^{9+} than for other charge states.

Looking at the line assignment in table 4.3, it is evident that the charge state $9+$ is represented by the spectral line at 14.9 nm and the surrounding lines. These lines all stem from transitions from the $5p$- to the $4d$-shell. These transitions are of great interest as they are expected to be the ones with the shortest lifetime; plasma density and temperature may affect the radiative transition. The population does not require secondary processes such as inelastic collisions with quasifree electrons. The excitation with 13.5 nm light is resonant with the $4d$-shell, therefore in the beginning holes are created predominantly in that shell. The $5p$-shell has the largest overlap with the $4d$-shell[16], so the fastest transitions will occur from there.

The $9+$-lines are not the only ones due to a $5p-4d$-transition. All the lines between 16 and 18.6 nm belong to $5p-4d$-transitions of charge states of Xe^{8+}, Xe^{7+} and Xe^{6+}.

In order to make a detailed comparison of the evolution of these transitions, I fitted the lines between 13.5 and 18.9 nm with a sum of Lorentzian curves of the form

$$f(x) = \frac{k/\pi}{k^2 + (x - \lambda_{\text{pos}})^2} \cdot I_{\text{line}}, \tag{4.6}$$

where k is half the width of the line at half of the maximum value (HWHM), λ_{pos} is the wavelength position of the center of the line and I_{line} is the intensity of the line. An example of a fitted spectrum is shown in figure 4.22.

Thereby, it is possible to estimate if all $5p-4d$-transitions behave in the same way, if individual

---

[14] Also, the relative abundance of the charge states is very similar in both scans. The main difference is that in the second scan the yield of Ar^{6+} and Ar^{7+} is higher than in the first scan. This slight discrepancy of the higher charge states being more abundant in the second scan can be attributed to the higher FEL intensity in the second scan (between $I = 2.3 \cdot 10^{15}$ to $2.6 \cdot 10^{15}\,\text{W/cm}^2$ compared to between $I = 1.7 \cdot 10^{15}$ to $2.3 \cdot 10^{15}\,\text{W/cm}^2$). The variation in intensity is due to machine instabilities, the position of the refocusing mirror was kept constant.

[15] In the case of xenon, the results of one scan were essentially reproduced in the other. Differences between the scans can be attributed to the higher FEL intensity during the second scan. Therefore, only results from one scan, the second one, are shown here.

[16] private communication R. Santra

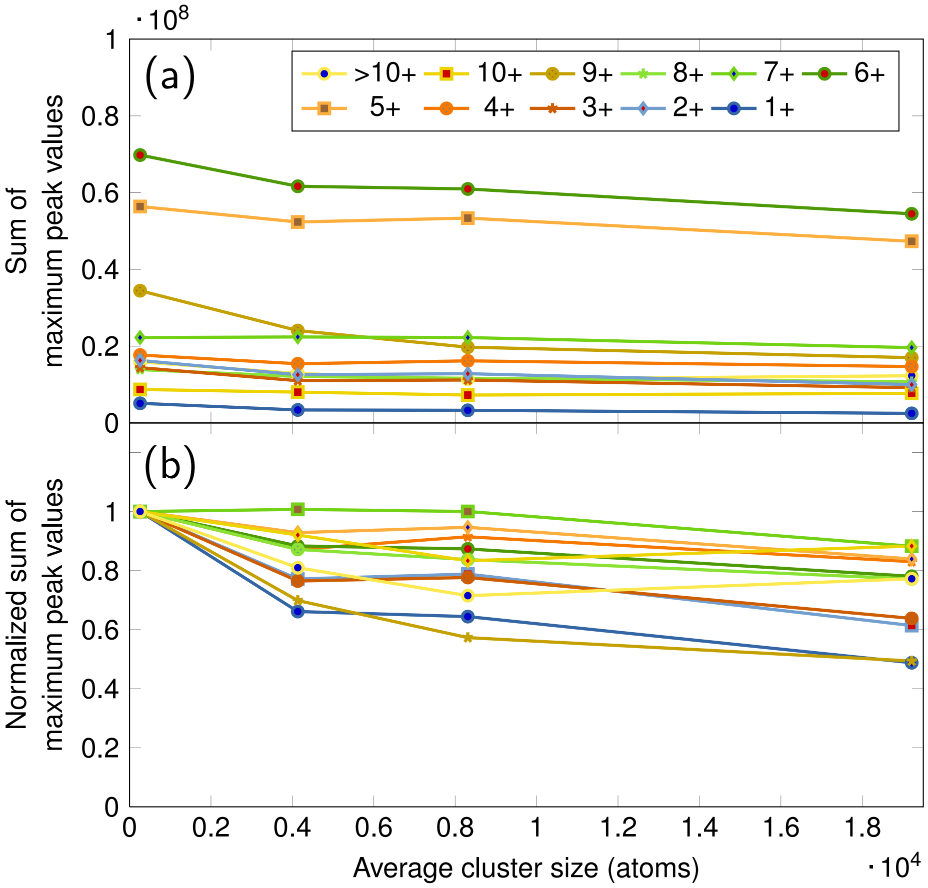

Figure 4.21.: Xenon: (a) Distribution of charge states in dependence on cluster size. Lines which could not be unambiguously assigned to a charge state (see table 4.3) were not considered. (b) All charge states normalized to 1 at the smallest cluster size. In this way, it is much easier to see that the behavior of xenon clusters is much more varied than that of argon.

charge states behave differently or if there is even a difference between lines of the same charge states.

Furthermore, one can see if there is a continuous trend in the evolution of the line widths. As these transitions are expected to occur the fastest, they offer the best possibility of observing an alteration of the lifetime - and therefore line widths - of the states.

For the fitting procedure, the wavelength positions were left free to be adjusted within $\pm 0.03\,\mathrm{nm}$. No boundaries were set for the line intensities. For most of the lines, boundaries for the full width at half maximum (FWHM) were set to 0.1 and 0.3 nm. For the conglomerate of lines dominated by the peak at 14.9 nm, however, these linewidths were not sufficient to accurately model the shape of the lines. I chose to widen the boundaries for the linewidths in this region to 0.54 nm FWHM[17].

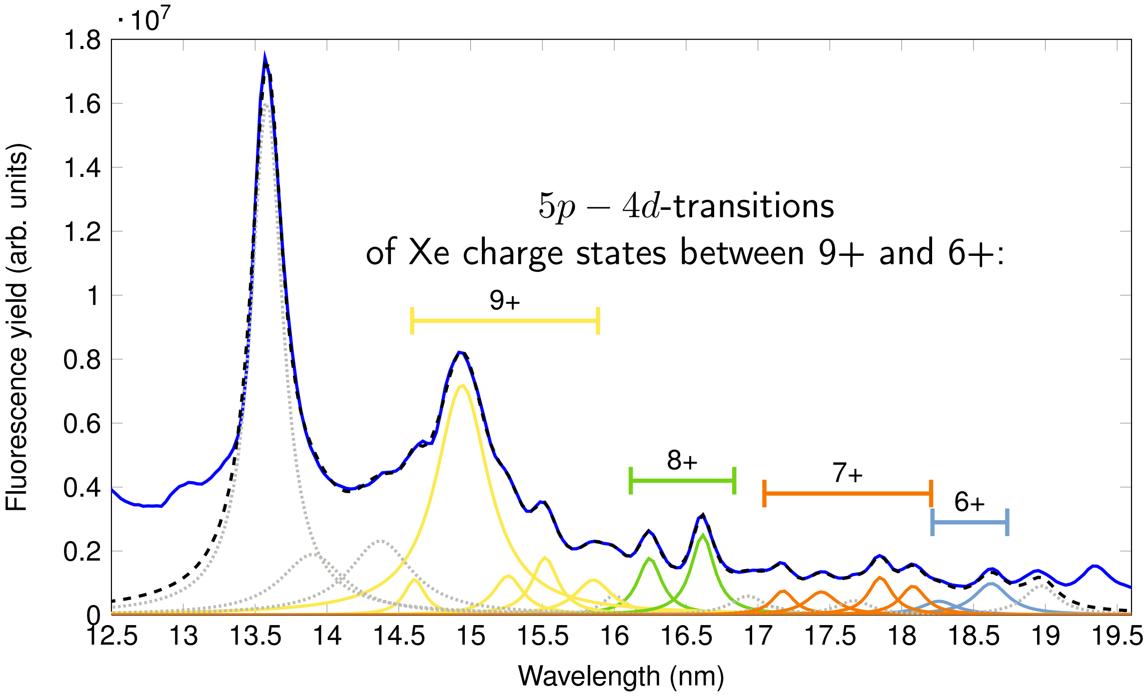

Figure 4.22.: Area of $5p - 4d$-transitions of xenon fitted by a sum of Lorentz curves. The sum closely resembles the signal of Xe clusters of an average size of about 4100 atoms. Colored fitted curves correspond to the charge states indicated above them.

The fits were executed in MATLAB. Each fit has an R^2 of at least 0.99. An R^2 of 1 would signify a perfect fit[18]. The stray light peak at 13.5 nm was included in the fit to make sure that

---

[17] While it is in principle possible that the wider lines are caused by a shorter lifetime, it is more probable that more lines contribute to the broad peak than can be identified in the spectra. According to the NIST database [67], there are many Xe^{9+}-lines close to the line at 14.93 nm, almost all of them also $5p - 4d$-transitions. Adding just two lines to the fit, at 14.9 and 15 nm, makes it possible to fit the observed peak with FWHMs between 0.1 and 0.3 nm. However, since no additional lines can be identified in the spectra, a single, wider fit was used. If there are indeed more lines present than can be identified, this procedure is an approximation because the sum of two Lorentzians is not a Lorentzian itself.

[18] R^2 is a measure for the goodness of the fit and is given by

$$R^2 = 1 - \frac{SS_{\mathrm{err}}}{SS_{\mathrm{tot}}},$$

where SS_{err} is the sum of the squared differences of each data point y_i and its fitted value f_i, given by

$$SS_{\mathrm{err}} = \sum_i (y_i - f_i)^2$$

and SS_{tot} is the sum of the squared differences of each data point from the mean value of data points a seeming variation in the Xe^{9+}-lines close to it was not in reality caused by a broadened stray light peak.

The stronger decrease of Xe^{9+} compared to all other charge states is validated by this analysis. Figure 4.23 shows the evolution with cluster size of the ratio $A_{9+,\,5p4d}/A_{<9+,\,5p4d}$, where $A_{9+,\,5p4d}$ is the area of the Xe^{9+}-lines and the $A_{<9+,\,5p4d}$ is the area of the $5p-4d$-transitions of lower charge states. It can clearly be seen that the area of Xe^{9+} decreases faster than the area of the lower charge states. If the area of Xe^{9+} and the other charge states decreased at an equal rate, the plots in figure 4.23 would obviously be horizontal lines. Unfortunately, no reproducible trend could be found in the behavior of the linewidths or of the positions of the spectral lines.

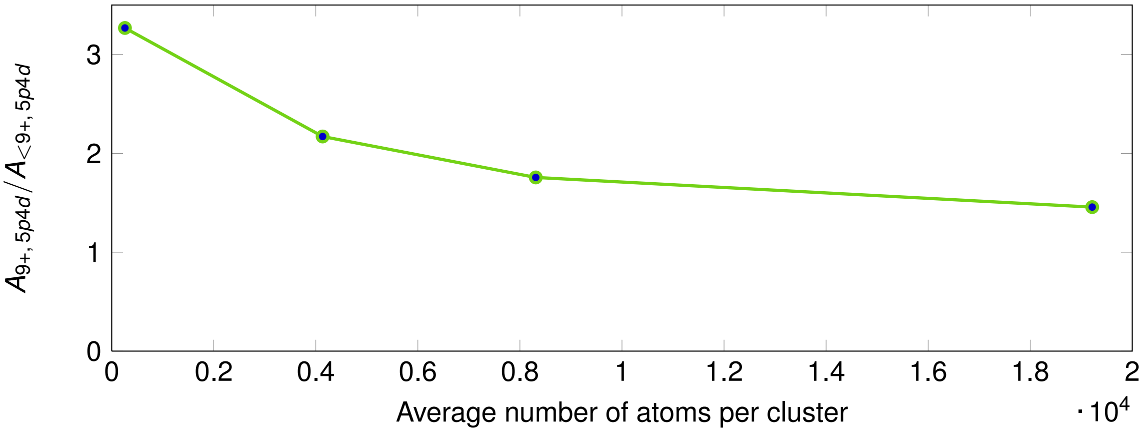

Figure 4.23.: Evolution of the Xe^{9+} charge states stemming from $5p-4d$-transitions in comparison to the $5p-4d$-transitions of lower charge states. The negative slope shows that in larger clusters the yield of Xe$^{9}+$ drops faster than the yield of other $5p-4d$-transitions.

The main outcome of this section is that there are significant differences in the FEL-induced fluorescence of individual charge states of xenon and argon with increasing cluster size. In argon, all charge states evolve in virtually the same way. In xenon, on the other hand, the behavior of individual charge states differs significantly. Such a variation with cluster size at an FEL wavelength of 13.5 nm has not been published yet. As was mentioned before, Thomas et al. [20] observed a drop in the average charge state per atom in the charged outer shell from 2 for $\overline{N}$=50 to 0.5 for $\overline{N}$=7800. While they certainly proved a dependence on the cluster size, their electrostatic model does not predict the behavior of individual charge states. Our observation of the rapid decrease of fluorescence yield per Xe^{9+} ion with increasing cluster size could play an important role in the decrease in the overall charge states observed by Thomas et al. microseconds after the interaction by means of mass spectrometry.

The differences in the dependence on cluster size of individual charge states confirm that there are complex ionization, charge redistribution and relaxation mechanisms at work in xenon clusters, which certainly warrant further investigation. Theoretical calculations and additional experiments are needed to gain a deeper understanding of the effects.

$\bar{y}$, given by

$$SS_{\text{tot}} = \sum_i (y_i - \bar{y})^2$$

4.5. Xenon-core-argon-shell clusters

The experiments on pure clusters have shown that fluorescence predominantly stems from a layer of atoms on the surface of the cluster, with no discernible contribution from the cluster core. Now the question arises: what happens if the cluster consists of a strongly absorbing core of one species and a surrounding atom shell of a different element that absorbs much less photons? Will the shell still be multiply charged and fluoresce or not?
Chapter 2.4 already gave an overview of related mass spectrometric studies by Hoener et al. on so-called core-shell clusters [9], which had a xenon core and a surrounding shell of argon atoms. Figure 4.24 shows the recorded TOF spectra of core-shell-clusters of 400 and 4000 atoms, respectively. The TOF spectra of the core-shell clusters showed only very low charge states of xenon, up to 2+ at experimental conditions similar to those in our experiment, while pure xenon clusters produced charge states of up to 9+. The results indicate an efficient exchange of energy and charge between the surface and the core at some point in time during or after the interaction. Since fluorescence spectroscopy gives complementary information, as already shown in previous chapters, we expect to gain new information by investigating fluorescence from core-shell clusters.

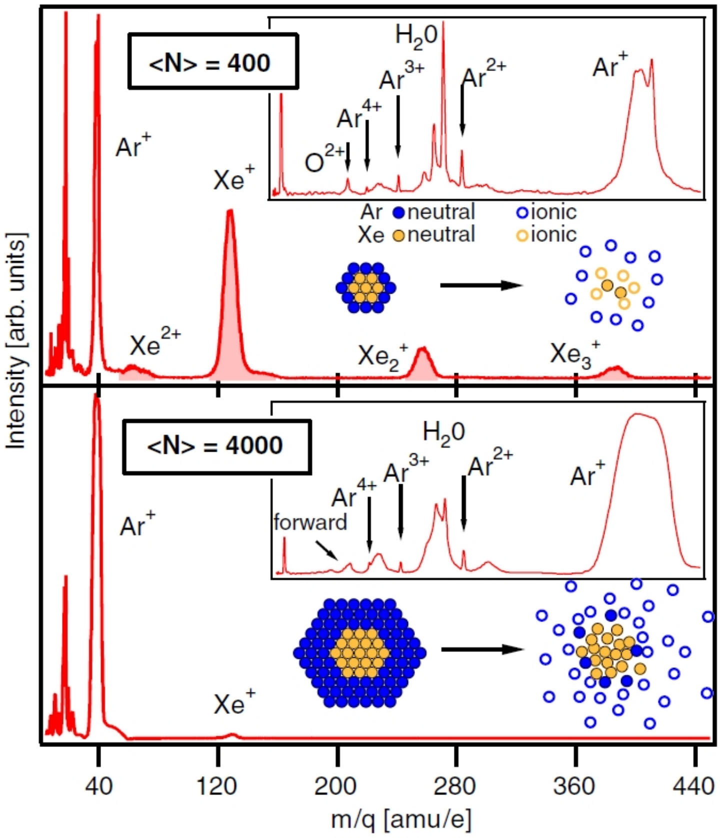

Figure 4.24.: Ion time-of-flight spectra of Xe-core-Ar-shell clusters measured by Hoener et al. [9]. Small clusters with a thin argon shell exhibit only low charge states of xenon stemming from the core. Clusters with a thicker shell hardly show any xenon signal at all. The few detected xenon ions are only singly charged. In the same experimental conditions, pure xenon clusters showed charge states up to 9+.

The clusters were produced by expanding a gas mixture of 2 % xenon in argon through a nozzle with the same geometry as in the TOF experiments of Hoener et al. [9]. The pressure at the nozzle was 6500 mbar. According to the discussion in chapter 2.1, this pressure produces, on average, clusters of 400 argon atoms with an embedded core of about 80 xenon atoms. These experimental parameters are virtually the same as those for the smaller core-shell clusters in the experiments of Hoener et al. [9].

Figure 4.25 shows a comparison between fluorescence spectra of core-shell clusters and pure argon clusters. Here, only fluorescence in the short-wavelength range of the spectrometer is displayed because interesting differences can be observed. Relative line intensities vary between both spectra, but for the most part of the spectra, all lines which appear in the core-shell spectrum are also present in the pure argon spectra. This means that the vast majority of the spectrum consists of spectral lines of argon atoms, which were situated in the cluster shell. However, as a crucial exception to this observation, xenon-core-argon-shell clusters fluoresce at low wavelengths, between 10.5 and 12 nm. This signal is absent in pure argon clusters. The wavelength range in which additional transitions appear in the core-shell spectrum is highlighted. We assign the fluorescence at short wavelength to the xenon ion core because it coincides with the most prominent peak (apart from Rayleigh scattering from the clusters) in the pure Xe spectra.

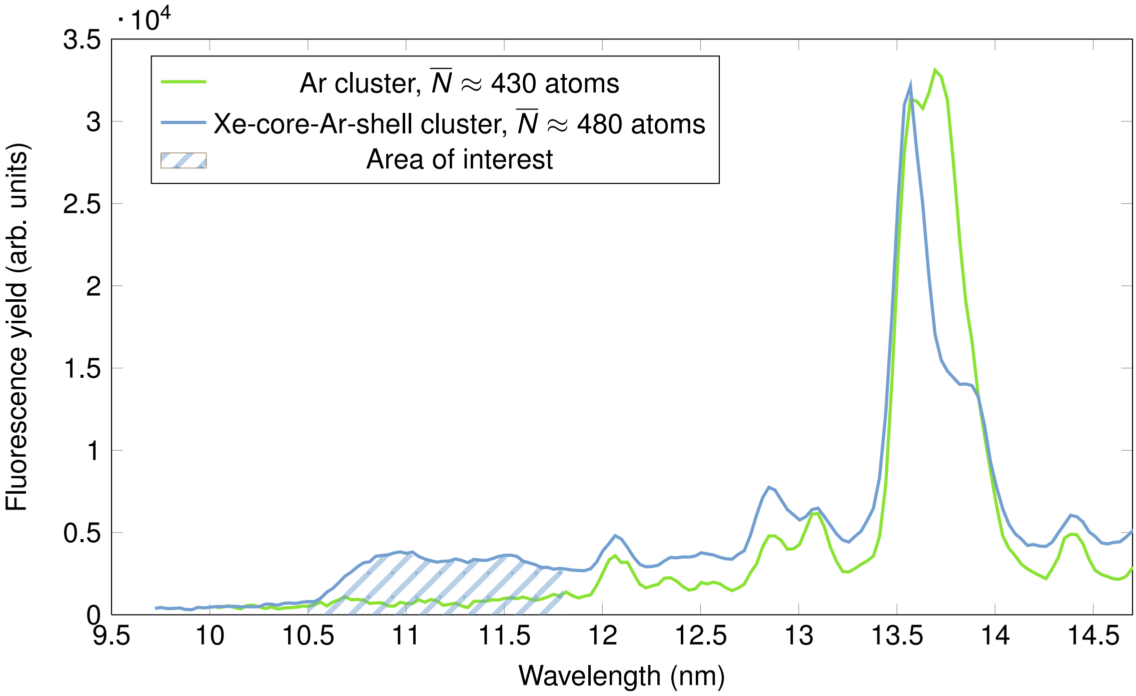

Figure 4.25.: Comparison of a core-shell cluster spectrum and a spectrum of pure argon clusters of similar size. The area of interest highlights spectral lines in the core-shell spectrum which are not present in the pure argon spectrum.

In order to extract the effect of the cluster composition on the fluorescence spectra, I attempted to emulate the core-shell spectrum by combining spectra of pure xenon and pure argon clusters. We measured an argon spectrum with an average cluster size of 430 atoms, very close to the size of the core-shell clusters. Unfortunately, a spectrum of xenon clusters as small as 80 atoms is not available. Therefore, I chose to use one of the smallest available xenon spectra, with an average of about 260 atoms. The normalization factor, which determines the contribution of the pure Xenon spectrum, is derived by an analysis of the straylight signal in each spectrum. The detailed procedure is discussed in the following[19]. As shown in figure 4.26, there is a clear difference in the intensity of the stray light peak between pure argon and core-shell clusters.

---

[19] It must be pointed out that this method is not expected to be exact. In a core-shell cluster, the two constituents influence each other. This cannot be duplicated by combining spectra of pure clusters. Furthermore, the use of a scaled xenon spectrum neglects that spectral lines and the stray light may depend on the cluster size in a different way. Therefore, a Xe cluster size as close as possible to the

This becomes apparent only if one fits the straylight and the spectral line adjacent to it both for the core-shell cluster and the pure argon cluster. The signals at 13.6 nm of pure argon and of the core-shell clusters are of very similar height, but the stray light peak in argon has a strong contribution from the adjacent spectral line, which is in fact stronger than the stray light itself. In the core-shell cluster, this fluorescence line is much weaker. A fit of the lines reveals that the area under the stray light peak of the core-shell-cluster is more than two times larger than for pure argon. The weighting of spectra is based on the assumption that this difference is due to the presence of the xenon core. As was seen in chapters 4.2 and 4.3, xenon scatters light with a wavelength of 13.5 nm much more efficiently than argon. It must be pointed out that even though the xenon atoms are located in the center of the cluster they can still contribute to the scattering signal. Firstly, the absorption cross section of neutral argon atoms is not large enough to keep photons from reaching the cluster core. Secondly, once a nanoplasma has formed, the depth to which light can penetrate into a plasma, the so-called *plasma penetration depth* δ_p, is still much larger than the cluster radius. This can be shown with an estimate. The plasma penetration depth δ_p is given by (see, for instance, Attwood [1]):

$$\delta_p = \frac{c}{\omega_p}, \tag{4.7}$$

where c is the speed of light and ω_p is the plasma frequency

$$\omega_p = \sqrt{\frac{n_e e^2}{\epsilon_0 m_e}}. \tag{4.8}$$

The electron number density is designated by n_e, e is the electron charge, ϵ_0 is the vacuum permittivity and m_e is the electron mass. Plugging in the constants, one arrives at

$$\delta_p = 5.31 \cdot 10^5 \frac{1}{\sqrt{n_e/\text{cm}^{-3}}} \text{cm} \tag{4.9}$$

The electron density can be estimated by assuming a certain average charge state for an argon cluster of 400 atoms. The electron density is the product of the average charge state $\langle q \rangle$ and the number N of atoms in the cluster, distributed over the cluster volume V_c.

$$n_e = \frac{\langle q \rangle N}{V_c} = \frac{\langle q \rangle N}{\frac{4}{3}\pi (N^{\frac{1}{3}} r_s)^3} = \frac{\langle q \rangle}{\frac{4}{3}\pi r_s^3}, \tag{4.10}$$

where r_s is the Wigner-Seitz-radius. Obviously, in this estimate the electron density depends only on the average charge state and not on the number of atoms in the cluster.

Even assuming an average charge state of 8+, which is larger than the highest detected charge states in pure argon clusters as discussed in chapter 4.3.1, this gives a plasma penetration depth of about 12 nm, much larger than the cluster radius of $400^{1/3} r_s \approx 1.5\,\text{nm}$. Consequently, the FEL light reaches the xenon core and is scattered. Therefore, the difference in scattering intensity between the core-shell spectra and the pure argon spectra is attributed to the presence of the xenon core. The xenon spectrum is normalized by calculating the area of the Lorentz-fitted stray light peak in all three spectra. The spectra and the fitted lines are shown in figure

---

size of the core of the core-shell cluster is chosen.

4.26[20]. The difference between the area of the stray light peak of the core-shell and the pure argon clusters was determined. The xenon spectrum was divided by a factor to make up for this difference.
The result of the addition of the argon spectrum and the normalized xenon spectrum is shown in figure 4.27 in comparison to the measured spectra of core-shell clusters and pure argon clusters. There is a clear similarity in the structures between 10.5 and 12 nm of pure argon and the core-shell clusters. Both structures start at virtually the same position and their surface area is very similar. A perfect agreement would in fact be very surprising, because firstly the xenon signal of the synthesized plot stems from ions which originated from a somewhat larger cluster than the cluster core. Secondly, interactions between the two constituents of the core-shell cluster cannot be replicated by this method. Nevertheless, the result is clear evidence of the presence of xenon lines in the core-shell spectra. Much more importantly, it is clear evidence of *highly charged* xenon ions. As was shown in chapter 4.2.1, xenon lines between 10.5 and 12 nm correspond to charge states of at least Xe^{11+}, the highest charge states we measured. In other words, the Xe charge states observed in the core-shell clusters are just as high as those in pure xenon spectra. This result is a striking difference to mass spectrometry, where no charge state higher than Xe^{2+} was detected (Hoener et al. [9]).
Our findings have important implications:

1. The signal must *come from the cluster core*. Therefore the conclusion of the last chapter has to be extended: even though the majority of fluorescence photons comes from ions stemming from a surface layer of the cluster, there is also a small contribution from ions located in the cluster core. This signal is too small to be discernible in the spectra of pure clusters.

2. The measured fluorescence of these spectral lines must occur *fast*. If the highly charged ions were still present after the cluster has disintegrated, these charge states would also be present in the TOF spectra of Hoener et al. [9].

In summary, the experiments show *direct* evidence that even in core-shell clusters the xenon core is initially highly charged, i.e. during the interaction and before disintegration. The results prove that the XUV fluorescence spectroscopy can provide information which is not accessible by time-of-flight spectroscopy.

---

[20] The spectral lines and the stray light of the Xe spectrum are wider than in the spectra shown in chapter 4.2, possibly due to a slight misalignment of the spectrometer. However, for the normalization, the surface area of the stray light peak is used. This area stays constant if the focusing becomes worse because the same number of photons is merely spread out over a wider region of the detector. Therefore, the normalization remains valid.

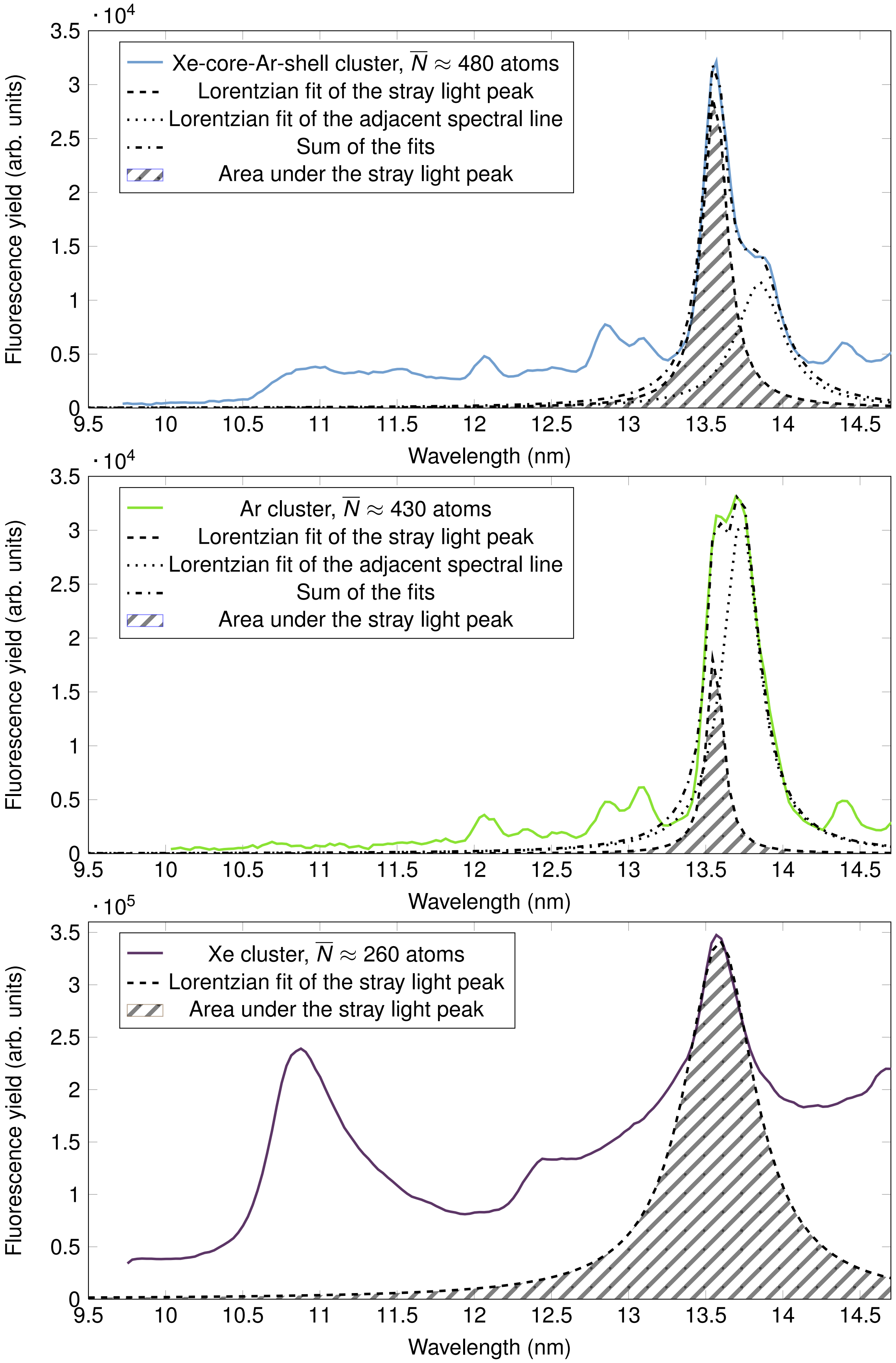

Figure 4.26.: Lorentzian fits of the stray light peak and the adjacent spectral line for Xe-core-Ar-shell clusters and pure argon clusters. Only the stray light peak is fitted in case of pure xenon clusters.

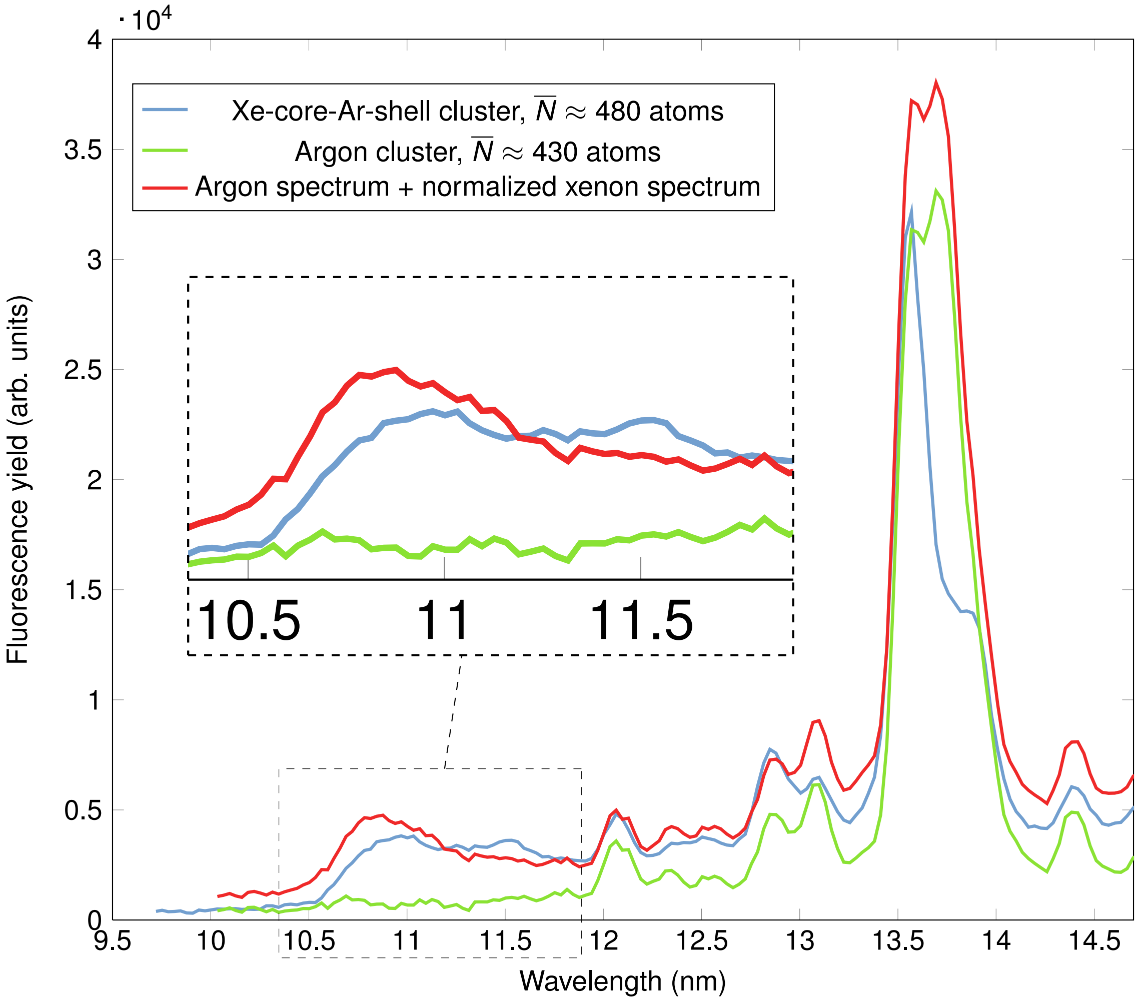

Figure 4.27.: Comparison of the measured Xe-core-Ar-shell spectrum, the pure argon spectrum and the spectrum synthesized from the argon- and a normalized xenon spectrum. The Xe-core-Ar-shell spectrum and the synthesized spectrum show reasonable agreement at very short wavelengths where Xe charge states of at least 11+ appear. This signal in the Xe-core-Ar-shell spectrum must stem from the xenon atoms embedded in the cluster core.

5. Summary and outlook

The presented work has illustrated that experiments on rare gas clusters in strong XUV laser pulses are a fruitful field of research and will remain so for some time, as there are still many unanswered questions. In this chapter, the most important results of the thesis will be reviewed and I will give an outlook to experiments which could be based on these results in the future.

The main aim of this work was to analyze charge states which are created early in the interaction of rare gas clusters with an FEL. In order to do this, an XUV spectrometer was designed and constructed[1]. It is sensitive across a wide spectral range, from 10 nm to 76 nm. The diffraction grating diffracts as well as focuses the radiation onto a flat detection plane. The use of a single optical element keeps the inevitable absorption of radiation at a minimum. The resulting transmission of the spectrometer is $1 \cdot 10^{-7}$. The measured resolution (theoretical values in brackets) is $\Delta\lambda/\lambda = 53$ at 12.3 nm ($\Delta\lambda/\lambda_{\text{theo}} \approx 197$) and $\Delta\lambda/\lambda = 491$ at 73.6 nm ($\Delta\lambda/\lambda_{\text{theo}} \approx 1067$). One possible explanation for the discrepancy between measured and theoretical values is that most of the measured spectral lines are in fact closely spaced overlapping lines.

Experiments on xenon, argon and xenon-core-argon-shell clusters were carried out. Clusters were produced by gas expansion through a conical nozzle. Average cluster sizes between 250 and 19000 atoms were evaluated for xenon, and between 40 and 6300 atoms for argon. Clusters were illuminated with pulses from FLASH (pulse energies up to 150 µJ, estimated pulse duration of 150 ± 50 fs). By moving a refocusing mirror, the peak FEL intensity in the cluster jet could be varied between $5 \cdot 10^{13}$ W/cm^2 and $2.7 \cdot 10^{15}$ W/cm^2. An assignment of charge states is possible by evaluating the dependence of the fluorescence spectra on FEL intensity.

In the experiments on pure xenon clusters, charge states up to at least 11+ were detected, in reasonable agreement with previously published works using ion-time-of-flight spectrometers [9, 20]. The dependence on cluster size varies significantly between individual charge states of xenon. Especially the yield of Xe^{9+} per atom decreases very fast compared to other charge states.

In argon, on the other hand, all charge states evolve very similarly. In argon, charge states up to 7+ were detected. This result is in line with the much smaller photo-absorption cross section of argon at 13.5 nm, compared to xenon.

Very interestingly, the behavior of the total yield of xenon as well as argon in dependence on cluster size can be explained by assuming that fluorescence is only emitted from a shell of ions on the surface of the cluster during the disintegration of the clusters (Coulomb explosion of the shell and hydrodynamic expansion of the cluster core). We showed that this shell is thicker in xenon than in argon clusters. Due to the higher cross section, plasma heating by the excess energy of inner-ionized electrons is much more efficient in xenon. Consequently, many more electrons can leave a xenon cluster and the diameter of the resulting nanoplasma is smaller in xenon than in argon. It follows that the fluorescing shell of xenon clusters is thicker compared to argon, because fluorescence is suppressed in the nanoplasma: Quasi-free electrons, which form the nanoplasma, recombine with ions in the cluster core. The electronically excited ions return to the ground state by inelastic collisions with other quasi-free electrons on a timescale shorter than the fluorescence lifetime (non-radiative recombination).

This picture is in general agreement with mass spectrometric results [20]. However, the finding

---

[1] The compact design of the spectrometer makes it possible to be used in different experiments. For instance, it was used in the first measurement of seeded FEL operation at FLASH [96].

(for Xe clusters) of ≈5 multiply-charged shells from fluorescence spectroscopy compared to 3 multiply-charged shells from mass spectrometry may already be a sign that fluorescence spectroscopy gives a time-integrated signal that includes all phases of the FEL-cluster interaction. It suggests that early in the interaction, ions are distributed over a thicker shell, which first fluoresces and then partly recombines. Thus, the number of multiply charged shells derived from mass spectrometry is less than the number derived from fluorescence spectroscopy.

In the present thesis, the sensitivity to fluorescence from the cluster core could be significantly increased by investigating clusters that are composed of a core and a shell of different elements. In fact, experiments on xenon-core-argon-shell clusters show that there is also a small portion of fluorescence which stems from the cluster core and is emitted fast. Here, we observed xenon charge states of at least 11+, just as high as in pure xenon clusters. This is an important result, which could not be obtained by ion TOF measurements: Hoener et al. [9] observed only charge states up to 2+ in xenon stemming from xenon-core-argon-shell clusters of the same composition as in our experiments. In pure xenon clusters, on the other hand, they measured charge states up to 9+ . We therefore know that the fluorescence signal from the core is emitted fast, before the ions would inevitably be neutralized, because otherwise the high charge states would also have been detected in the experiments of Hoener et al.. This result shows the potential of fluorescence spectroscopy for analyzing charge states created early in the interaction of clusters and light *before* recombination sets in. It also points to possible future experiments for measurements which are not possible with the current setup.

The results presented in this thesis show that many interesting effects manifest themselves in the short wavelength range of our spectrometer, between about 10 and 25 nm. Examples are the strong decrease with growing cluster size of $5p-4d$-transitions of Xe^{9+} compared to other $5p-4d$-transitions and the generation of spectral lines at shorter wavelengths than the excitation wavelength. The incorporation of another diffraction grating, designed for a narrower wavelength range, will make it possible to study these phenomena in more detail and also increase the chance of observing spectral line broadening and/or shifting due to cluster or plasma effects.

Due to uncertainties in experimental conditions at FEL facilities, a comparison of previously published ion-TOF spectra to the measured fluorescence spectra, while important, is not as definitive as a synchronous measurement of fluorescence spectra *and* ion-TOF spectra would be[2]. Such measurements would allow us to identify with sufficiently high accuracy if even in pure clusters the maximum charge state detected by fluorescence spectroscopy is higher than the one detected by ion-TOF measurements. Furthermore, varying the FEL intensity or the average cluster size in such simultaneously performed studies and comparing the relative change in the charge state distributions would allow conclusions regarding ionization dynamics and possible changes in the population of specific electronic states.

We showed that it is possible to record fast fluorescence from the cluster core by using core-shell clusters. However, the signal is only visible in a spectral range where the sensitivity of the spectrometer is highest and where the cluster shell emits no fluorescence. It would be very desirable to be able to detect this fast signal across the whole spectrum. An ambitious experiment would be to incorporate time-resolved techniques such as an XUV streak camera into the setup, in order to directly record fluorescence lifetimes.

---

[2] We attempted such simultaneous measurements but the preexisting experimental setup caused restrictions to the design of the TOF spectrometer which make the spectra difficult to analyze.

A. Appendix

This chapter is mainly intended to provide technical information which may be useful in the continuation of the experiments presented in this thesis.

A.1. Ion time-of-flight-spectrometer for simultaneous ion and photon detection

As was mentioned in the summary, the simultaneous measurement of fluorescence spectra and ion mass spectra would allow for an exact comparison of the charge states detected with each method. The most common method of measuring ion mass spectra in FLASH experiments are time-of-flight spectrometers (TOFs). TOFs are described in detail in [97], for instance. For this section, only the basic principle is needed: ions are formed at a defined moment in time in the detection region of the TOF. Electric fields are used to collect and guide the ions to the detector. It takes the ions a certain time to travel from the point of creation to the detector. This time is for each ion proportional to the ratio of mass and charge of the ion m/q. The mass m is known, so by measuring the time between creation - defined by the FLASH pulse - and the arrival at the detector, one can determine the charge state of ions.

A common setup of a TOF is the Wiley-McLaren configuration [98], which minimizes the difference in flight times of ions of identical mass and charge which travel in different directions immediately after their creation. A basic schematic is shown in figure A.1. Three elements are used to get the ions into a field-free drift tube and finally onto the detector: the repeller and the extractor guide the ions and the lens focuses them onto the detector.

In the case of our experiment, shown in figure 3.2, such a setup could not be employed due to geometric restrictions imposed by the existing experimental setup. Therefore, a TOF which does not use a repeller plate was designed and simulated with SIMION by Andreas Kickermann, another PhD student in our group, on short notice. The design is shown in figure A.2. Its main components are a skimmer[1] (opening diameter ~1 mm), to which a negative voltage can be applied, followed by an electrostatic lens and a long drift tube which ends directly in front of the detector. The detector is a commercial design, made of an MCP, a scintillator and a photomultiplier tube. Voltages which, according to A. Kickermann, are a good starting point for an experimental optimization are given in table A.1. The setup can be moved by an xyz-manipulator to point the skimmer directly at the interaction region.

A critical boundary condition of the design was the need for a vacuum of better than $1 \cdot 10^{-6}$ mbar at the detector, dictated by the MCP. As the generation of clusters requires the introduction of high-pressure gas into the vacuum chamber, two differential pumping stages[2] are needed in the TOF. They are implemented in the following way: the drift tube is surrounded by a tube with slightly larger diameter. This tube extends to the first pumping stage. The inside of the

---

[1] Skimmers look like funnels which are mounted tip first. They are usually used to let only the central portion of a cluster beam pass into the interaction volume.

[2] The term differential pumping refers to mounting vacuum pumps at portions of a vacuum chamber which are not strictly isolated vacuum-wise, but are only connected by a passage with a low conductivity for gas, usually a long, thin tube.

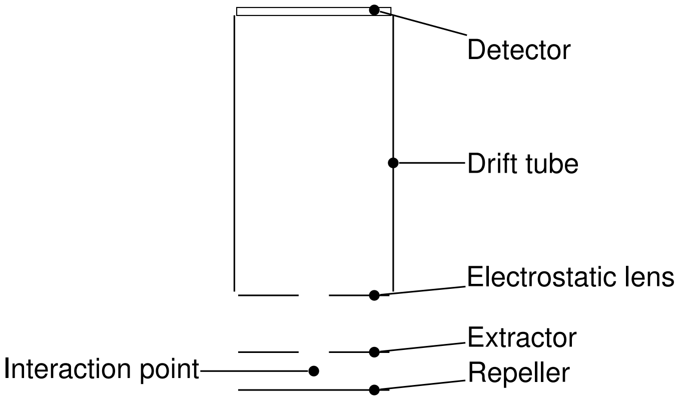

Figure A.1.: Schematic layout of a Wiley-McLaren TOF

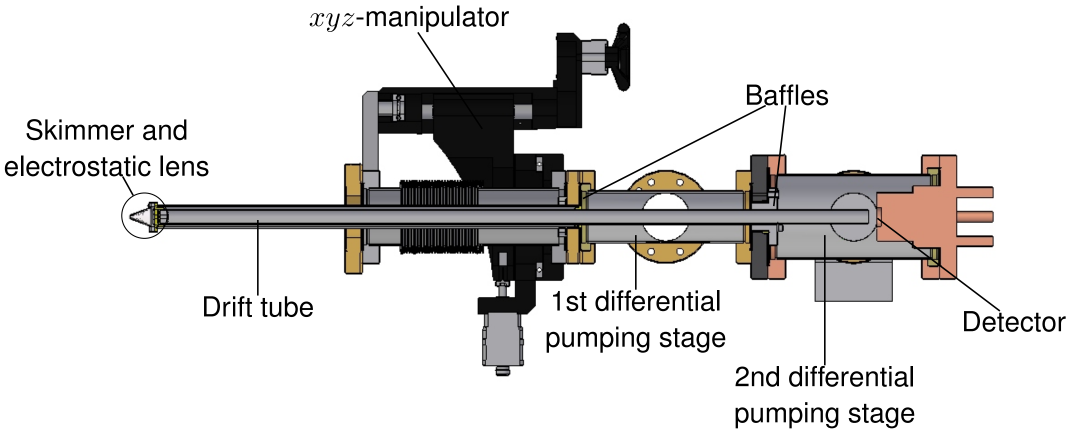

Figure A.2.: Cross section of the ion time-of-flight spectrometer designed by Andreas Kickermann for simultaneous measurements of mass spectra and fluorescence spectra.

Element	Voltage (kV)
Skimmer	0
Lens	increase until signal is visible (more than $-3\,\mathrm{kV}$during beamtime)
Drift tube	-2
MCP front	-2
MCP back	-1
Scintillator	$+2.5$
Photomultiplier tube	max. -0.8

Table A.1.: Voltages for the components of the differentially pumped TOF. A modification of the voltages may be necessary in the experiment. The voltage of the drift tube should in general be equal to the voltage at the MCP front, otherwise an additional acceleration (positive or negative) of the ions takes place. The maximum voltage difference between the MCP front and back is 1.2 kV, the maximum voltage difference between the MCP back and the scintillator is 4.5 kV.

manipulator is connected to the vacuum system of the main chamber. The second pumping stage comprises the detector and the inside of the drift tube. The pumping stages are separated by baffles through which the tubes pass with close tolerances. Figure A.3 shows how the TOF is mounted in the experimental chamber. Both the fluorescence spectrometer and the TOF observe the same interaction point.

Unfortunately, the measurements during the beamtime revealed that the time-of-flight spectra kept changing, even though the experimental condition were kept constant. The most likely reason for the changes are charging effects in the TOF which distort the electric fields. A component on which charges could accumulate is the piece which keeps the skimmer, the electrostatic lens and the two tubes isolated from each other. This part is necessary because all of those components are operated at independent voltages. Obviously, this component has to be made of an isolating material. Selectively coating this isolating spacer with graphite powder, to allow charges to dissipate, seemed to have an effect but did not ultimately solve the observed problems.

In conclusion, more experimental experience with the TOF is needed to understand and solve the observed phenomena. Alternatively, the experimental setup could be changed in such a way that a more classical TOF geometry could be employed while still making use of the double differential pumping stage designed for this spectrometer. Solving the present challenges is crucial, because the simultaneous measurement of fluorescence and mass spectra is a very important next step in this project.

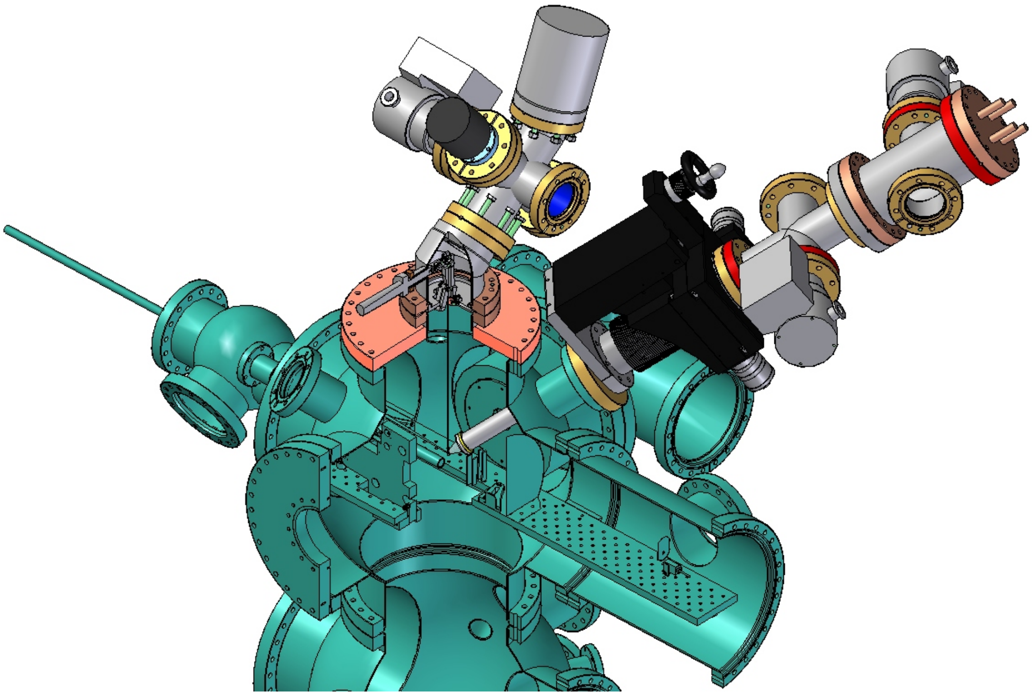

Figure A.3.: Position of the TOF in the experimental chamber. Both the fluorescence spectrometer and the TOF look at the interaction point.

A.2. Compact xy-manipulator

As was mentioned in chapter 3, the fluorescence spectrometer is intended as a universal device, usable in different experiments. To this end, I adapted the design of an xy-manipulator with a very compact height. The design was made available to me by Dr. Klaus van Haeften and Stuart Thornton from the University of Leicester. Due to height restrictions imposed by the vacuum chamber and because the necessary adjustments were possible by other means (see chapter 3), the manipulator was not yet constructed. It may however be a useful device for future measurements, so the design is briefly documented here. The design is shown in figure A.4. The manipulator consists of three plates, a base plate, which is fixed in space and two plates which can be moved in relation to it, one in the x-direction and the other in the y-direction. If the plate in the middle is moved, the one on top moves as well. If the one on the top is moved, the middle one is stationary. In the base plate, there is a raised groove for an o-ring onto which the top plate is pressed. In the middle plate, there is an opening which is wider than the raised lip for the groove so that the plate can be moved around it. Circular plates made of a material with a low friction coefficient are inlayed into the base plate and the middle plate and sit slightly proud of the surface. This is to minimize friction between the plates of the manipulator. In the current state, movement is planned to be controlled by machine screws but incorporating micrometer screws and spring-loading, for example, would be straightforward. According to Dr. van Haeften, such a manipulator can be mounted vertically as well as horizontally, provided that clamps are added to keep the plates on top of each other when the chamber is vented. He reports that pressures of at least $2 \cdot 10^{-7}$ mbar are possible, without alteration when the manipulator is moved. The o-ring should be slightly lubricated with vacuum-compatible grease.

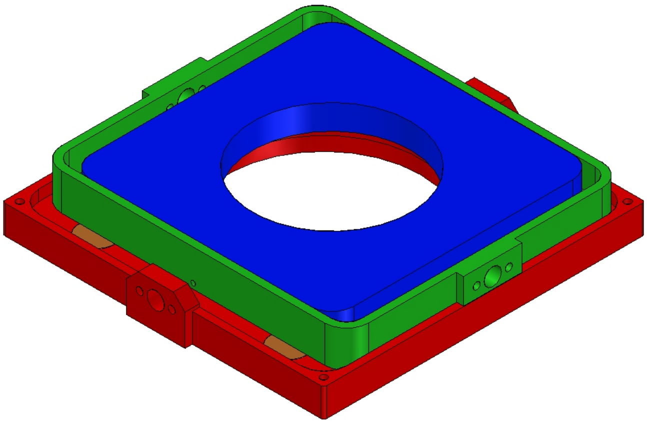

(a) Isometric view

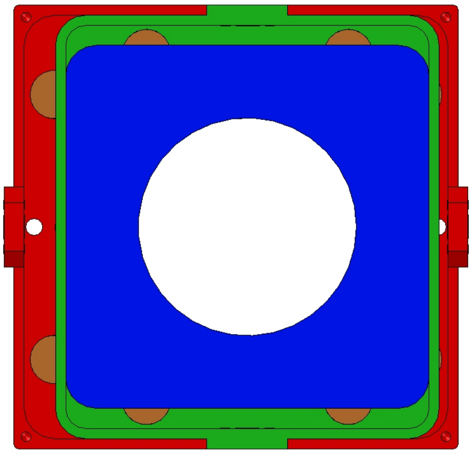

(b) Top view

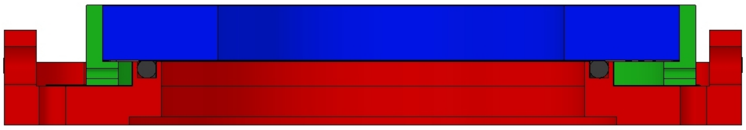

(c) Cross section

Figure A.4.: Compact xy-manipulator. The top plate (blue) is nested inside the middle plate (green), which is nested inside the base plate (red). Some of the friction reducing plates (bronze-colored) can also be seen. The top plate is only schematic; an experimental device would be mounted on it. In the cross section (c), the o-ring (black) can be seen.

A.3. Comparison with electron impact induced fluorescence

Apart from the measurements at FLASH, we also recorded fluorescence spectra induced by collisions with electrons from an electron gun. The measurements were carried out at the Technische Universität Berlin and are the topic of the diploma thesis of Tim Oelze [99]. The figures in this section are from his thesis. My role in the measurements was designing a movable entrance slit (slit apertures mounted on an xyz-manipulator) and aiding in the complicated alignment of all components. The measurements shown here were taken by Tim Oelze on his own.

There are several reasons for taking up this experiment. First of all, electron impact ionization is a very different ionization process from the main ionization process in the fluorescence spectra recorded at an FEL, namely direct photoionization. However, it is expected that the quasi-free electrons created in clusters by an FEL can also lead to electron impact ionization (see chapter 2.4.2). By measuring spectra caused exclusively by electron impact ionization, one may be able to learn more about its role in a cluster nanoplasma induced by 13.5 nm-photons.

The measurements can also be useful, however, for identifying charge states in the fluorescence spectra recorded at FLASH. One major obstacle in the identification is that the FEL intensity, even at the lowest values, was still sufficient to produce multiply charged ions. Therefore, one always has to deal with spectra in which many charge states contribute. By increasing the electron energy step by step, it should be possible to only generate charge states up to a certain value.

In figures A.5, A.6 and A.7, it can be seen that this works in principle. Figure A.5 shows spectra for different electron energies, which result in different relative abundances of spectral lines. Figure A.6 shows the relative abundance of charge states from Ar^{1+} to Ar^{4+} in dependence on electron energy. As can be seen, Ar^{1+} and Ar^{2+} are generated at electron energies as low as 90 eV, whereas Ar^{4+} can first be clearly identified at 500 eV.

Figure A.7 shows a comparison of fluorescence spectra, one recorded at a low FEL intensity of $8 \cdot 10^{12}$ W/cm^2 and the other induced by electron impacts from electrons with a kinetic energy of 1000 eV. As can be seen, many lines can be identified in both spectra, illustrating the usefulness of this method for the identification of spectral lines. However, there are also clear differences between the spectra, for example the lines between 46 and 47 nm in the electron impact induced spectrum, which are not present in the FEL induced spectrum. The reason may be, as Oelze suggests [99], that these lines correspond to transitions which are dipole-forbidden, so that their population by electron impact would be much more likely than by photoionization. Such similarities and discrepancies can be useful in determining the role of electron impact ionization in cluster experiments at FLASH.

T. Oelzes diploma thesis deals with argon spectra exclusively, but we also recorded some spectra of xenon clusters excited by electron impact ionization. The spectra are not shown here because stray light, whose origin could not be determined during the measurements, made a precise analysis very difficult. However, the spectra showed a clear trend of more spectral lines developing at shorter wavelengths with increased electron energy. This again shows the potential of this method to aid in the assignment of spectral lines.

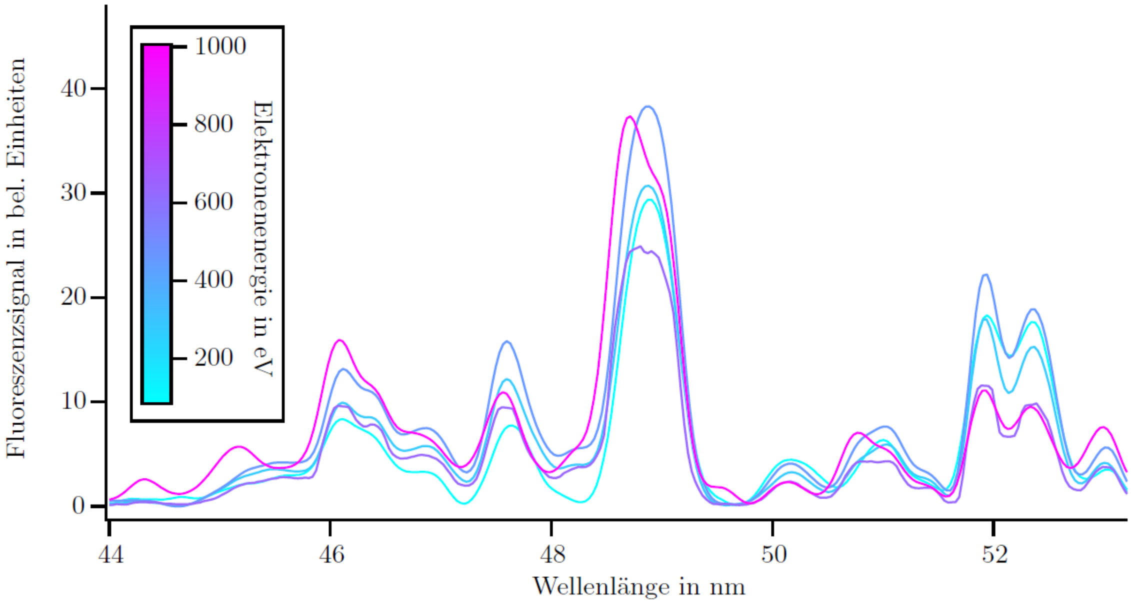

Figure A.5.: Dependence of electron impact induced fluorescence yield on the kinetic energy of the electrons (from Oelze [99]).

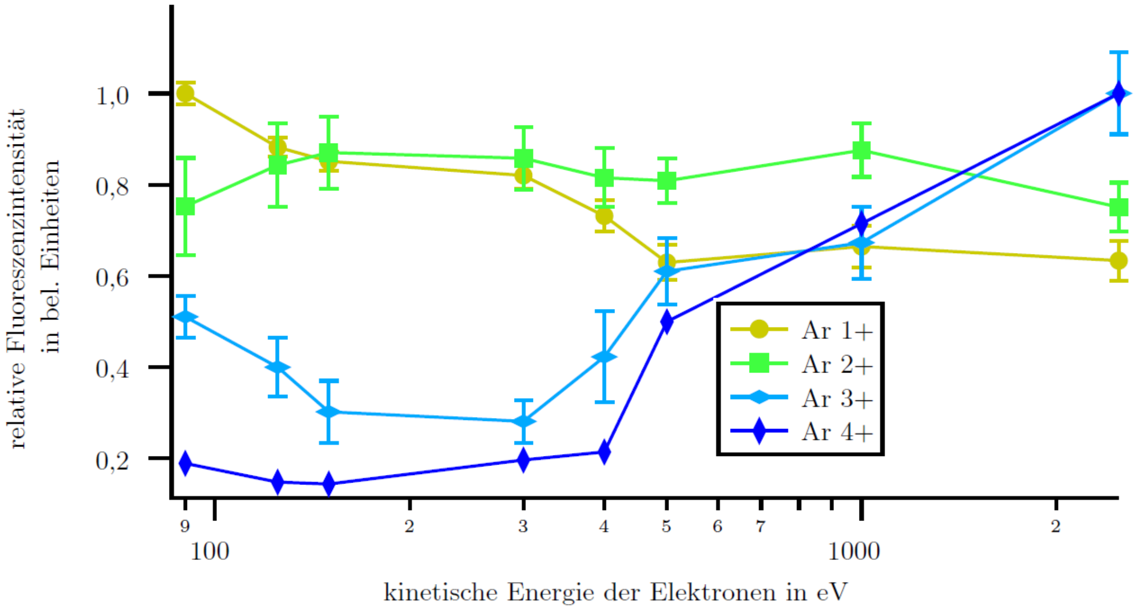

Figure A.6.: Dependence of charge state abundance on the kinetic energy of the electrons (from Oelze [99]). The charge states were derived from electron impact induced fluorescence spectra.

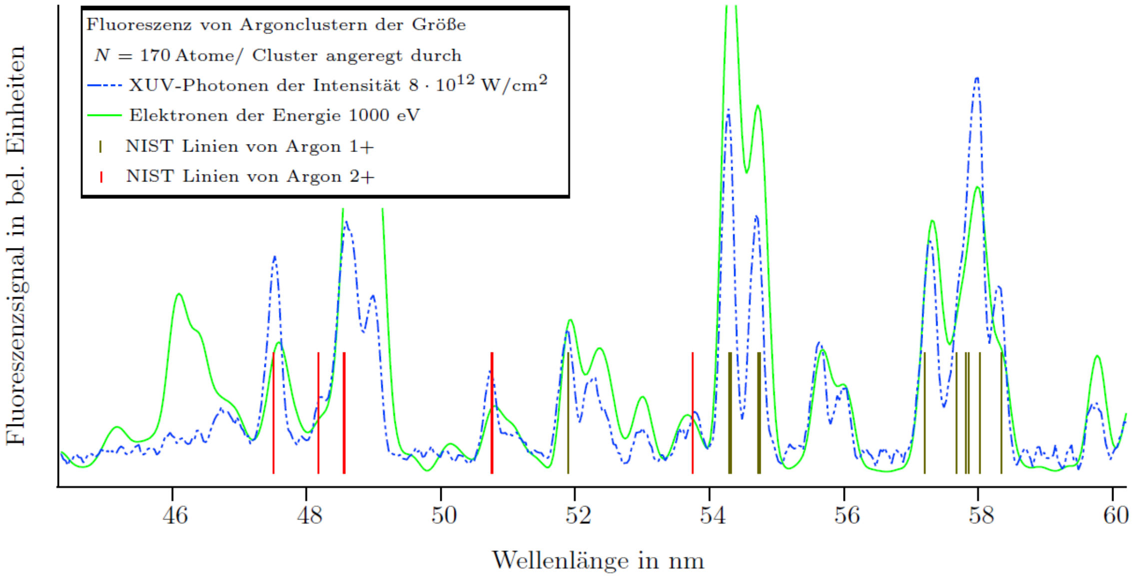

Figure A.7.: Comparison of Ar fluorescence spectra in dependence on wavelength, one recorded at a low FEL intensity (blue dashed line) and the other induced by impacts from electrons with a kinetic energy of 1000 eV (green line) (from Oelze [99]). Black lines (Ar^{1+}) and red lines (Ar^{2+}) signify charge states tabulated in the NIST database [67].

A.4. Dependence of individual charge states on cluster size, first scan

This section shows supplemental data to chapter 4.4.3, which deals with the dependence of the fluorescence yield of individual Xe charge states on the cluster size. Figure A.8 shows a plot for the first xenon cluster size scan, analogous to figure 4.21. This figure was omitted from the main body of the work because it essentially reproduces the conclusions drawn from figure 4.21: (i) For xenon, the decrease of fluorescence yield with increasing cluster size is strongly dependent on charge state. (ii) The decrease of Xe^{9+} is very pronounced. Differences in the abundance of individual charge states between the scans can be explained by the slightly higher FEL intensity in the second scan ($I = 2.4 \cdot 10^{15}$ to $2.5 \cdot 10^{15}$ W/cm^2 compared to $I = 2.3 \cdot 10^{15}$ to $2.4 \cdot 10^{15}$ W/cm^2).

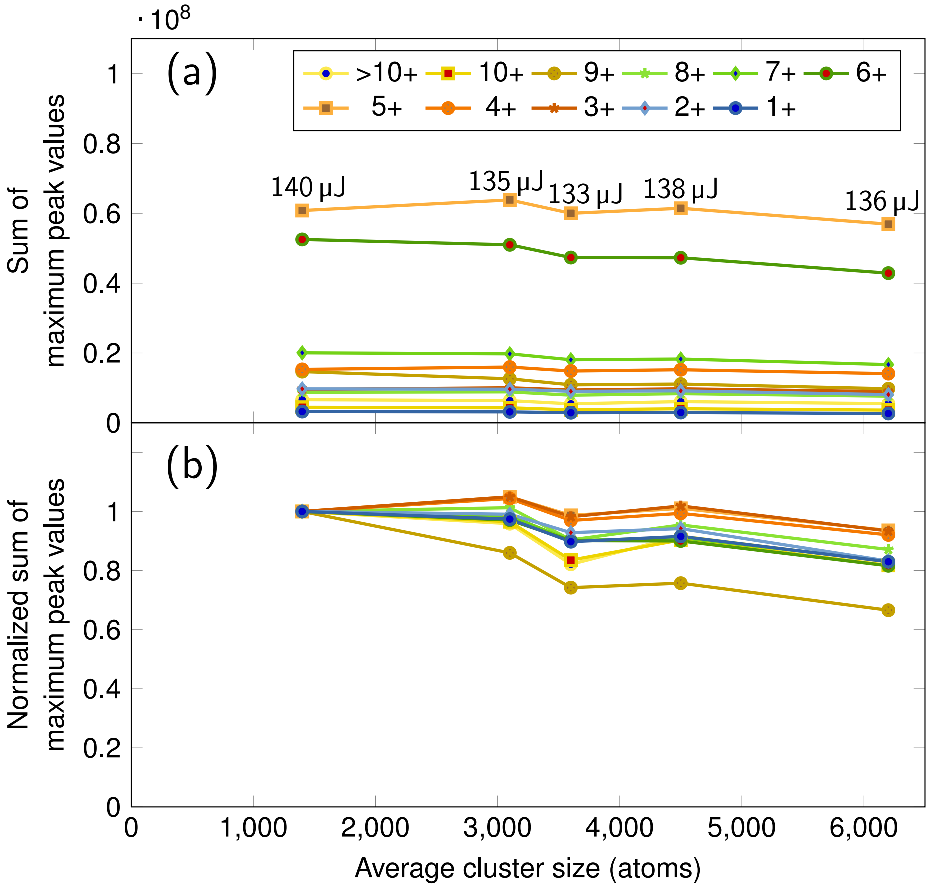

Figure A.8.: First xenon scan: (a) Distribution of charge states in dependence on cluster size. Lines which could not be unambiguously assigned to a charge state (see table 4.3) were not considered. Pulse energies have been added at each position. At wavelengths from 65 to 77 nm, the spectra of the three smallest cluster sizes only showed noise, which was artificially amplified by the normalization procedure. This noise skewed the results. Therefore in this region the three smallest cluster sizes were not considered. (b) All charge states normalized to 1 at an average cluster size of 1400 atoms. In this way, it is much easier to see that the behavior of xenon clusters is much more varied than that of argon.

List of Figures

List of Tables

Bibliography

[1] D. Attwood. *Soft X-Rays and Extreme Ultraviolet Radiation: principles and applications*. 1st ed. Cambridge University Press, 2007.

[2] E. Allaria et al. "Tunability experiments at the FERMI @ Elettra free-electron laser". *New J. Phys.* **14** (2012), 113009.

[3] P. Emma et al. "First lasing and operation of an angstrom-wavelength free-electron laser". *Nature Photon.* **4** (2010), 641–647.

[4] H. Tanaka et al. "A compact X-ray free-electron laser emitting in the sub-ångström region". *Nature Photon.* **6** (2012), 540–544.

[5] J. Jortner. "Cluster size effects". *Z. Phys. D - Atoms, Molecules and Clusters* **24** (1992), 247–275.

[6] R. Neutze et al. "Potential for biomolecular imaging with femtosecond X-ray pulses". *Nature* **406** (2000), 752–757.

[7] S. P. Hau-Riege et al. "Sacrificial Tamper Slows Down Sample Explosion in FLASH Diffraction Experiments". *Phys. Rev. Lett.* **104** (2010), 064801.

[8] U. Saalmann. "Cluster nanoplasmas in strong FLASH pulses: formation, excitation and relaxation". *J. Phys. B: At. Mol. Opt. Phys.* **43** (2010), 194012.

[9] M. Hoener et al. "Charge recombination in soft x-ray laser produced nanoplasmas". *J. Phys. B: At. Mol. Opt. Phys.* **41** (2008), 181001.

[10] A. McPherson et al. "Multiphoton-induced X-ray Emission". *Applied Physics B* **57** (1993), 337–347.

[11] A. McPherson et al. "Multiphoton-induced X-ray emission at 4-5 keV from Xe atoms with multiple core vacancies". *Nature* **370** (1994), 631–634.

[12] T. Ditmire et al. "High-energy ions produced in explosions of superheated atomic clusters". *Nature* **386** (1997), 54–56.

[13] T. Ditmire et al. "Nuclear fusion from explosions of femtosecond laser-heated deuterium clusters". *Nature* **398** (1999), 489–492.

[14] H. Wabnitz et al. "Multiple ionization of atom clusters by intense soft X-rays from a free-electron laser". *Nature* **420** (2002), 482–485.

[15] H. C. Kapteyn and T. Ditmire. "Ultraviolet upset". *Nature* **420** (2002), 467–468.

[16] C. Siedschlag and J.-M. Rost. "Small Rare-Gas Clusters in Soft X-Ray Pulses". *Phys. Rev. Lett.* **93** (2004), 043402.

[17] R. Santra and C. H. Greene. "Xenon Clusters in Intense VUV Laser Fields". *Phys. Rev. Lett.* **91** (2003), 233401.

[18] C. Jungreuthmayer et al. "Intense VUV laser cluster interaction in the strong coupling regime". *J. Phys. B: At. Mol. Opt. Phys.* **38** (2005), 3029–3036.

[19] D. Bauer. "Small rare gas clusters in XUV laser pulses". *Appl. Phys. B* **78** (2004), 801–806.

[20] H. Thomas et al. “Shell explosion and core expansion of xenon clusters irradiated with intense femtosecond soft x-ray pulses”. *J. Phys. B: At. Mol. Opt. Phys.* **42** (2009), 134018.

[21] C. Bostedt et al. “Ultrafast X-Ray Scattering of Xenon Nanoparticles: Imaging Transient States of Matter”. *Phys. Rev. Lett.* **108** (2012), 093401.

[22] T. Fennel, L. Ramunno, and T. Brabec. “Highly Charged Ions from Laser-Cluster Interactions: Local-Field-Enhanced Impact Ionization and Frustrated Electron-Ion Recombination”. *Phys. Rev. Lett.* **99** (2007), 233401.

[23] O. Hagena. “Cluster ion sources”. *Rev. Sci. Instrum.* **63** (1992), 2374–2379.

[24] J. Wörmer et al. “Fluorescence excitation spectroscopy of xenon clusters in the VUV”. *Chem. Phys. Lett.* **159** (1989), 321–326.

[25] M. Joppien. “Lumineszenzspektroskopische Untersuchung der elektronischen Anregungen von Helium- und Neon-Clustern”. Ph.D. thesis. Universität Hamburg, 1994.

[26] O. Hagena. “Nucleation and Growth of Clusters in Expanding Nozzle Flows”. *Surface Science* **106** (1981), 101–116.

[27] U. Buck and R. Krohne. “Cluster size determination from diffractive He atom scattering”. *J. Chem. Phys.* **105** (1996), 5408–5415.

[28] R. von Pietrowski. “Spektroskopische Untersuchungen an edelgasdotierten Edelgasclustern”. Ph.D. thesis. Universität Hamburg, 1997.

[29] R. Karnbach et al. “CLULU: An experimental setup for luminescence measurements on van der Waals clusters with synchrotron radiation”. *Rev. Sci. Instrum.* **64** (1993), 2838–2849.

[30] F. Dorchies et al. “Spatial distribution of cluster size and density in supersonic jets as targets for intense laser pulses”. *Phys. Rev. A* **68** (2003), 023201.

[31] J. Farges et al. “Structure and temperature of rare gas clusters in a supersonic expansion”. *Surface Science* **106** (1981), 95–100.

[32] A. L. Mackay. “A dense non-crystallographic packing of equal spheres”. *Acta Cryst.* **15** (1962), 916–918.

[33] O. Echt, K. Sattler, and E. Recknagel. “Magic Numbers for Sphere Packings: Experimental Verification in Free Xenon Clusters”. *Phys. Rev. Lett.* **47** (1981), 1121–1124.

[34] O. G. Danylchenko et al. “Phase Separation into Pure Components in Mixed Ar–Xe Clusters”. *JETP Letters* **84** (2006), 324–328.

[35] U. Frühling et al. “Single-shot terahertz-field-driven X-ray streak camera”. *Nature Photon.* **3** (2009), 523–528.

[36] *DESY Photon Science 2012. Highlights and Annual Report.* 2012.

[37] W. Ackermann et al. “Operation of a free-electron laser from the extreme ultraviolet to the water window”. *Nature Photon.* **1** (2007), 336 –342.

[38] J. Bödewadt. “Transverse Beam Diagnostics for the XUV Seeding Experiment at FLASH”. Ph.D. thesis. Universität Hamburg, 2011.

[39] K. Tiedtke et al. “The soft x-ray free-electron laser FLASH at DESY: beamlines, diagnostics and end-stations”. *New J. Phys.* **11** (2009), 023029.

[40] M. O. Krause. “Photoionization of atoms and molecules using synchrotron radiation”. *IEEE Transactions on Nuclear Science* **28** (1981), 1215–1219.

[41] J. B. West and G. V. Marr. “The Absolute Photoionization Cross Sections of Helium, Neon, Argon and Krypton in the Extreme Vacuum Ultraviolet Region of the Spectrum”. *Proc. R. Soc. Lond. A.* **349** (1976), 397–421.

[42] I. Nenner and P. Morin. “Electronic and nuclear relaxation of core-excited molecules”. In: *VUV and Soft X-ray Photoionization*. Ed. by U. Becker and D. A. Shirley. 1st ed. Chap. 9.

[43] J. W. Cooper. “Photoionization from Outer Atomic Subshells. A Model Study”. *Phys. Rev.* **128** (1962), 681–693.

[44] U. Becker et al. “Subshell photoionization of Xe between 40 and 1000 eV”. *Phys. Rev. A* **39** (1989), 3902–3911.

[45] A. Aguilar et al. “Absolute photoionization cross sections for Xe^{4+}, Xe^{5+}, and Xe^{6+} near 13.5 nm: Experiment and theory”. *Phys. Rev. A* **73** (2006), 032717.

[46] A. A. Sorokin et al. “Photoelectric Effect at Ultrahigh Intensities”. *Phys. Rev. Lett.* **99** (2007), 213002.

[47] D. R. Lide, ed. *CRC Handbook of Chemistry and Physics*. 84th ed. CRC Press, 2003.

[48] T. Fennel et al. “Laser-driven nonlinear cluster dynamics”. *Rev. Mod. Phys.* **82** (2010), 1793–1842.

[49] U. Saalmann, C. Siedschlag, and J. M. Rost. “Mechanisms of cluster ionization in strong laser pulses”. *J. Phys. B: At. Mol. Opt. Phys.* **39** (2006), R39–R77.

[50] M. Göppert-Mayer. “Über Elementarakte mit zwei Quantensprüngen”. *Ann. d. Phys.* **401** (1931), 273–294.

[51] I. Last and J. Jortner. “Quasiresonance ionization of large multicharged clusters in a strong laser field”. *Phys. Rev. A* **60** (1999), 2215–2221.

[52] T. Ditmire et al. “Interaction of intense laser pulses with atomic clusters”. *Phys. Rev. A* **53** (1996), 3379–3402.

[53] M. Arbeiter and T. Fennel. “Ionization heating in rare-gas clusters under intense XUV laser pulses”. *Phys. Rev. A* **82** (2010), 013201.

[54] M. Arbeiter and T. Fennel. “Rare-gas clusters in intense VUV, XUV and soft x-ray pulses: signatures of the transition from nanoplasma-driven cluster expansion to Coulomb explosion in ion and electron spectra”. *New J. Phys.* **13** (2011), 053022.

[55] J. Zweiback, T. Ditmire, and M. D. Perry. “Femtosecond time-resolved studies of the dynamics of noble-gas cluster explosions”. *Phys. Rev. A* **59** (1999), 3166–3169.

[56] I. Georgescu, U. Saalmann, and J. M. Rost. “Clusters under strong vuv pulses: A quantum-classical hybrid description incorporating plasma effects”. *Phys. Rev. A* **76** (2007), 043203.

[57] V. P. Krainov. “Inverse stimulated bremsstrahlung of slow electrons under Coulomb scattering”. *J. Phys. B: At. Mol. Opt. Phys.* **33** (2000), 1585–1595.

[58] B. Ziaja et al. “Emission of electrons from rare gas clusters after irradiation with intense VUV pulses of wavelength 100 nm and 32 nm”. *New J. Phys.* **11** (2009), 103012.

[59] C. Bostedt et al. “Multistep Ionization of Argon Clusters in Intense Femtosecond Extreme Ultraviolet Pulses”. *Phys. Rev. Lett.* **100** (2008), 133401.

[60] C. Bostedt et al. “Fast electrons from multi-electron dynamics in xenon clusters induced by inner-shell ionization”. *New J. Phys.* **12** (2010), 083004.

[61] C. Gnodtke, U. Saalmann, and J. M. Rost. “Ionization and charge migration through strong internal field in clusters exposed to intense x-ray pulses”. *Phys. Rev. A* **79** (2009), 041201.

[62] C. Gnodtke, U. Saalmann, and J. M. Rost. “Dynamics of photo-activated Coulomb complexes”. *New J. Phys.* **13** (2011), 013028.

[63] I. V. Hertel and C.-P. Schulz. *Atome, Moleküle und optische Physik 1*. 1st ed. Springer-Verlag Berlin Heidelberg, 2008.

[64] B. Ziaja et al. “Energetics, Ionization, and Expansion Dynamics of Atomic Clusters Irradiated with Short Intense Vacuum-Ultraviolet Pulses”. *Phys. Rev. Lett.* **102** (2009), 205002.

[65] V. P. Krainov and M. B. Smirnov. “Cluster beams in the super-intense femtosecond laser pulse”. *Physics Reports* **370** (2002), 237 –331.

[66] B. Ziaja et al. “Heterogeneous clusters as a model system for the study of ionization dynamics within tampered samples”. *Phys. Rev. A* **84** (2011), 033201.

[67] A. Kramida et al. *NIST Atomic Spectra Database (ver. 5.0), [Online]*. Aug. 2012. URL: `http://physics.nist.gov/asd`.

[68] T. Ditmire et al. “Strong X-Ray Emission from High-Temperature Plasmas Produced by Intense Irradiation of Clusters”. *Phys. Rev. Lett.* **75** (1995), 3122 –3125.

[69] N. Böwering et al. “Extreme ultraviolet emission spectra of highly ionized xenon and their comparison with model calculations”. *J. Appl. Phys.* **95** (2004), 16–23.

[70] M. A. Klosner and W. T. Silfvast. “Xenon-emission-spectra identification in the 5–20-nm spectral region in highly ionized xenon capillary-discharge plasmas”. *J. Opt. Soc. Am. B* **17** (2000), 1279–1290.

[71] I. I. Sobelman et al. “A capillary discharge plasma source of intense VUV radiation”. *Quantum Electronics* **33** (2003), 3–6.

[72] J.-P. Rozet et al. “State Selective Measurements of HCI Produced by Strong Ultrashort Laser-Clusters Interaction”. *Phys. Scr.* **T92** (2001), 113–118.

[73] I. Y. Skobelev et al. “On the Interaction of Femtosecond Laser Pulses with Cluster Targets”. *Journal of Experimental and Theoretical Physics* **94** (2002), 73–83.

[74] H. Iwayama et al. “Demonstration of up-conversion fluorescence from Ar clusters in intense free-electron-laser fields”. *Optics Express* **20** (2012), 23174–23179.

[75] B. H. Bransden and C. J. Joachain. *Physics of Atoms and Molecules*. 2nd ed. Pearson Education Limited, 2003.

[76] H. R. Griem. *Principles of Plasma Spectroscopy*. 1st ed. Cambridge University Press, 1997.

[77] I. I. Sobel’man, L. A. Vainshtein, and E. A. Yukov. *Excitation of Atoms and Broadening of Spectral Lines*. 2nd ed. Springer Verlag Berlin Heidelberg, 1995.

[78] B. L. Henke, E. M. Gullikson, and J. C. Davis. “X-ray interactions: photoabsorption, scattering, transmission and reflection for $E = 50 - 30000$ eV, $Z = 1 - 92$”. *Atomic Data and Nuclear Data Tables* **54** (1993), 181–342.

[79] P. Kirkpatrick and A. V. Baez. “Formation of optical images by x-rays”. *J. Opt. Soc. Am.* **38** (1948), 766–774.

[80] K. M. Skulina et al. “Molybdenum/beryllium multilayer mirrors for normal incidence in the extreme ultraviolet”. *Applied Optics* **34** (1995), 3727–3730.

[81] `http://www.cxro.lbl.gov`. *Center for X-Ray Optics*. Website. 1995-2007.

[82] M. Müller. “Untersuchung der Wechselwirkung intensiver Röntgenpulse mit Clustern durch Fluoreszenzspektroskopie”. Diplomarbeit. Technische Universität Berlin, 2012.

[83] E. Hecht. *Optics*. 4th ed. Addison Wesley, 2002.

[84] K. Tiedtke et al. “Gas detectors for x-ray lasers”. *J. Appl. Phys.* **103** (2008), 094511.

[85] R. Mitzner et al. “Direct autocorrelation of soft-x-ray free-electron-laser pulses by time-resolved two-photon double ionization of He”. *Phys. Rev. A* **80** (2009), 025402.

[86] C. Palmer and E. Loewen, eds. *Diffraction Grating Handbook*. 6th ed. Newport Corporation, 2005.

[87] R. R. Fäustlin. “Warm Dense Matter and Thomson Scattering at FLASH”. Ph.D. thesis. Universität Hamburg, 2010.

[88] J. L. Wiza. “Microchannel Plate Detectors”. *Nuclear Instruments and Methods* **162** (1979), 587–601.

[89] J. D. Carpenter et al. “An analysis of microchannel plate composition and its effect on extreme ultraviolet quantum efficiency”. *Nuclear Instruments and Methods in Physics research A* **573** (2007), 232–235.

[90] J. R. Lakowicz. *Principles of fluorescence spectroscopy*. 3rd ed. Springer-Verlag Berlin Heidelberg New York, 2006.

[91] S. Brühl. “Fluoreszenzspektroskopie an atomarem Xenon im vakuumultravioletten Spektralbereich”. Ph.D. thesis. Universität Hamburg, 1996.

[92] J. Wildman. *Bron-Kerbosch maximal clique finding algorithm*. Oct. 2011. URL: `http://www.mathworks.com/matlabcentral/fileexchange/30413`.

[93] C. Bron and J. Kerbosch. “Algorithm 457: finding all cliques of an undirected graph”. *Communications of the ACM* **16** (1973), 575–577.

[94] F. Cazals and C. Karande. “A note on the problem of reporting maximal cliques”. *Theoretical Computer Science* **407** (2008), 564–568.

[95] B. Ziaja et al. “Energetics, Ionization, and Expansion Dynamics of Atomic Clusters Irradiated with Short Intense Vacuum-Ultraviolet Pulses”. *Physical Review Letters* **102** (2009), 205002.

[96] S. Ackermann et al. “Generation of coherent 19 nm and 38 nm radiation at a free-electron laser directly seeded at 38 nm” (Submitted 2013).

[97] E. W. Schlag, ed. *Time-of-Flight Mass Spectrometry and its Applications*. 1st ed. Elsevier Science, 1994.

[98] W. C. Wiley and I. H. McLaren. “Time-of-Flight Mass Spectrometer with Improved Resolution”. *Rev. Sci. Instrum.* **26** (1955), 1150–1157.

[99] T. Oelze. “Untersuchung der Ionisationsprozesse von Argonclustern in höchstintensiven Pulsen weicher Röntgenstrahlung mit Methoden der Fluoreszenzspektroskopie”. Diplomarbeit. Technische Universität Berlin, 2013.

Danksagung

Alles, was diese Doktorarbeit umfasst, wäre nicht möglich gewesen ohne das Mitwirken zahlreicher Personen. Ich möchte mich bedanken bei:

- PD Dr. Tim Laarmann, sowohl für die Aufgabenstellung als auch für die fortwährende Unterstützung während aller Phasen dieser Arbeit
- der gesamten Arbeitsgruppe für die Hilfe während der Strahlzeiten und für die angenehme Arbeitsatmosphäre, sowie im speziellen:
  - Andreas Przystawik für viele hilfreiche Diskussionen und Gedankenanstöße
  - Andreas Kickermann für die Entwicklung des Nasen-TOFs. Außerdem ist es schön, nicht der einzige zu sein, der mit einer Doktorarbeit ringt
  - Jörn Bödewadt für das Aufklären einiger Feinheiten der Funktionsweise von FLASH
  - Angad Swiderski für die fehlerfreie technische Entwicklung des Spektrometers
- Professor Dr. Thomas Möller von der Technischen Universität Berlin für die Möglichkeit, die Messungen in der Tandemkonfiguration hinter dem Hauptexperiment durchführen zu können. Seiner Arbeitsgruppe danke ich für die Unterstützung bei den Messungen. Insbesondere:
  - Maria Müller für die hervorragende Zusammenarbeit bei der Messung der Fluoreszenzspektren und die aufschlußreichen Diskussionen zur Auswertung
  - Tim Oelze, ebenfalls für die hervorragende Zusammenarbeit bei der Messung der Fluoreszenzspektren und dafür, dass er mir kurzfristig seine Diplomarbeit zur Verfügung gestellt hat
  - Daniela Rupp, deren eiserne Kontrolle über den experimentellen Ablauf einen wesentlichen Anteil am Gelingen der Experimente hatte
- den Mitarbeitern der mechanischen Werkstätten, insbesondere für die Bereitschaft, in Notsituationen Aufträge auch kurzfristig zu erledigen
- allen Teams um FLASH, sowohl auf der Maschinen- als auch auf der Experimentseite

Und zu guter Letzt:

- meiner Familie und meinen Freunden, deren Zuspruch mir sehr geholfen hat. Ganz besonders möchte ich meinen Eltern danken, ohne deren Unterstützung ich das Physikstudium schon sehr früh aufgegeben hätte.